Spectroscopic factors and strength distributions for the deeply bound orbitals in ^{40}Ca obtained from the $(\vec{p}, 2p)$ reaction at 392 MeV

Yusuke Yasuda

Abstract

Cross sections and analyzing powers for the ^{40}Ca$(\vec{p}, 2p)$ reaction were measured with a 392-MeV polarized proton beam. Recoil momentum distributions of the cross section, which approximately reflect the Fermi momentum of nucleons in nuclei, and those of the analyzing power were measured for hole states of low-lying and deeply bound orbitals. The cross sections and the analyzing powers were analyzed by the distorted-wave impulse approximation (DWIA).

For the low-lying discrete states in separation energy spectra, measured recoil-momentum distributions of the cross section were well reproduced by a hole state of the $1d_{3/2}$ orbital for the peak at 8.3 MeV and a superposition of the $2s_{1/2}$ and $1f_{7/2}$ orbitals for the peak at 10.9 MeV respectively although the observed spectroscopic factors for these orbitals were larger than those from the previous $(e, e'p)$ studies. To discuss spectroscopic factors for deeply bound orbitals in ^{40}Ca, the normalization factor for the discrete states was determined as 0.53 comparing with a spectroscopic factor from the $(e, e'p)$ measurement. The recoil-momentum distributions of the analyzing power for the low-lying discrete states were qualitatively reproduced by the DWIA calculation but they were overestimated in the entire recoil-momentum range. It was found that the DWIA calculation reproduces the recoil-momentum distribution of the cross section and the analyzing power qualitatively well but quantitative problems on the normalization are left.

The strength distributions for the deep-hole states were obtained by a multipole decomposition analysis and a background subtraction. They were reasonably disentangled from continuous spectrum on the basis of characteristic behavior of the recoil-momentum distribution of the cross section depending on the orbital angular momentum L. The centroid energies and widths of the hole-state strengths were determined as 29.6 ± 0.5 and 48.4 ± 0.6 MeV for the $1p$ and $1s_{1/2}$-hole states respectively. The normalized spectroscopic factors for the deeply bound $1p$ and $1s_{1/2}$ orbitals were 49 ± 7 and $89 \pm 9\%$ of the sum-rule limits of independent-particle shell model, respectively. The reduction of the spectroscopic factors suggests an influence of the nucleon-nucleon correlations on the spectroscopic factors.

Contents

Chapter 1

Introduction

1.1 Nuclear structure and nucleon-nucleon correlations

A nucleus is a many body system that has been studied experimentally and theoretically for a long time. Among different nuclear models, the independent-particle shell model (IPSM) in the nuclear mean field describes distinctive features of nucleus like the existence of magic numbers or the spins and parities of nuclei. The IPSM assumes that the nucleons independently move in a nucleus, *i.e.* nucleon's motion in a nucleus is described by a single-particle wave function obtained by solving a Schrödinger equation with a mean-field potential, and a nucleus is described as a kind of product of the single-particle wave functions of nucleons. The nucleons occupy the single-particle orbitals, which are classified with principle quantum numbers and total angular momenta, from the deepest binding orbital to the shallow orbitals near the Fermi surface.

In microscopic nuclear models such as the IPSM, the nuclear mean field is built on the basis of nucleon-nucleon (NN) two-body interaction. However, some features of the NN interaction are neglected. The difference between the mean-field potential and the actual sum of the NN interactions is known as the residual interaction or the NN correlations, and it is necessary to describe nuclear structure in detail and attracts many researchers. The short-range correlations, which are related to the strong repulsive core of the NN two-body interaction, are the most important NN correlations. It has been an interesting topic how the strong repulsive interaction between nucleons works in nuclei. Recently, the spin-isospin and tensor correlations have also received much attention because they play an important role in the binding of nucleons and affect the shell structure in exotic nuclei [1, 2].

In the theoretical point of view, in the 1950s, Jastrow proposed a method to take the influence of the strong two-body repulsive force into a theoretical description of the nucleus using a correlation function [3]. This function is multiplied on the single-particle wave functions so as to take the short-range correlation into account, and the amplitude of the modified wave functions become zero when nucleons are in a short distance. This method was employed in the following works, and it was predicted that high-momentum components in nucleon momentum are enhanced due to the NN correlations [4, 5,

6, 7, 8].

1.1.1 Spectroscopic factor

Spectroscopic factor is a useful measure to examine the NN correlation. The spectroscopic factor is defined as a ratio of the measured cross section to the theoretical cross section calculated within the IPSM framework. For knock-out and pick-up reactions, this factor indicates how many nucleons in the orbital participate in the reaction channel, and approximately shows how many nucleons are in the orbital in the target nucleus. In a naive shell-model picture, the spectroscopic factor for an orbital with total angular momentum J is expected to be $2J + 1$, since orbitals in nuclei are filled by nucleons up to $2J + 1$.

In a knock-out reaction, an incident particle is scattered from a nucleon in a nucleus and the recoiled nucleon is knocked out from the nucleus. The residual nucleus is expected to be a one-hole state because a nucleon is independently moving in the nucleus in the view of the IPSM. When the nucleon in the nucleus strongly correlates with another nucleon, the residual nucleus is far from one-hole state and the correlated nucleon is often ejected from the nucleus at the same time. Consequently, a cross section measured under the kinematical condition that the residual nucleus is expected to remain a one-hole state decreases, that is, the existence of NN correlated pairs makes the spectroscopic factor decrease. Therefore, the spectroscopic factor is of importance to examine the NN correlations.

1.1.2 Previous studies of the spectroscopic factor

The spectroscopic factors for orbitals in nuclei have been measured to investigate the influence of the NN correlations on the shell structure. Early spectroscopic studies were performed by the $(d, {}^3\text{He})$ reaction for proton (*e.g.* Ref. [9]). As the progress of electron accelerators, experiments for quasi-free knock-out reactions with electron beams were actively performed. At the Nationaal Instituut voor Subatomaire Fysica, Amsterdam (NIKHEF), high resolution studies of the $(e, e'p)$ reaction were carried out for nuclei in the wide mass range from ${}^2\text{H}$ to ${}^{209}\text{Bi}$, as reviewed by Dieperink and Witt Huberts [10].

From the results of high resolution $(e, e'p)$ experiments at NIKHEF, Lapikás *et al.* reported the spectroscopic factors for the nucleon orbitals close to the Fermi surface in ${}^{16}\text{O}$, ${}^{40}\text{Ca}$, ${}^{48}\text{Ca}$, ${}^{90}\text{Zr}$, and ${}^{208}\text{Pb}$ decrease to 60%–70% of the simple IPSM limits ($2J + 1$) and compared those factors with predictions from nuclear matter calculations that include short-range and tensor correlations [11]. Figure 1.1 from Ref. [11] shows summed spectroscopic strength as a function of the missing energy. A large reduction is observed near the Fermi surface. This reduction of the spectroscopic factor cannot be described in the IPSM and it is expected to be ascribed to the presence of correlations between the nucleons, coming from the residual nuclear interactions.

The curves in Fig. 1.1 show theoretical calculations by Benhar *et al.* using a microscopic nuclear matter calculation with the correlated basis function (CBF) theory including the NN correlations and
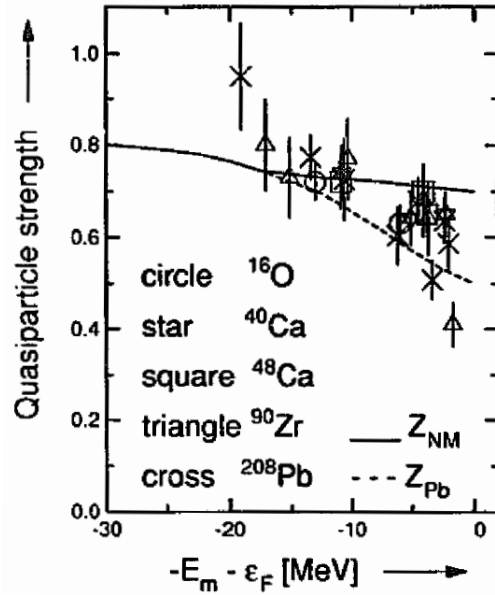
Figure 1.1: Summed spectroscopic strength observed for proton knock-out reactions from various orbitals in the closed-shell nuclei ^{16}O, ^{40}Ca, ^{48}Ca, ^{90}Zr, and ^{208}Pb as a function of the mean excitation energy of the orbital relative to the Fermi energy (ϵ_F). The dashed curve represents the quasi-particle strength calculated for nuclear matter, the solid curve is derived from the nuclear matter curve by including surface effects calculated for ^{208}Pb [12]. This figure is taken from Ref. [11].

surface effects [12]. The quenched spectroscopic strength near the Fermi surface was explained by both contributions of the NN correlations and the surface effects. It is worthy of notice in Fig. 1.1 that the hole-state strengths far below the Fermi surface, where the surface effects are not important, were suggested to decrease to almost 80% of the IPSM limits [12].

Some theoretical calculations performed with state-dependent correlations also suggested the reduction of spectroscopic factors for deeply bound orbitals. The spectroscopic factors calculated by Fabrocini et $al.$ for the $1s$ and $1p$ orbitals are quenched to 70% and 90% of the IPSM limits in ^{16}O, and to 55% and 58% in ^{40}Ca, respectively [13]. According to this calculation, the depletion of the spectroscopic factors by the NN correlations is 10%–15% for the valence orbitals and 30%–45% for the deeply bound orbitals. Most of the depletion was caused by the spin-isospin and tensor components of the NN correlations in their calculation. Bisconti et $al.$ developed the calculation following Ref. [13] by Fabrocini et $al.$, and predicted the spectroscopic factors for several doubly-closed-shell nuclei to be 80% or less of the IPSM limit for the $1s$ and $1p$ orbitals in medium and heavy nuclei [14]. It is interesting that the spectroscopic factor for the deepest $1s$ orbital is suppressed owing to the NN correlations most strongly of all the orbitals in both of the calculations [13, 14].

Since the deeply bound orbitals such as $1s$ and $1p$ orbitals are bound far below the Fermi surface in medium and heavy nuclei, the spectroscopic factors for these orbitals will not be affected by surface effects but will be predominantly affected by the NN correlations. Therefore, it is interesting for the
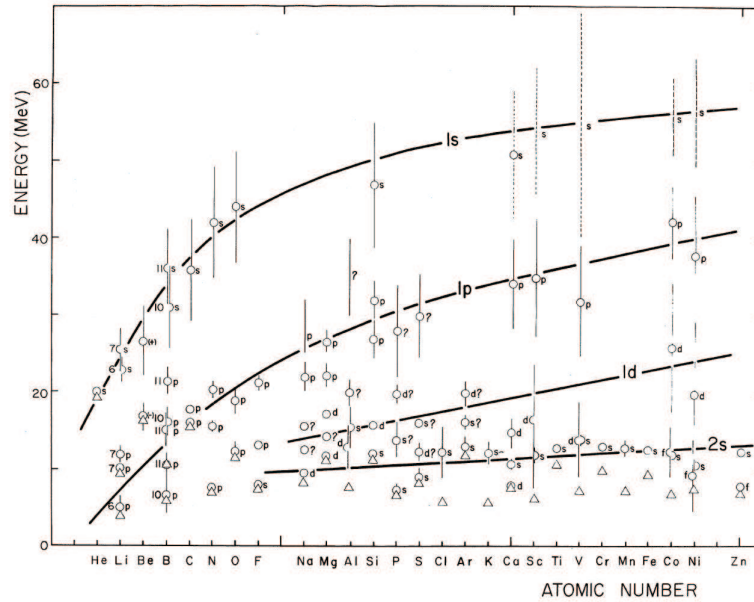
Figure 1.2: Separation energies, widths, and angular momentum assignments of the hole states obtained from quasi-free scattering, as functions of the atomic number. This figure is taken from Ref. [15].

study of NN correlations to investigate the spectroscopic factors for the deeply bound orbitals in medium and heavy nuclei.

1.1.3   Previous measurements of deep-hole states

The valence or low-lying orbitals, which characterize the spin state of the nucleus, have been studied well, whereas the nature of the deeply bound orbitals in medium and heavy nuclei have not sufficiently been investigated and the deeply bound orbitals are assumed to be fully occupied by nucleons in the IPSM.

Figure 1.2 from Ref. [15] is a famous figure on separation energies and widths compiled by Jacob and Maris. Separation energies and widths for hole states were obtained from quasi-free reactions for the wide mass-number range of nuclei. The separation energy is an energy to remove a nucleon from a nucleus, that is, a binding energy of the nucleon. For the heavy nuclei, the experimental knowledge for deeply bound orbitals was far from rich and has hardly been updated. Since the hole states knocked out from the deeply bound orbitals are thought to have short lifetimes and large widths and they overlap each other, it is very difficult to identify deep hole states.

In the medium-mass range of nuclei, for example, ^{40}Ca is often used for study on nuclear structure since it is a doubly magic nucleus. As ^{40}Ca has a core of closed shells with 16 nucleons (8 protons and 8 neutrons), the $1s_{1/2}$ and $1p$ orbitals in the inner core are suitable to study correlations far below the Fermi surface. Many pioneering attempts were performed so as to examine the single-particle behavior

of the deep-hole states by the $(e, e'p)$ [16, 17, 18, 19] and $(p, 2p)$ [20, 21] reactions with the ^{40}Ca target.

In the work by Mougey *et al.* in Ref. [16], the hole-strength distribution from the $(e, e'p)$ reaction was obtained by using the momentum dependence of the spectral function as shown in Fig. 1.3. Since this distribution is plotted in large energy bins and they tentatively gave mean removal energies of the $1s$- and $1p$-hole states, the information on the deep-hole states were not reliable. The reported spectroscopic factors were 75% of the IPSM limit for the $1s_{1/2}$ orbital and 95% for the $1p$ orbital.

Nakamura *et al.* also reported the result of the $(e, e'p)$ reaction experiment [17, 18]. The hole states except for the $1s_{1/2}$ orbital were identified by fitting their distorted momentum distributions. The $1s_{1/2}$- hole-state distributions in Fig. 1.4 were extracted by subtracting the contribution of the upper shells and the background due to multiple collision processes from the separation energy spectra [18]. These distributions were not on the basis of the recoil-momentum dependence and the shapes of the $1s_{1/2}$ distributions in Fig. 1.4 are unclear. The reported spectroscopic factors for the $1s_{1/2}$ and $1p$ orbitals are larger than the sum-rule limits.

Figure. 1.5 from Ref. [20] shows the strength distributions obtained from the $(p, 2p)$ reaction by James *et al.* They are better in statistics than those from the electron scattering, but low-lying states, which correspond to the ground or first excited states of the residual nucleus ^{39}K, are not separated due to insufficient separation-energy resolution of 4–5 MeV (FWHM). Although James *et al.* reported the ratios of the measured protons to the protons occupying the nlj shell as reduction factors, it is difficult to compare those values for the low-lying states with other measurements for checking consistency of the analysis owing to the poor separation of the low-lying states. They separated the contributions of the orbitals from the strength distributions by using distorted momentum distributions and identified the $1s$ level in ^{40}Ca, however, they didn't give the centroid of the distribution because of the broad nature of the level.

The reported spectroscopic factors $1s_{1/2}$ and $1p$ orbitals in ^{40}Ca are not consistent among these experiments, and their centroids of the distributions are unreliable. Thus, these values of interest are still controversial.

After the dawn of the knockout-reaction experiment, in the 1990s, the Petersburg Nuclear Physics Institute (PNPI) group reported that they had succeeded in identifying the $1s_{1/2}$-hole states for medium- and heavy-mass nuclei such as ^{40}Ca, ^{90}Zr, and ^{208}Pb in the separation-energy spectra for the $(p, 2p)$ and (p, np) reactions with a proton beam at 1 GeV [22, 23]. Figure 1.6 from Ref. [22] shows separation-energy spectra for the ^{40}Ca$(p, 2p)$ (upper three figures in Fig. 1.6) and ^{40}Ca(p, pn) (lower three figures in Fig. 1.6) reactions, and broad bumps of the deepest $1s$-hole states are observed in the spectra. There is no other experiment identifying $1s$-hole states in separation energy spectra for the medium- and heavy-mass nuclei except the PNPI group. The high energy 1-GeV injection beam might be advantageous to identify deep hole states. Since the absolute cross sections were not measured, the spectroscopic factors were not be given. Nevertheless, these reports encouraged many researchers to study deep-hole states again.
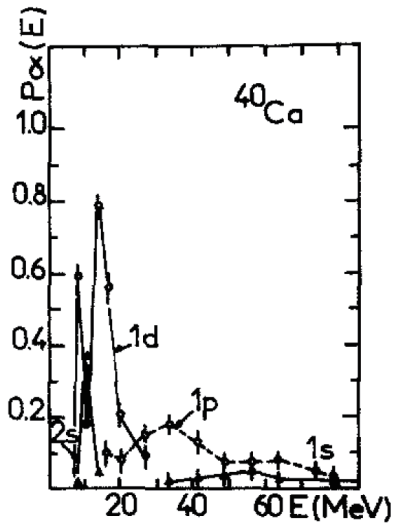
Figure 1.3: Hole-strength distribution from $(e, e'p)$ reaction for ^{40}Ca obtained by Mougey *et al.* This figure is taken from Ref. [16].
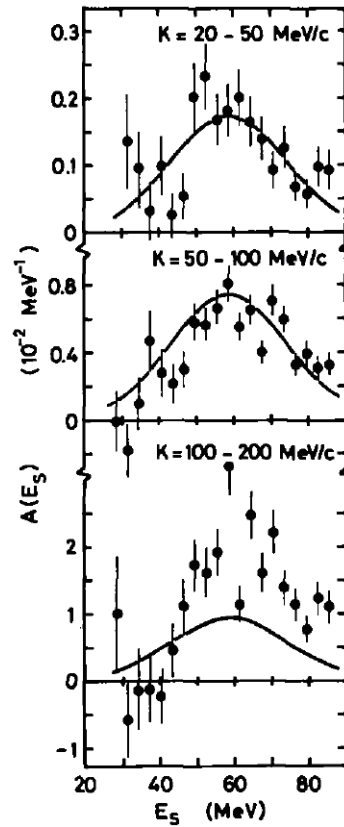

Figure 1.4: Separation energy spectra in the $1s_{1/2}$ region for ^{40}Ca after subtraction of the contributions of upper shells and backgrounds in $(e, e'p)$ reaction. This figure is taken from Ref. [18].

As described above, the measurements providing the information on all of the orbitals from the surface to the inner core in a nucleus with absolute cross sections and sufficient resolution of the separation energy were unavailable. Such a kind of measurement is necessary to compare spectroscopic factors for low-lying states with those from the high-resolution $(e, e'p)$ reaction measurement and to ensure the values for deeply bound orbitals.

1.1.4 Direct measurement of NN-correlated pair

There are other methods that don't employ spectroscopic factors to study the NN correlation. Several experiments were performed by knock-out reaction to directly measure the correlated nucleon pairs. When a nucleon in a correlated pair is knocked out, the other nucleon in the pair recoils. Taking advantage of this nature, correlated nucleon pairs were measured under the back-to-back kinematical condition as evidence of short-range correlations by the $(e, e'pp)$ reaction at the Thomas Jefferson National Accelerator Facility (JLab) [24, 25] and at NIKHEF [26], by the $(e, e'pn)$ reaction at Maintz [27, 28], and by the $(p, 2pn)$ reaction at Brookhaven National Laboratory (BNL) [29, 30]. At JLab, Subedi *et al.* measured
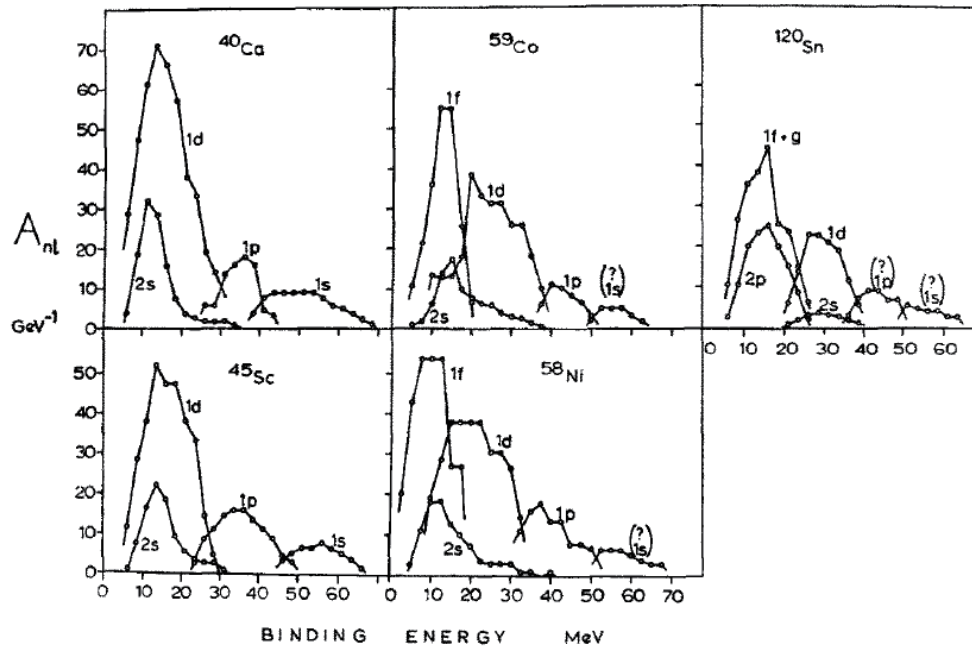
Figure 1.5: Strength distributions from the $(p, 2p)$ reaction obtained for various nuclei by James *et al.* This figure is taken from Ref. [20].

the $^{12}C(e, e'pn)$, $^{12}C(e, e'pp)$, and $^{12}C(e, e'p)$ reactions simultaneously, and they suggested from their result that the 80% of the nucleons in the ^{12}C behave as described within the shell model, and 18% of them are p–n correlated pairs and the rest of 2% are p–p and n–n correlated pairs.

The result of these direct measurement indicates the existence of the state in which nucleons correlate each other. However, this kind of experiment don't answer the question how much nucleons occupy the single-particle states in nuclei. The study of the spectroscopic factor can provide the information on this question. Therefore, the direct measurement of NN-correlated pair and the spectroscopic study should be complementary on the study of nuclear structure.

1.2 Quasi-free knock-out $(p, 2p)$ reaction

Quasi-free knock-out reaction is one of the most direct methods to investigate the single-particle properties of a nucleus such as spectroscopic factors or nucleon-momentum distributions and modification of the single-particle orbitals in nuclear medium. This is a process where an incident particle knocks a nucleon out of a nucleus and the residual nucleus remains in a one-hole state. If the energy of the incoming particle and the momentum transfer to the nucleon in the nucleus is sufficiently large, the influence of the other spectator nucleons in the nucleus on the knock-out process can be neglected and the scattering of the incident particle and the knocked-out nucleon is like a scattering in a free space. This is the reason why this process is called quasi-free or quasi-elastic scattering. The $(p, 2p)$ reaction
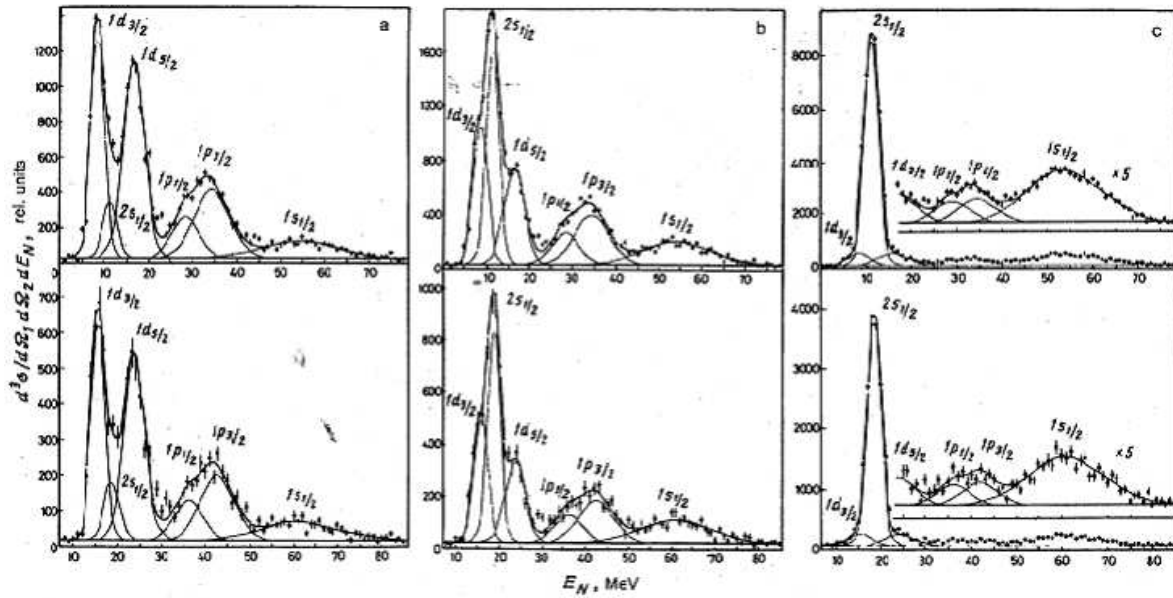
Figure 1.6: Separation-energy spectra for the ^{40}Ca$(p, 2p)$ (upper three figures) and ^{40}Ca(p, pn) (lower three figures) reactions measured with a 1 GeV proton beam at Petersburg Nuclear Physics Institute (PNPI) from Ref. [22]. The detection range of proton energy is (a) 830–870, (b) 855–887, and (c) 880–915 MeV, respectively.

differs from pp scattering in a free space on the point that the knocked-out nucleon is bound and has the Fermi momentum in a nucleus before the scattering. The cross section for the $(p, 2p)$ reaction depends not only on the NN-scattering amplitude but also the Fermi momentum in a nucleus. This nature of the cross section is useful to examine the momentum distribution of a nucleon in a nucleus. As quasi-free knock-out reactions have three-body final states, measurements can be made under various kinematical conditions to investigate a momentum distribution of a nucleon in nuclei.

The first experiments of such processes were the $(p, 2p)$ reaction experiments, which were performed at Berkeley using 340 MeV incident proton beam for light nucleus and the coincident proton pairs were observed [31, 32]. Subsequently, the $(p, 2p)$ reaction experiments were performed with medium-energy proton beams at Uppsala, CERN, Liverpool, and so on, as reviewed in Refs. [33, 34, 35]. For the description of the $(p, 2p)$ reaction, DWIA calculations have been developed and used. In the impulse approximation, the proton-proton matrix element is replaced by that of free proton-proton scattering for the kinematics of the experiment. The three wave functions of the incoming and outgoing protons are distorted by complex optical potentials. This distortion reflects inelastic multiple scattering. The distortion reduces the intensity of scattered protons and smears out the angular correlations expected from the momentum distributions in the orbitals.

Since the 1980s, the spectroscopic study by the $(p, 2p)$ reaction principally progressed at Indiana, TRIUMF, Maryland, and iThemba [36, 37, 38, 39, 40, 41, 42, 43, 44]. The experiments were mostly performed at the energy range of 100–200 MeV. The spectroscopic factors obtained with the DWIA

calculation were often different between the measurement conditions, that is, the absolute values of the cross section from the DWIA calculation have some uncertainties. Nevertheless, iThemba group obtained the spectroscopic factors for the hole states of the valence orbitals in ^{208}Pb and found that they are in good agreement with the $(e, e'p)$ studies [44].

On the other hand, quasi-free $(e, e'p)$ reaction measurement has also been performed since the 1960s [33, 34, 45, 46]. Only the outgoing proton suffers distortion owing to the optical potential, so that the intensity reduction and strong distortion are less severe in the $(e, e'p)$ scattering than in the $(p, 2p)$ scattering. Thus the spectroscopic factors provided by the $(e, e'p)$ reaction have small uncertainties [47]. Since the $(e, e'p)$ reaction occurs in whole of the radial range of a target nucleus [47], this reaction is effective to investigate whole of a bound-state wave function with respect to the radial range. However, as the cross sections are much smaller than those for the $(p, 2p)$ reaction owing to the electromagnetic interaction between the incident electron and a nucleon in a nucleus, the measurement was limited to the hole states of the low-lying orbitals.

In both of the $(p, 2p)$ and $(e, e'p)$ reactions, the cross sections for the deep-hole states are much smaller than those for the low-lying states. Although the intensity reduction for the $(p, 2p)$ reaction owing to multiple collisions is more severe than that for the $(e, e'p)$ reaction, the $(p, 2p)$ reaction has an advantage to gain yields sufficiently for deep-hole states. If the $(p, 2p)$ measurement is performed with enough resolution of the separation energy to separate low-lying states, the deduced spectroscopic factors can be compared with those for low-lying states from the $(e, e'p)$ reaction and be checked their absolute values. Furthermore, normalizing the spectroscopic factors to that from the $(e, e'p)$ reaction, it is possible to avoid the uncertainty owing to the large intensity reduction and to determine spectroscopic factors for deep-hole states with small uncertainty. Therefore, the $(p, 2p)$ measurement from deep-hole to low-lying states with sufficient resolution of the separation energy can provide reliable values of spectroscopic factors with the aid of the result of the $(e, e'p)$ reaction.

The $(p, 2p)$ reaction has an another property that the $(e, e'p)$ reaction doesn't have. In the measurement of the $(p, 2p)$ reaction with a polarized proton beam, cross sections have asymmetry depending on the direction of the proton spin. In 1973, Jacob and Maris suggested that analyzing powers (A_y's) for the hole states of the $j_>$ and $j_<$ orbitals are expected to behave differently owing to the spin-orbit coupling in the nucleus [48]. Analyzing powers were measured with polarized proton beam at TRIUMF for ^{16}O and ^{40}Ca at 200 MeV [49, 37, 38] and for ^{16}O at 500 MeV [39], and the J dependence of the analyzing power were experimentally confirmed [35]. The analyzing powers for the $1p_{3/2}$- and $1p_{1/2}$-hole states in the ^{16}O$(p, 2p)$ reaction measured by changing a kinetic energy of an ejected proton are shown in Fig. 1.7 from Ref. [37]. Since the $1p_{3/2}$- and $1p_{1/2}$ orbitals have a different spin-orbit coupling, the analyzing powers for these states behave differently. This effect for the analyzing power is called Maris effect. As a result of the extensive investigation of the $(p, 2p)$ reaction, the analyzing power for a hole state is recognized to be due to the spin-orbit part of the optical potential for an orbital with $L = 0$ and to both the spin-orbit part and the effective polarization (Maris effect) for a $L \neq 0$ orbital. Therefore, the analyzing power data can provide the information on the $j_>$ and $j_<$ orbitals and may separate contributions of $j_>$- and $j_<$-hole states in the cross sections.
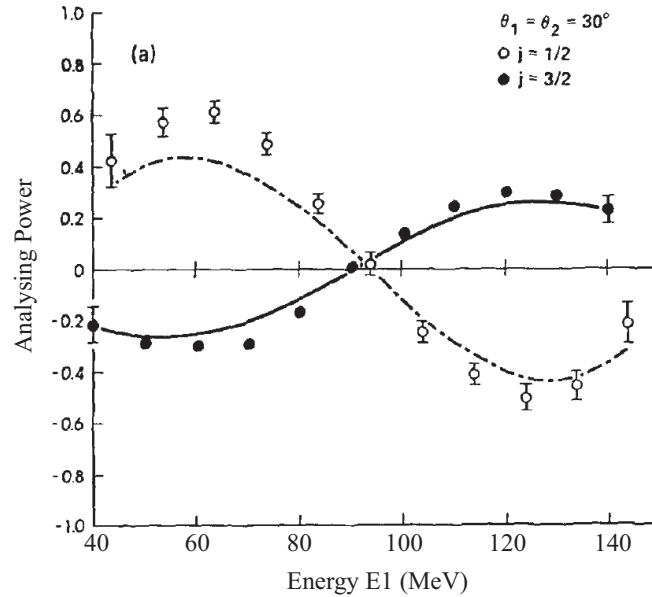
Figure 1.7: Analyzing powers for the $1p_{3/2}$ and $p_{1/2}$-hole states in the $^{16}O(p, 2p)$ reaction measured by changing a kinetic energy of an ejected proton. They behave differently as predicted by Jacob and Maris and show the validity of Maris effect. This figure is taken from Ref. [37].

1.3 $(p, 2p)$ experiment at $1\,\mathrm{GeV}$

In 1999 and 2000, our group performed $(p, 2p)$ experiments with 1 GeV proton beam at PNPI to measure the hump of the $1s$-hole state in ^{40}Ca in a separation energy spectrum and its absolute cross section simultaneously [50]. The magnetic spectrometers were set at an asymmetric angle condition and the measured kinetic energies of the ejected two protons were unbalanced, following a previous work by Volkov *et al* [22]. However, the $1s$-hole state could not be identified in the separation energy spectrum at that time. There was no visible hump at the expected separation-energy region. Volkov *et al.* used a magnetic spectrometer and a time of flight detector array that consists of scintillation counters to analyze momenta of two protons, whereas we used two magnetic spectrometers. The time of flight detector array had 10 times smaller acceptance of the vertical angular acceptance than that of a magnetic spectrometer. Therefore, it was considered that a large detected vertical angle accepted wide recoil momentum ranges of residual nuclei and possibly smeared the separation-energy spectrum.

1.4 Purposes of this work

Reliable extraction of the strength distributions of deep-hole states is of much interest. It has been desired for long to determine the spectroscopic factors for deeply bound orbitals far below the Fermi surface and to discuss their quenching. To clarify these matters, in the present work, we performed the ^{40}Ca$(p, 2p)$ reaction experiment with a polarized proton beam at $392\,\mathrm{MeV}$ and with a high separation-

energy resolution of 750 keV, and measured the cross sections and the analyzing powers for the all orbitals from the inner core to the Fermi surface.

The high-resolution measurement enables us to observe the low-lying states as the discrete peaks in the separation-energy spectrum, so these states are independently studied. The low-lying discrete states are useful for verifying the *L*-dependence of the cross section and for checking the DWIA calculation. Furthermore, it is possible to compare the measured spectroscopic factors for low-lying states with those from the $(e, e'p)$ reaction for checking the absolute value. The uncertainty due to the strong intensity reduction can be eliminated by comparing the spectroscopic factor for the low-lying discrete states from the $(p, 2p)$ reaction with those from the $(e, e'p)$ reaction.

^{40}Ca is a suitable nucleus to study deeply bound orbitals since ^{40}Ca is a nucleus in the medium-mass region and has a core of closed shells. It would be premature to use much heavier nucleus than ^{40}Ca. The energy of 392 MeV of the injection proton is higher than the energy of 200 MeV, where many $(p, 2p)$ experiments have been performed. Since both of the ejected protons have larger kinetic energies than protons in case of 200 MeV injection, the protons ought to suffer less multiple collisions. Furthermore, when a polarized proton beam is used, the *J* dependence of the analyzing power for the $(p, 2p)$ reaction might be useful for separating the contributions of the $j_{>}$- and $j_{<}$-hole states.

In the following chapters, the detail of the present work is presented. The experimental setup is explained in Chap. 2. The data reduction and analysis of measured data are presented in Chap. 3 and 4. The result is shown in Chap. 5 and discussed in Chap. 6. At last, the summary is given in Chap. 7.

Chapter 2

Experiment

The experiment was performed under Program No. E168 and E217 in the ring cyclotron facility at RCNP, Osaka University, with a 392-MeV polarized proton beam and the dual-arm spectrometer system in the WS beam line. A schematic layout of the RCNP cyclotron facility is shown in Fig. 2.1.

2.1   Kinematics

In the $(p, 2p)$ reaction measurement, an injected proton interacts with a bound proton in the target nucleus and both of the bound and injected protons go out from the nucleus. The knocked-out proton and the scattered proton are measured in the experiment.

In the $A(p, 2p)B$ reaction with a target nucleus A and a residual nucleus B, as illustrated in Fig. 2.2, the separation energy E_{sep} is given by

$$E_{\text{sep}} = T_0 - T_1 - T_2 - T_3 = E_x - Q, \tag{2.1}$$

where T_i $(i = 0, 1, 2, 3)$ are the kinetic energies of the incident proton $(i = 0)$, the scattered and knocked-out protons $(i = 1, 2)$, and the residual nucleus $(i = 3)$. The quantities E_x and Q indicate the excitation energy of the residual nucleus B and the reaction Q-value [$Q = M_A - (M_B + m_p)$], respectively; M_A, M_B, and m_p are the masses of the target nucleus, the residual nucleus, and the proton. The separation energy is the energy required to knock out a proton from a target nucleus, corresponding to the binding energy of the knocked-out proton.

The momenta and the scattering angles of the two ejected protons were measured in the $(p, 2p)$ measurement. Although the residual nucleus was not detected, its momentum ($\boldsymbol{p_3}$) was calculated from the momenta of the incident proton and two ejected protons on the basis of the momentum conservation law. Though the residual nucleus is a spectator for quasi-free knock-out reactions in the view of the IPSM, it recoils and has a momentum owing to the momentum conservation. The momentum ($\boldsymbol{p_3}$) is called a recoil momentum. Since the target nucleus is at rest before the scattering, the proton ejected from the nucleus should have a momentum $-\boldsymbol{p_3}$, which corresponds to the Fermi momentum, in the
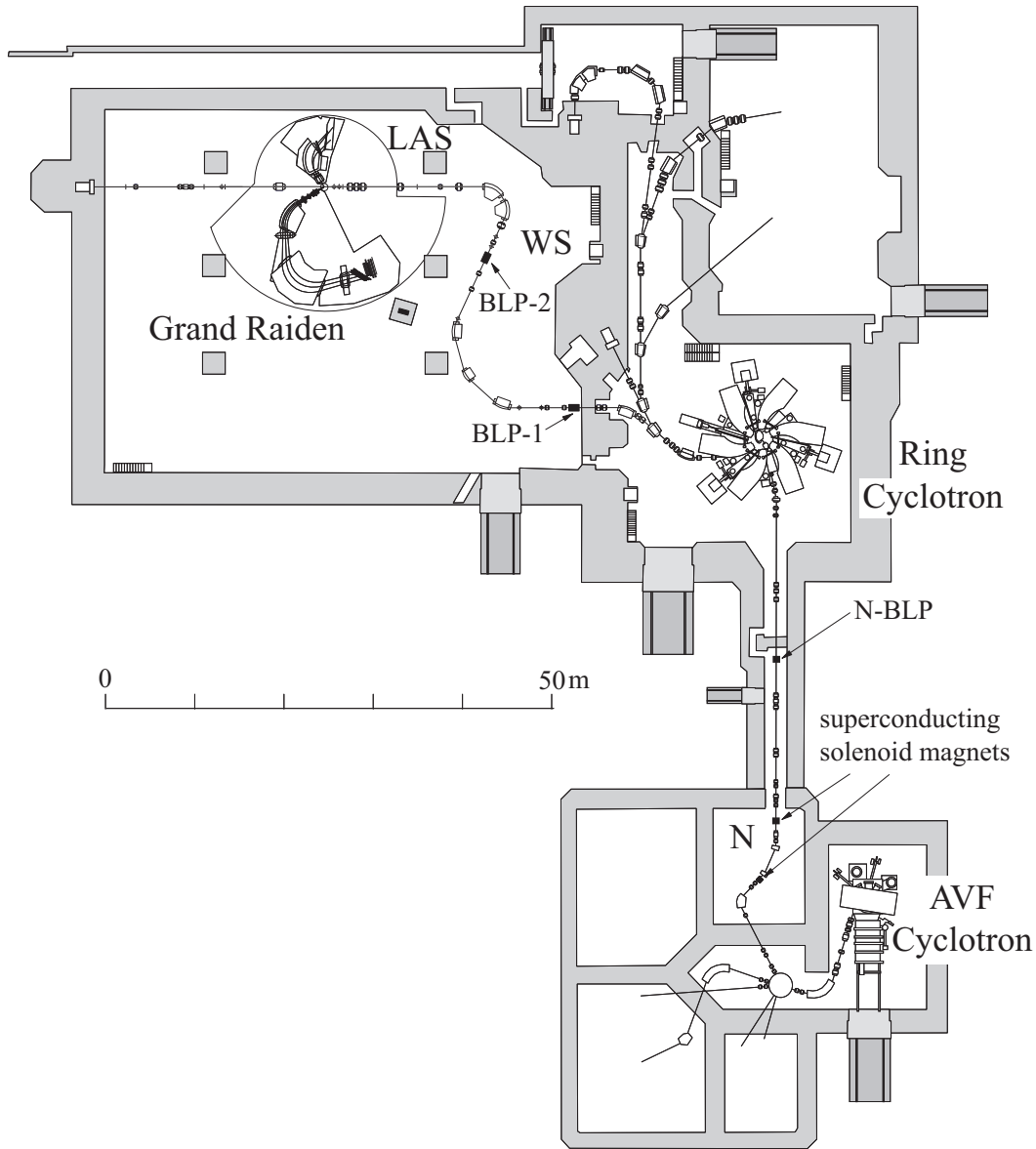
Figure 2.1: Schematic view of the RCNP ring cyclotron facility.

target nucleus before the scattering

Since the nucleon-momentum distribution in a nucleus is strongly related to the orbital angular momentum L, the recoil-momentum distribution of the cross section for the $(p, 2p)$ reaction predominantly depends on L. Because protons in the single-particle orbitals with $L \neq 0$ cannot have zero momentum in a nucleus, the cross sections for the knock-out reaction from the single-particle orbitals with $L \neq 0$ should have a minimum around $p_3 = 0$. On the other hand, the cross sections of the s-hole states ($L = 0$) have a maximum at $p_3 = 0$. Since the distribution of the cross section has characteristic behavior at $p_3 = 0$, the measurement around $p_3 = 0$ is essential.
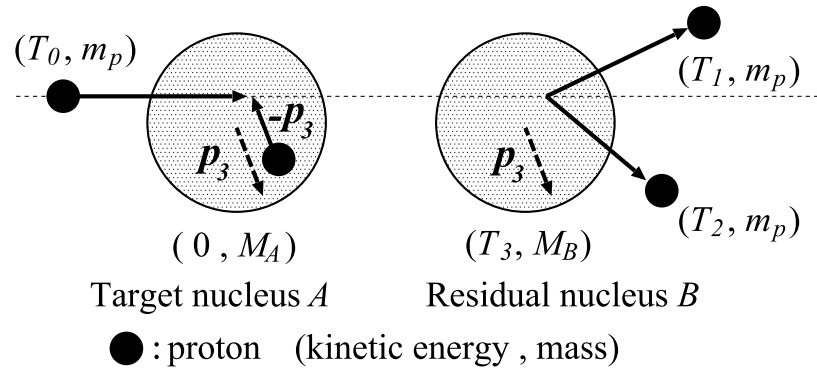
Figure 2.2: Notation for the kinematics of the $A(p, 2p)B$ reaction in the laboratory system. The incident energy of the proton is $T_0 = 392$ MeV in the present study. The recoil momentum of the residual nucleus B is indicated by p_3.

2.2 Experimental conditions

Some types of experiments have been performed until now. One of them is a symmetric experiment where the two outgoing protons have equal emerged angles and kinetic energies. Although this simple measurement condition is advantageous for the theoretical calculation, only a part of events measured by the counters satisfy this condition. When the kinetic energies of two ejected protons are kept fixed and the direction of an ejected proton is changed to measure the recoil momentum distribution, distorting potentials for the outgoing protons can be fixed and the uncertainty from the distortion potentials due to change of kinetic energies of protons can be decreased. In a so-called energy-sharing experiment, the directions of two ejected protons are kept fixed and the energies of them are varied. A large part of measured events can be used and it is easier to vary the recoil momentum by changing energies of ejected protons than changing the directions of protons.

Since the cross sections of deep-hole states are expected to be small, the experiments were performed under the energy-sharing condition in this work. The magnetic fields of the spectrometers and the angle of the LAS were varied, while the sum of the kinetic energies of the two measured protons $T_1 + T_2$ was kept constant at each separation energy. The directions of the ejected protons were set at asymmetric condition following the experiments at PNPI where the $1s$-hole states were identified in separation energy spectra by Volkov *et al.* The angle of the GR was fixed at $25.5°$. In order to separate the hole states, the recoil-momentum distributions of the cross section and the analyzing power were measured in the region of 0–200 MeV/c in the separation energy region of 0–89 MeV. The experimental parameters are listed in Table 2.1. The kinematical sets are grouped according to the range of the measured separation energies.

Table 2.1: Measured kinematical sets (central values). The angle of the GR was fixed at 25.5°. θ_{LAS} indicates the angle of the LAS which was set according to the measured separation-energy region.

	E_{sep} (MeV)		T_1 (MeV)	θ_{LAS} (deg)	T_2 (MeV)
Set 1	0–17	a	290.49	56.41	95.00
		b	270.20	56.41	115.29
		c	251.07	56.41	134.42
		d	233.22	56.41	152.27
Set 2	6–37	a	270.20	52.06	95.00
		b	251.07	52.06	114.13
		c	233.22	52.06	131.98
		d	218.25	52.06	146.95
Set 3	25–54	a	251.07	48.00	95.00
		b	233.22	48.00	112.85
		c	218.25	48.00	127.82
		d	203.70	48.00	142.37
Set 4	40–75	a	233.22	44.26	95.00
		b	218.25	44.26	109.97
		c	203.70	44.26	124.52
		d	189.00	44.26	139.22
Set 5	56–89	a	218.25	41.18	95.00
		b	203.70	41.18	109.55
		c	189.00	41.18	124.25
		d	175.00	41.18	138.25

2.3   Experimental setup

2.3.1   Beam transportation and target

A polarized proton beam was provided by a high intensity polarized ion source (HIPIS) [51] and was injected to the $K = 120$ MeV AVF (Azimuthally Varying Field) cyclotron. At the same time, the polarization axis was adjusted to the vertical direction by bending the beam with both an electrostatic deflector and a bending magnet. The direction of the beam polarization was reversed every second by switching the strong and weak transition units of the HIPIS, alternatively. The proton beam was accelerated to the energy of 64.2 MeV by AVF cyclotron and further accelerated to 392 MeV by the $K = 400$ MeV ring cyclotron [52]. The proton beam extracted from the ring cyclotron was achromatically transported to the target in the scattering chamber through the WS beamline [53]. The beam spot size at the target point was typically 1 mm in diameter. After passing through the target, the beam was transported into a Faraday cup in the shielding wall. The beam current collected in the Faraday cup was

monitored with a current digitizer (model 1000C) from Brookhaven Instruments Corporation.

The beam polarization was continuously monitored using a beam-line polarimeter (BLP) system using a polyethylene target. In the polarimeter system, kinematical coincidence was used to select p-H scattering from $(CH_2)_n$ foil. A pair of protons scattered to the opposite directions in the center of mass system are detected in coincidence by a pair of the scintillation detectors. Two pairs of the scintillation detectors (L–L' and R–R' pairs) were placed in the horizontal plane to measure left/right scattering asymmetry as shown in Fig. 2.3. The other pairs were arranged in the vertical plane to measure up/down scattering asymmetry. The scintillation detectors were placed at the laboratory angles of 17.0° and 69.7° where the value of the analyzing power for pp-scattering is nearly maximum at this injection energy. Delayed coincidence events between different beam bunches were also measured to estimate the numbers of accidental coincidence protons. Beam polarization of 60–70% was achieved in the experiment.

The calcium targets were made from a natural calcium block. Pieces of the calcium block were rolled thin and they were cut into the rectangular shapes with 20 mm × 30 mm. As calcium is an easily oxidizable metal, the pieces of calcium block were soaked in liquid paraffin when they were rolled and stored. The targets used in the measurements were two sheets of calcium foil with thicknesses of 53 and 24 mg/cm^2. The thickness of 24 mg/cm^2 was normalized to the thicker target with the thickness of 53 mg/cm^2 by comparing the cross sections in some kinematical regions. The thickness of 24 mg/cm^2 was thinner than the value of 27 mg/cm^2 estimated from its area and weight during the preparation. The uncertainty of the target thickness was probably due to matter of its uniformity. Assuming that the thicker target had the same amount of uncertainty due to the matter of its uniformity, the target with a thickness of 53 mg/cm^2 has the uncertainty of 6%. The uncertainty of the thickness of 24 mg/cm^2 was estimated as 6% combining the uncertainty of the normalization factor. The targets used in the
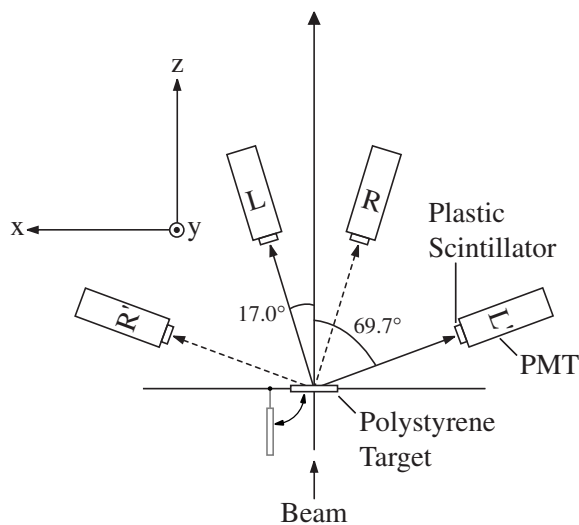

Figure 2.3: Layout of BLP.

Table 2.2: Targets used in the measurements.

Number	Experiment	thickness	thickness (Normalized)	uncertainty
1	E168	53 mg/cm^2	—	6%
2	E217	27 mg/cm^2	24 mg/cm^2	6%

measurements were summarized in Table 2.2. The oxygen contamination was estimated from elastic scattering and was less than 1% relative to calcium in weight.

2.3.2 Dual spectrometer system

Scattered protons were analyzed with the dual-spectrometer system, the Grand Raiden spectrometer (GR) [54, 55] and the large-acceptance spectrometer (LAS) [56, 57]. A schematic view of the system is shown in Fig. 2.4.

The GR was designed and constructed for high-resolution measurements with a momentum resolution $p/\delta p$ = 37000. The design specifications are listed in Table 2.3. The GR consists of three dipole magnets (D1, D2, and DSR), two quadrupole magnets (Q1 and Q2), a sextupole magnet (SX), and a multipole magnet (MP) as shown in Fig. 2.4. The second order ion-optical properties like the tilting angle of the focal plane are adjusted by the SX magnet, and higher-order aberrations are minimized by the MP magnet and the curvatures of the pole edges at the entrance and exit of the dipole magnets. The
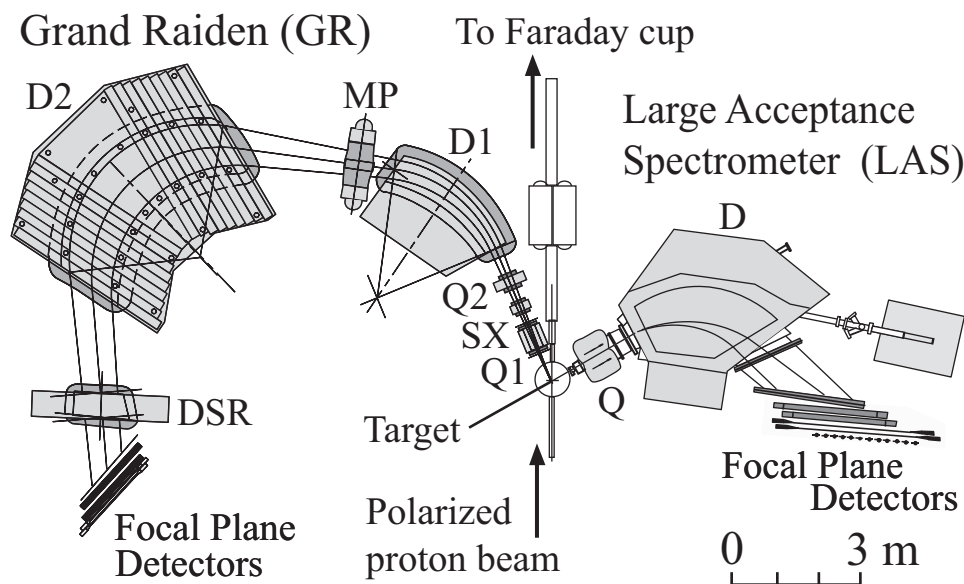
Figure 2.4: Schematic view of the dual-arm spectrometer system at RCNP.

Table 2.3: Design specification of the Grand Raiden spectrometer (GR).

Mean orbit radius	3 m
Total deflection angle	162°
Range of the setting angle	−4° to 90°
Momentum range	5%
Momentum dispersion	15.45 m
Momentum resolution ($p/\Delta p$)	37,000 [a]
Tilting angle of focal plane	45°
Focal plane length	120 cm
Maximum magnet rigidity	5.4 T·m
Maximum field strength (D1, D2)	1.8 T
Maximum field gradient (Q1)	0.13 T/cm
Maximum field gradient (Q2)	0.033 T/cm
Horizontal magnification ($x|x$)	-0.417
Vertical magnification ($y|y$)	5.98
Horizontal angle acceptance	±20 mrad
Vertical angle acceptance	±70 mrad
Maximum solid angle	4.3 msr
Flight path of the central ray	20 m

[a]The source width is assumed to be 1 mm.

third dipole magnet (DSR) required for in-plane polarization transfer measurements was not used in the present experiment. The LAS is the second arm spectrometer with a resolution $p/\delta p = 5,000$. It was designed to have a large solid angle ($\approx$20 msr) and a wide momentum acceptance (30%). The design specifications are listed in Table 2.4. The LAS consists of a quadrupole (Q) and a dipole magnet (D).

2.3.3 Focal-Plane detectors of GR and LAS

The two scattered protons were detected with the focal plane detectors at each spectrometer. Each focal plane detector consists of two plastic scintillation counters and two vertical-drift-type multiwire-drift chambers (MWDCs).

The focal plane detector system of the GR consists of two MWDCs and two planes of plastic scintillators, as illustrated in Fig. 2.5. The type of any plane of the MWDCs is, so-called, a vertical drift chamber (VDC), in which electrons and ions drift perpendicularly to the anode plane [58]. Specification of the GR-MWDCs are summarized in Table 2.5. Each MWDC has two anode wire planes (X and U), sandwiched between three cathode planes. Anode planes include sense wires and potential wires. The structure of an X-wire plane is schematically illustrated in Fig. 2.6. The wire configurations of the X and U planes of the GR-MWDC are shown in Fig. 2.7. It should be noted that the spacing of sense wires are different between X-plane (6 mm) and U-plane (4 mm) for the GR-MWDCs. The potential wires serve to make a uniform electric field between the cathode plane and the anode plane. High voltages of -300 V

Table 2.4: Design specification of the Large Acceptance Spectrometer (LAS).

Mean orbit radius	1.75 m
Total deflection angle	70°
Range of the setting angle	0° to 130°
Momentum range	30%
Momentum resolution ($p/\Delta p$)	5,000
Tilting angle of focal plane	~ 57° [a]
Focal plane length	170 cm
Maximum magnet rigidity	3.22 T·m
Maximum field strength (D)	1.6 T
Maximum field gradient (Q)	-74 mT/cm
(Sextupole component)	0.465 T/cm^{2}m
(Octupole component)	0.029 T/cm^{3}m
Horizontal magnification ($x|x$)	-0.40
Vertical magnification ($y|y$)	-7.3
Horizontal angle acceptance	±60 mrad
Vertical angle acceptance	±100 mrad
Maximum solid angle	~20 msr
Flight path of the central ray	6.2 m

[a]The value is given for the high momentum end (δ = +15%).
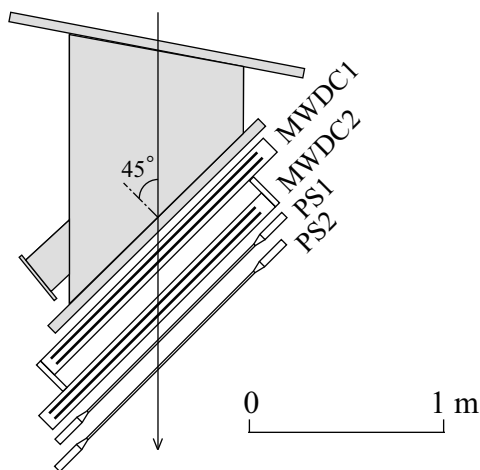
Figure 2.5: Focal plane detectors of the GR.

were applied to the potential wires in both planes and -5.6 kV to the cathode planes of the MWDCs. The sense wires were grounded (0 V). The gas multiplications by avalanche processes are only occurred near the sense wires. Mixture gas of argon (71.4%), iso-butan (28.6%), and iso-propyl-alcohol was used. The iso-propyl-alcohol in the vapor pressure at 2°C was mixed in the argon gas in order to reduce the deterioration due to the aging effect like the polymerizations of gas at the wire surface. Signals from

the anode wires were pre-amplified and discriminated by LeCroy 2735DC cards, which were directly connected on the printed bases of the MWDCs without cables. Output ECL signals of the 2735DC cards were transferred to LeCroy 3377 TDCs, in which information on the hit timing of each wire was digitized.
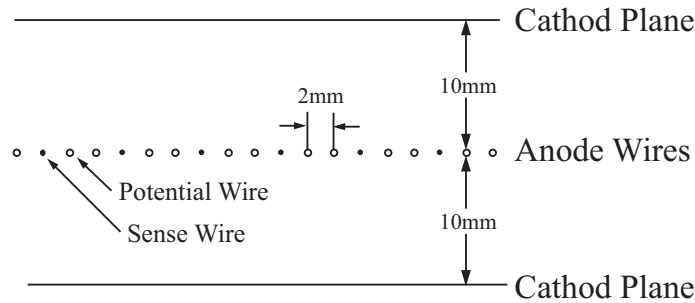
Figure 2.6: Structure of each plane of MWDC.
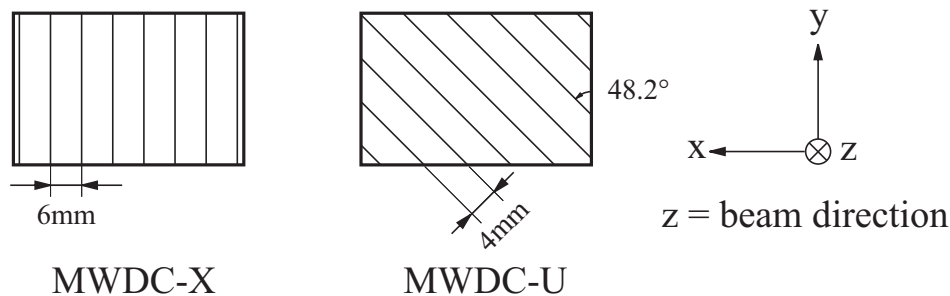
Figure 2.7: Wire configurations of the X-plane and U-plane of the GR-MWDC.

The GR drift chambers were backed by two plastic scintillation counters, the size of which is 1200^{W} mm $\times\ 120^{H}$ mm $\times\ 10^{t}$ mm. The scintillation light was detected by photo-multiplier tubes (HAMAMATSU H1161) at both sides of the scintillators. Signals from these scintillators were used to generate a trigger signal of the GR event. An aluminum plate with a thickness of 10 mm was placed between two scintillators in order to prevent the secondary electrons produced in one scintillator from hitting another scintillator.

The focal plane detector system of the LAS consists of two MWDCs and two planes of plastic scintillators. The detector layout is shown in Fig. 2.8. In order to cover the vertically broad focal plane of the LAS, both scintillator planes consist of three (up, middle, and down) scintillation counters, which are 2000^{W} mm $\times\ 150^{H}$ mm with a thickness of 6mm respectively. Fast photo-multiplier tubes (HAMA-MATSU H1949) were used on both sides of each scintillator. Aluminum plates with a thickness of 3 mm were placed between the scintillator planes for the same purpose as the GR side.

The LAS-MWDCs are similar to those for the GR, except for the size and wire configuration. Although each MWDC consists of three anode planes (X, U, and V), the V-plane has not been used owing to the lack of the readout electronics. The wire configurations of the X and U planes of the LAS-MWDC are shown in Fig. 2.9. A high voltage of -5.4 kV was supplied to the cathode plane, and -300 V to the potential wires. The specification of the LAS-MWDCs is summarized in Table 2.6.
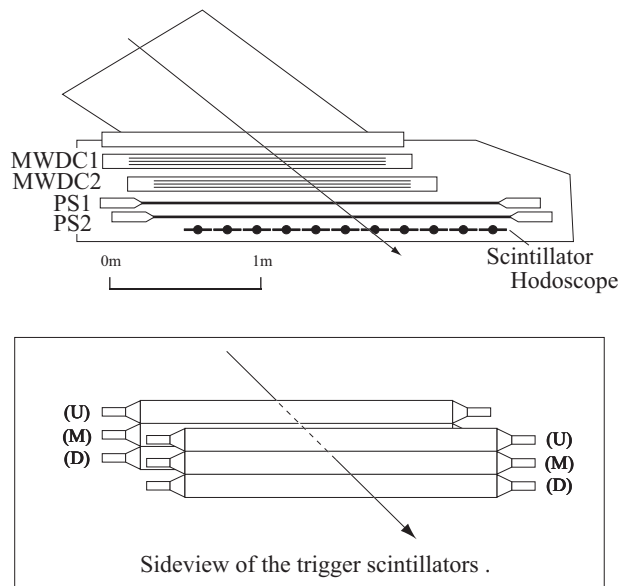

Figure 2.8: Focal plane detectors of the LAS.

2.3.4   MWPC for scattering angles

Two multiwire proportional chambers (MWPCs) were newly installed at the entrances of the GR and LAS to acquire the vertical-scattering-angle information which cannot be precisely determined from measurements in the focal planes of the spectrometers owing to their ion-optical properties. The precise measurement of the scattering angles is important in calculating the recoil momentum of the residual nucleus. The layout around the scattering chamber and the geometrical relation of anode planes and the center of the scattering chamber are illustrated in Figs. 2.10 and 2.11. The specification of the MWPCs are summarized in Table. 2.7. The structure of an anode-wire plane is schematically illustrated in Fig. 2.12. The MWPCs consist of two horizontal wire planes (X, X') and two vertical wire planes (Y, Y') whose wire pitch is 2.02 mm. Typically, one or two wires were hit per plane for one trajectory of a charged particle. The counter gas was a mixture of argon (66%), iso-butane (33%), freon (0.3%), and iso-propyl-alcohol (vapor pressure at $2°C$). High voltages of -4.9 kV and -4.7 kV were applied to the cathode planes of the MWPC for the GR and LAS, respectively. Signals from the anode wires were pre-amplified and discriminated by Nanometric N277-C3 cards or preamp-cards by REPIC. The wire-hit pattern was converted into the central position and the number of the hit wires for every cluster by the LeCroy PCOS III system.

Table 2.5: Specifications of the MWDCs for the GR.

Wire configuration	X (0°=vertical), U (48.2°)
Active area	1150^W mm × 120^H mm
Number of sense wires	192 (X), 208 (U)
Cathode-anode gap	10 mm
Anode wire spacing	2 mm
Sense wire spacing	6 mm (X), 4 mm (U)
Sense wires	20 μmϕ gold-plated tungsten wire
Potential wires	50 μmϕ beryllium-copper wire
Cathode	10 μm-thick carbon-aramid film
Cathode voltage	-5.6 kV
Potential-Wire Voltage	-300 V
Gas mixture	Argon (71%)+Iso-butane (28.6%)
	+Iso-propyl-alcohol (2°C vapor pressure)
Entrance and exit window	12.5 μm-thick aramid film
Distance between two MWDCs	250 mm
Pre-amplifier	LeCroy 2735DC

Table 2.6: Specifications of the MWDCs for the LAS.

Wire configuration	X (0°=vertical), U (31°), V (−31°)
Active area	1700^W mm × 350^H mm
Number of sense wires	272 (X), 256 (U), 256 (V)
Cathode-anode gap	10 mm
Anode wire spacing	2 mm
Sense wire spacing	6 mm
Sense wires	20 μmϕ gold-plated tungsten wire
Potential wires	50 μmϕ beryllium-copper wire
Cathode	10 μm-thick carbon-aramid film
Cathode voltage	-5.4 kV
Potential-Wire Voltage	-300 V
Gas mixture	Argon (71%)+Iso-butane (28.6%)
	+Iso-propyl-alcohol (2°C vapor pressure)
Entrance and exit window	25 μm-thick aramid film
Distance between two MWDCs	164 mm
Pre-amplifier	LeCroy 2735DC
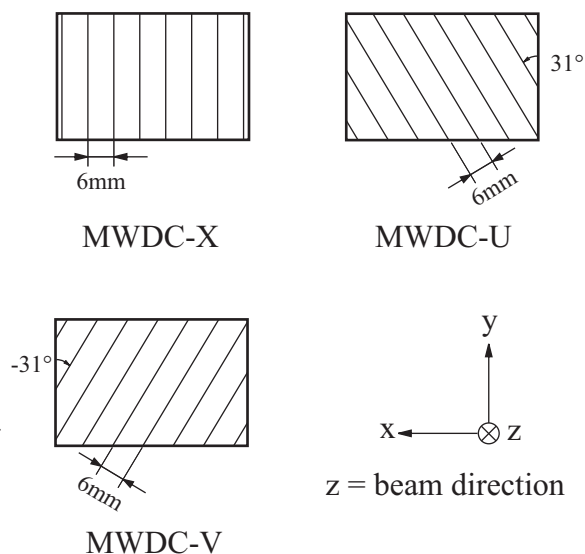
Figure 2.9: Wire configurations of the X-plane, U-plane, and V-plane of the LAS-MWDC.

The collimators made of lead were placed in front of the MWPCs for both of the spectrometers.

Table 2.7: Specifications of the MWPCs for the GR and LAS.

	GR	LAS
Wire configuration	X ($0°$=vertical), Y ($90°$=horizontal)	
Active area	30^W mm $\times$ 62^H mm	94^W mm $\times$ 158^H mm
Number of sense wires	16 (X), 32 (Y)	48 (X), 80 (Y)
Cathode-anode gap	6.4 mm	
Anode wire spacing	2.02 mm	
Sense wires	20 μmϕ gold-plated tungsten wire	
Guard wires	50 μmϕ Beryllium-Copper wire	
Cathode	6 μm-thick carbon-aramid film	
Cathode voltage	-4.9 kV	-4.7 kV
Gas mixture	Argon (66%)+Iso-butane (33%)+Freon (0.3%)	
	+Iso-propyl-alcohol ($2°$C vapor pressure)	
Entrance and exit window	50 μm-thick aramid film	
Pre-amplifier		

2.3.5   Trigger and data acquisition system

The data acquisition was initiated by the trigger signals from the GR and LAS scintillators. The readout electronics and trigger systems of the focal plane scintillators for the GR and LAS are illustrated in
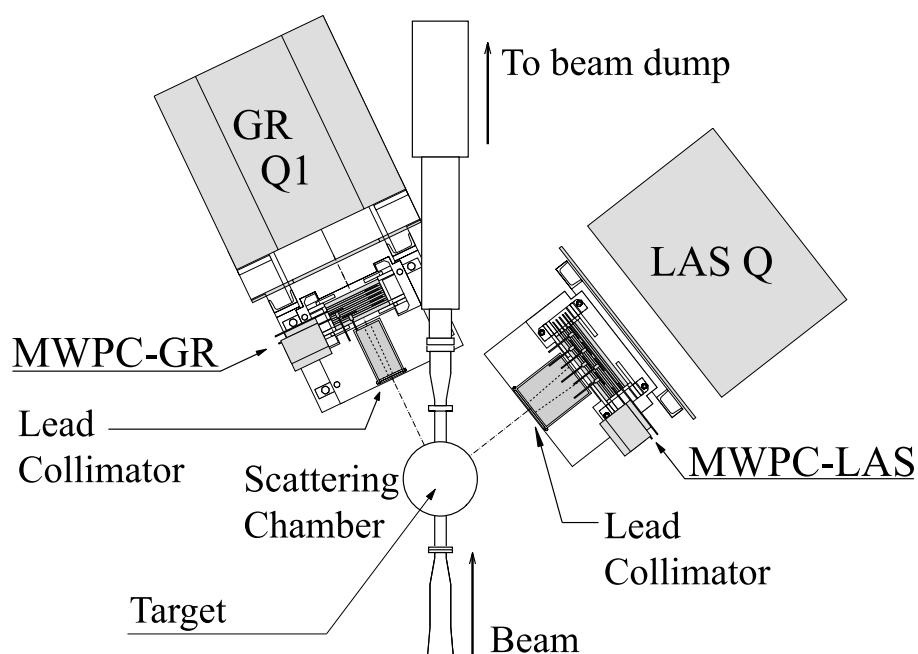
Figure 2.10: Schematic view of the layout around the scattering chamber. The proton beam is injected into the reaction target at the center of the scattering chamber and is transported to the Faraday cup placed about 25 m downstream of the target. The MWPCs and the lead collimators are installed in front of the quadrupole magnets.

Fig. 2.13 and Fig. 2.14, and were placed near the focal planes of the GR and LAS, respectively. Any output of photomultiplier tube (PMT) was first divided into two signals and one was discriminated by a constant fraction discriminator (CFD) and the other was sent to a FERA (Fast Encoding Readout ADC (analog-to-digital converter);LeCroy 4300B) module. One of the CFD outputs was transmitted to the TDC (time-to-digital converter) system that consists of TFCs (Time to FERA Converter;LeCroy 4303) and FERAs. A coincidence signal of two PMT-outputs on both sides of the same scintillator was generated by a Mean-Timer circuit, in which the times of two signals were averaged. Thus, the position dependence of output timing caused by the difference of the propagation time in the long scintillator was minimized.

The trigger system was constructed with LeCroy 2366 universal logic modules (ULM) with field programmable gate-array (FPGA) chips. As shown in Figs. 2.13 and 2.14, the trigger system received signals from the outputs of Mean Timers and generated the GR and LAS trigger under the condition that signals from PS1 and PS2 coincide internally. In the LAS, PS1 or PS2 was generated when there was at least one signal of three Mean Timer outputs corresponding to up, middle, and down scintillators. The GR trigger gave the gate signals of ADC modules and start signals of TDC modules for the GR focal plane detectors, while the LAS trigger was used as the ADC gate signals and the TDC start signals for the LAS focal plane detectors. The coincidence trigger of the GR and LAS was also generated in the 2366 module at the GR side, where the output timing was determined by the LAS trigger. The logic diagram for coincidence event of the GR and LAS is shown in Fig. 2.15. The $(p, 2p)$ event was
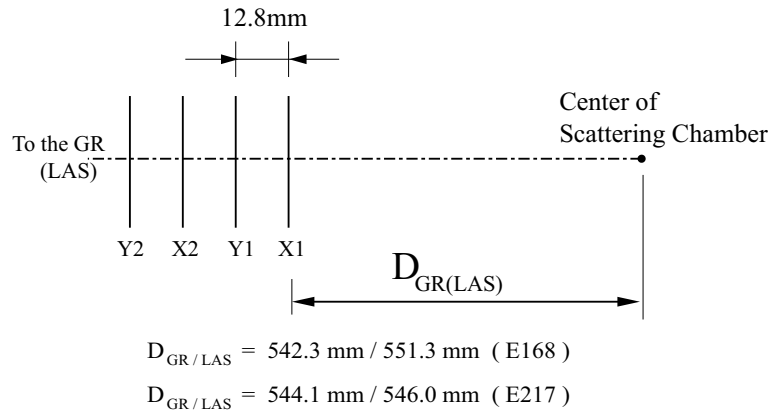
Figure 2.11: Geometrical relation of anode planes of the MWPC and the center of the scattering chamber.
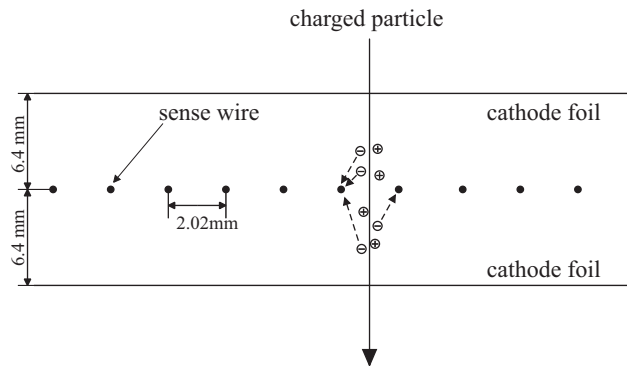
Figure 2.12: Structure of each wire plane of the MWPCs.

measured by GR+LAS coincidence mode, and a GR single event and a LAS single event were also measured under the sampling condition. The main trigger output started the data acquisition system.

A schematic diagram of the data acquisition (DAQ) system [59, 60] is shown in Fig. 2.16. The digitized data of the TDCs and ADCs for the detectors were transferred in parallel via the ECL bus to the high speed memory modules (HSM) in the VME crate. The flow controlling event tagger module (FCET) [61], that was installed in each CAMAC crate for TDCs and ADCs, attaches the event header, event number, and input register words to the data from the LeCroy FERA and FERET system for the subsequent event reconstruction, and transfers the data via the ECL bus. Similarly, the rapid data transfer module (RDTM) [62] manages the data from the LeCroy PCOS III system. The CAMAC actions are excluded in this data transfer process. In the present measurements, the DAQ system treated the data from the GR-MWDCs, the GR-scintillators, the LAS-MWDCs, the LAS-scintillators, and the MWPCs for the GR and LAS, in parallel. Each transfer line has two HSMs, which work as a double-buffer and reduce dead time in transferring buffered data.

The stored data in the HSMs were moved to a reflective memory module of RM5576 through the

VME bus by an MC68040 based CPU board, and the data in the RM5576 was automatically copied to another RM5576 module in the counting room through the link of optical fiber cables. A SUN workstation read the data from the RM5576 in the counting room and transferred them to an IBM RS/60000 workstation via an FDDI network. This data transfer method with reflective memory modules and optical fiber cables was used in the beamtime of E168. In the beamtime of E217, new data transfer method, which directly transfers the data to the workstation by a gigabit Ethernet, was installed and used. The data was stored in the large hard disk connected to the workstation. The event reconstruction and online data analysis were also performed on this computer.

Beam current was adjusted so that the live time of the DAQ system was kept at almost 80–90%.
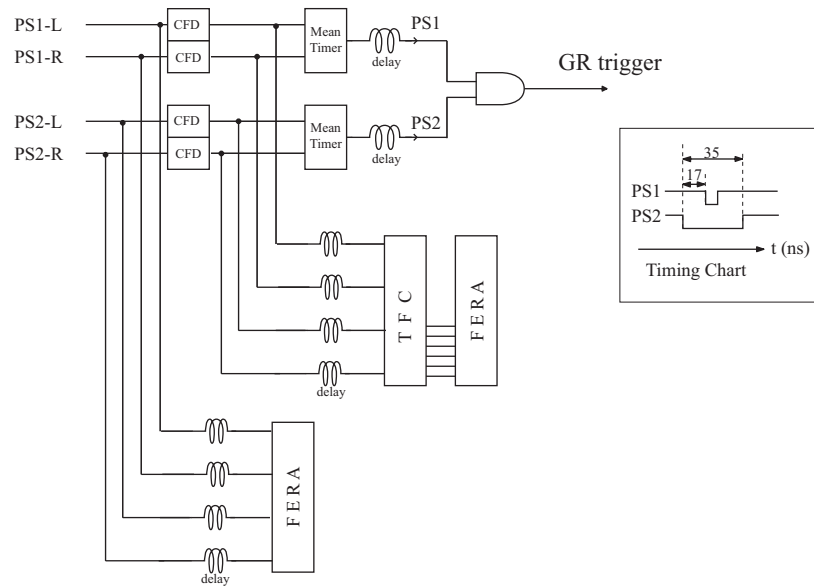
Figure 2.13: Logic diagram for the GR focal plane detectors.
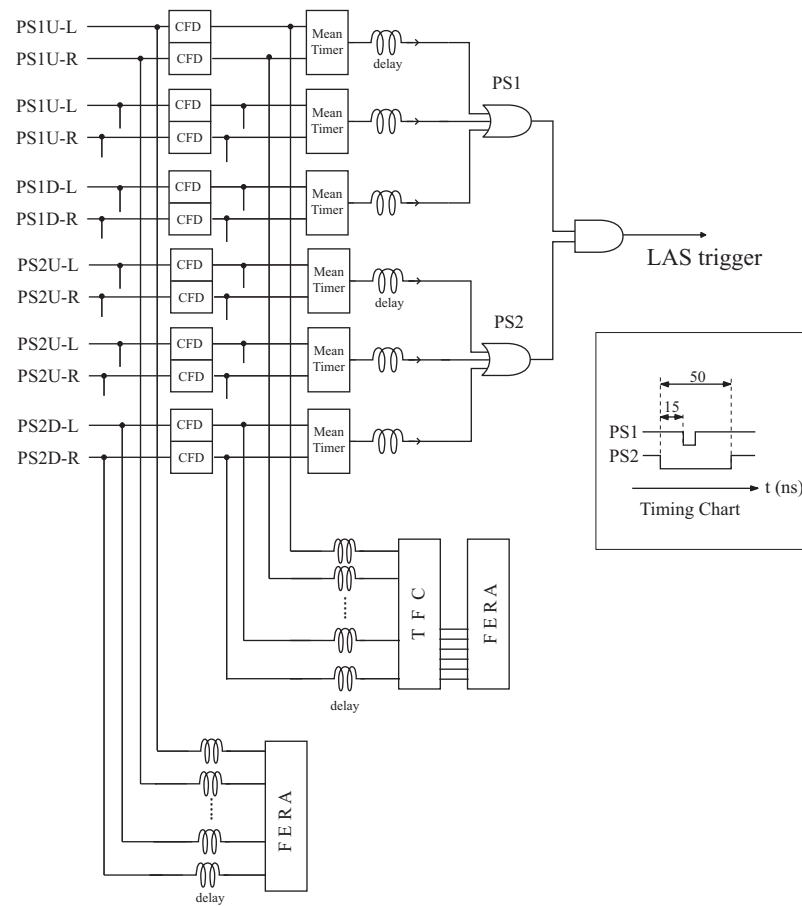
Figure 2.14: Logic diagram for the LAS focal plane detectors.
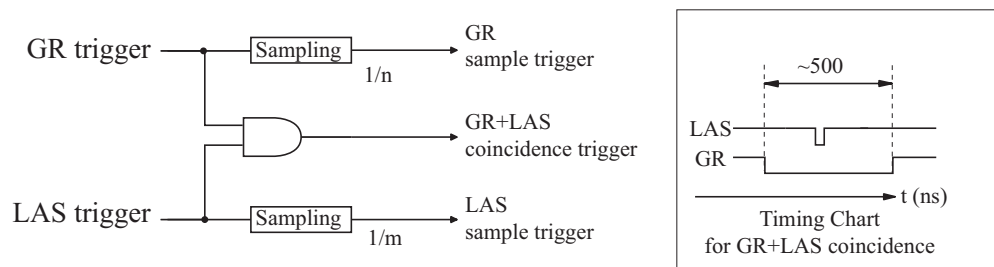
Figure 2.15: Logic diagram for coincidence event of the GR and LAS.
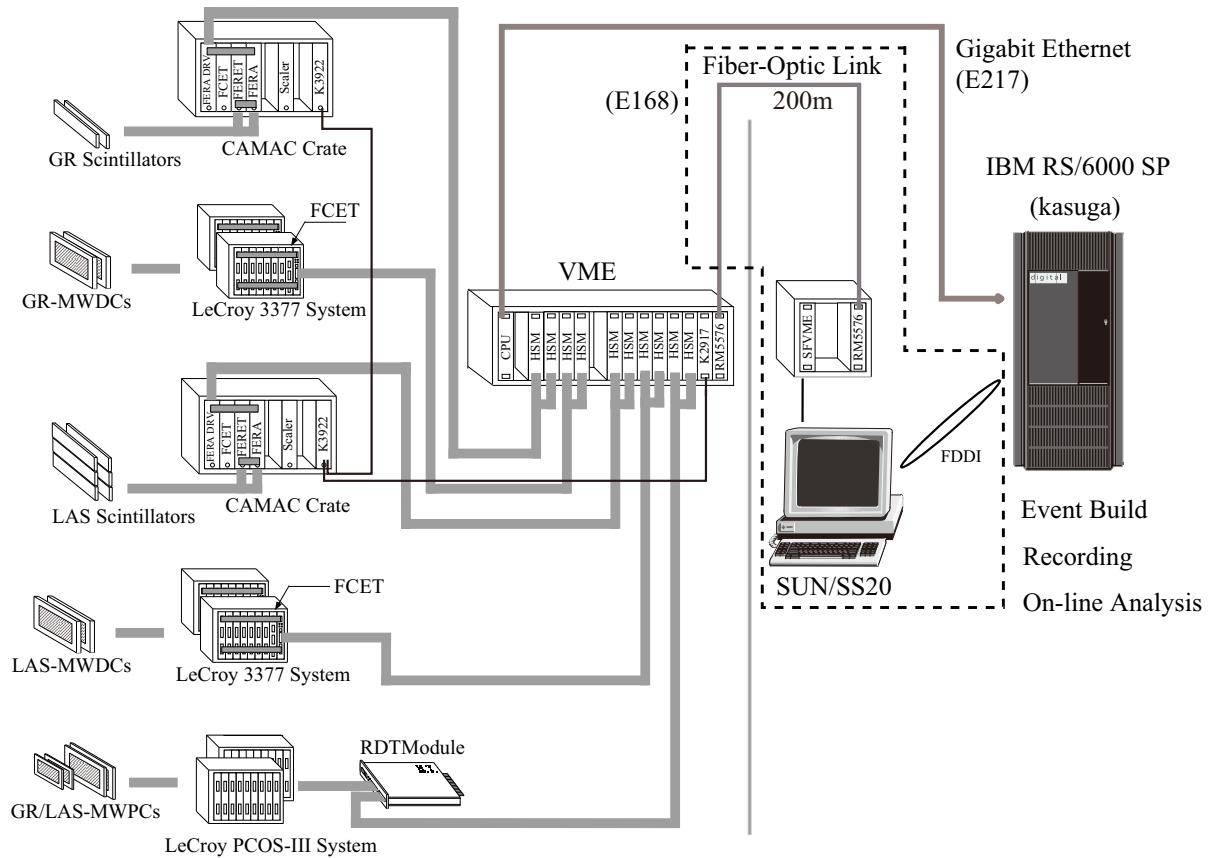
Figure 2.16: Schematic view of the data acquisition system.

Chapter 3

Data Reduction

A program code 'Yosoi analyzer' has been developed for analyzing experimental data obtained with the GR and/or LAS spectrometer system at RCNP. The analyzed results were stored in a HBOOK [63] file and graphically displayed using a program PAW [64]. The data analysis was mainly carried out by using the central computer system at RCNP, that is, IBM RS/6000SP system.

3.1 Polarization of proton beam

The beam polarization was measured by using the beam-line polarimeter 1 (BLP1) located at the first straight beam-line section in the west experimental hall. The BLP2 was used for monitoring the transmission and polarization of the beam.

Yield (N_L (N_R)) in coincidence by the pair of scintillators of L(R) and L'(R') in Fig. 2.3 for spin-up ($\uparrow$) and spin-down ($\downarrow$) modes are described as

$$N_L^\uparrow = N_L^{p\uparrow} - N_L^{a\uparrow} = \sigma_0(\theta_L)N_t N_b^\uparrow \epsilon_L \Delta\Omega_L(1 + A_y(\theta_L)p_y^\uparrow), \tag{3.1a}$$

$$N_R^\uparrow = N_R^{p\uparrow} - N_R^{a\uparrow} = \sigma_0(\theta_R)N_t N_b^\uparrow \epsilon_R \Delta\Omega_R(1 - A_y(\theta_R)p_y^\uparrow), \tag{3.1b}$$

$$N_L^\downarrow = N_L^{p\downarrow} - N_L^{a\downarrow} = \sigma_0(\theta_L)N_t N_b^\downarrow \epsilon_L \Delta\Omega_L(1 - A_y(\theta_L)p_y^\downarrow), \tag{3.1c}$$

$$N_R^\downarrow = N_R^{p\downarrow} - N_R^{a\downarrow} = \sigma_0(\theta_R)N_t N_b^\downarrow \epsilon_R \Delta\Omega_R(1 + A_y(\theta_R)p_y^\downarrow). \tag{3.1d}$$

The superscripts of $\uparrow$ and $\downarrow$ represent the quantities in spin-up ($\uparrow$) and spin-down ($\downarrow$) modes. N^p and N^a are the numbers of prompt and accidental coincidence events, $\sigma_0(\theta)$ and $A_y^{\text{eff}}(\theta)$ are the unpolarized cross section and the analyzing power for $p + p$ scattering. N_t and N_b are the numbers of the target and beam particles. p_y, ϵ and $\Delta\Omega$ are the beam-polarization in the vertical direction, the efficiency, and the solid angle of each scintillation detector, respectively. The accidental coincidence event N^a was estimated using the number of forward counter L(R) event coincident with the event of backward counter L'(R') in the next beam bunch.

The angular acceptances of the polarimeter were determined by collimating the backward protons.

If there is no instrumental asymmetry, namely $\epsilon_L \Delta \Omega_L = \epsilon_R \Delta \Omega_R = \epsilon \Delta \Omega$, the beam polarization can be expressed as follows;

$$p^\uparrow = \frac{1}{A_y(\theta)} \frac{2Q - (L + R)}{L - R} \tag{3.2a}$$

$$p^\downarrow = \frac{1}{A_y(\theta)} \frac{2/Q - (L^{-1} + R^{-1})}{R^{-1} - L^{-1}}. \tag{3.2b}$$

$$L = \frac{N_L^\downarrow}{N_L^\uparrow}, \quad R = \frac{N_R^\downarrow}{N_R^\uparrow}, \quad Q = \frac{N_b^\downarrow}{N_b^\uparrow} \tag{3.3}$$

The scattering angles of forward and backward protons for a 392 MeV proton beam were set at $\theta_{lab} = 17°$ and $\theta_{lab} = 69.7°$, respectively, The effective analyzing power of $A_y(17°) = 0.44 \pm 0.01$ for pp scattering from the polyethylene target was used in Eq. (3.2) to determine the beam polarization. This value of $A_y(17°)$ for 392 MeV was previously calibrated in comparison with two polarization values measured before and after the ring cyclotron for a vertically polarized proton beam. The beam polarization before the acceleration by the ring cyclotron, which was measured by BLP-N between the AVF and ring cyclotrons, was determined from the asymmetry for the $^{12}C(p, p)$ elastic scattering with the analyzing power data of the $^{12}C(p, p)$ elastic scattering measured at RCNP [65]. The beam polarization of 60–70% was achieved in the experiments.

3.2   Particle Identification

Combination of the time of flight (TOF) through the spectrometer and the energy deposition to the plastic scintillator (ΔE) provided the particle identification at the focal plane of the spectrometers. Photons from the scintillators were detected by PMTs attached on both the left and right sides. The photon number is attenuated owing to the absorption by the scintillator material during the transmission. The photon number I can be described as a function of the path length x,

$$I(x) = I_0 \exp \left(-\frac{x}{l} \right), \tag{3.4}$$

where I_0 is the initial photon numbers and l is the attenuation length of the scintillator material. Suppose the distances between the emitting point of the photons and the left/right PMTs are x_L and x_R, the geometrical mean $\bar{I}$ of the photon numbers at both sides is

$$\bar{I} = \sqrt{I_0 \exp \left(-\frac{x_L}{l} \right) \cdot I_0 \exp \left(-\frac{x_R}{l} \right)} = I_0 \exp \left(-\frac{x_L + x_R}{2l} \right) = I_0 \exp \left(-\frac{L}{2l} \right). \tag{3.5}$$

where $L = x_L + x_R$ is the length of the scintillator. Eq. (3.5) shows that $\bar{I}$ is independent on a position where a particle hits and becomes a good measure of energy deposition to the scintillator. Since the energy loss of the charged particles in the scintillator material is described by the well-known Bethe-Bloch formula, the $\bar{I}$ spectra are useful for the particle identification. Figure.3.1 shows the ΔE signal from PS1 of the GR. The peaks corresponding to protons and deuterons are recognized.
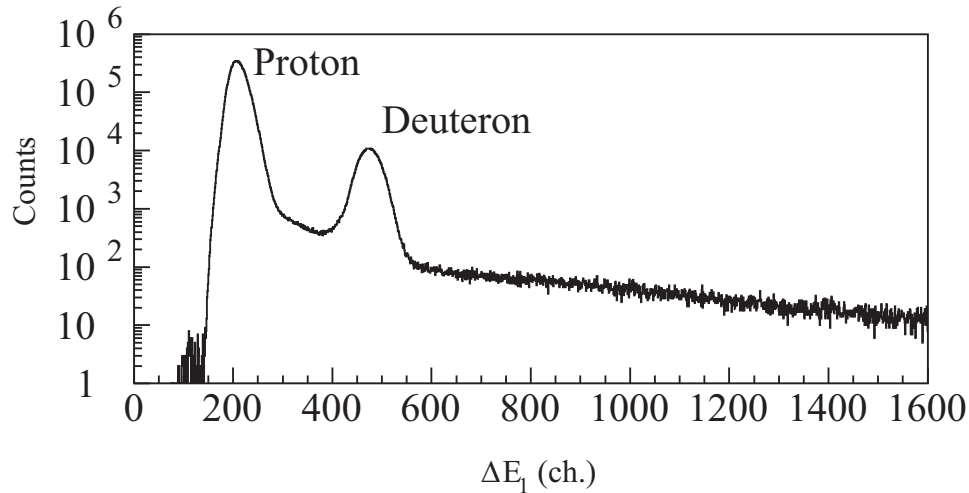
Figure 3.1: Energy loss spectrum for the PS1 of the GR, which is the mean of the pulse-height signals of the left and right PMTs.
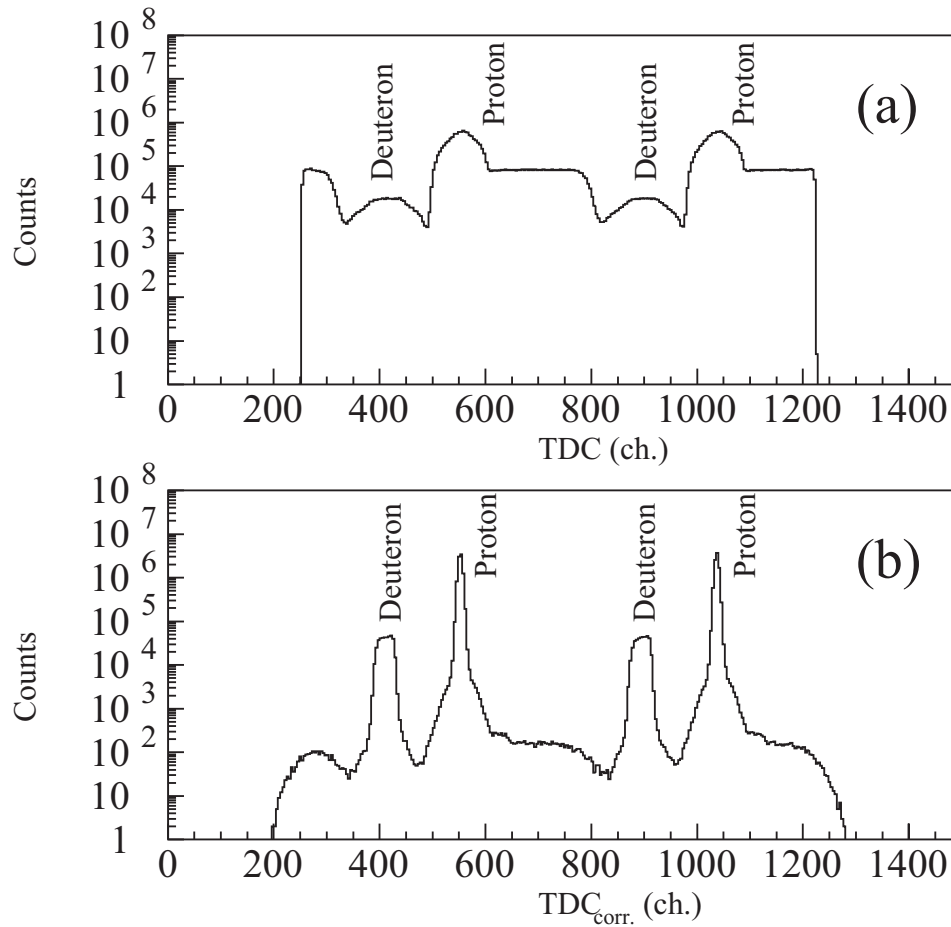
Figure 3.2 (a) shows the TDC spectrum that indicates the time difference between the mean-time signal from PS1 of the GR and the RF signal from the ring cyclotron. The RF signal, which was filtered at the half rate with a rate divider module, stopped the TDC and provided a periodic spectrum. Both of the two prominent peaks at 550 ch and 1050 ch in Fig 3.2 (a) indicate the spectra for proton trigger events, and the difference between the two peaks in TDC channel corresponds an interval of 60-ns period between beam bunches. The influence of the momentum acceptance of the spectrometer in the TDC spectrum was corrected by using the trajectory angle and the position at the focal plane, as seen in Fig. 3.2 (b). The time difference between the mean-time signal of a scintillator and the RF signal from the ring cyclotron reflects the time that the scattered particle takes to reach the scintillator from the target through the spectrometer. Since the particles have different velocities that depend on their masses under the same momentum condition, the TDC spectra for this time difference provides information on the masses of the particles.

Protons were identified by setting gates on the TDC spectra because the ΔE peak of proton has a long tail at higher ΔE region. The ΔE spectra for the PS1 scintillator was also used for the particle identification to eliminate the γ-ray contribution. These gates identifying proton are schematically displayed in the two-dimensional scatter plot of the corrected TDC and ΔE of the GR in Fig. 3.3. The proton identification of the LAS was performed in the identical way.

In the analysis of the set1a and a part of the set2a in Table 2.1, however, proton events were identified only with the ΔE spectra because the TDC data was not available owing to a trouble. In the part of the set2a where the TDC information was available, both of the particle identification were compared, and the yield identified with only the ΔE spectra was 0.5% smaller than that with the TDC and ΔE spectra. Since the ΔE spectra for the PS1 at the set1a shows a similar shape to that at the set2a, the influence of the lack of the TDC data for the particle identification at the set1a is expected to be as small as that at

Figure 3.2: (a): TDC spectrum that indicates the time difference between the mean-time signal from the PS1 of the GR and the RF signal from the AVF cyclotron. The RF signal was filtered at the half rate. (b): TDC spectrum corrected by the trajectory angle and the position at the focal plane so that the influence of the momentum acceptance of the spectrometer on the TDC is eliminated.

set2a.

3.3   Subtraction of accidental coincidences

The proton beam from the cyclotron has a time structure of approximately 60-ns period between bunches. To estimate the yield of accidental events, coincidence between the signals of the GR and LAS from adjacent beam bunches was allowed by increase in the width of the trigger signal of the GR. The yield of the true $(p, 2p)$ events, which must originate from the same beam bunch, was estimated by subtracting the yield of the accidental events from the yield of the coincident events in the same beam bunch.

A TDC spectrum for the time difference between the trigger signals of the GR and LAS is shown in Fig. 3.4. Each peak corresponds to one beam bunch. A prompt peak consists of the true and accidental
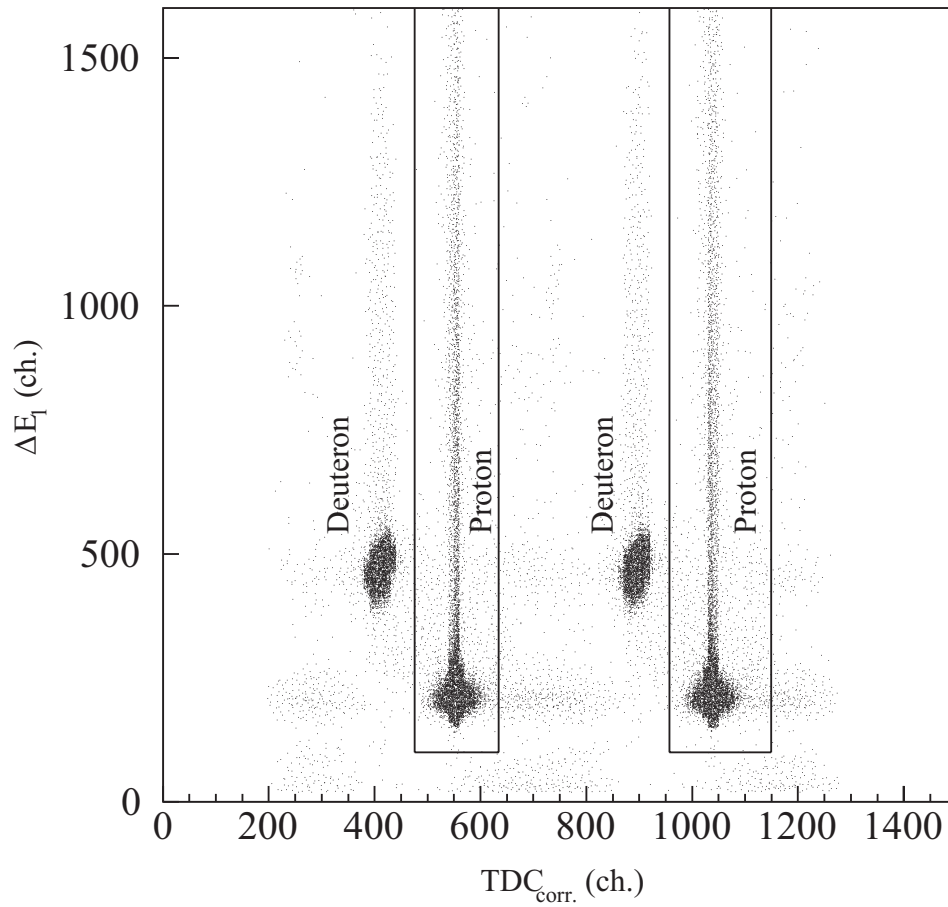
Figure 3.3: Two-dimensional scatter plot of the corrected TDC and ΔE_1 of the GR. The events enclosed by the solid lines are recognized as the proton events.

coincidence events, while the other peaks consist only of the accidental coincidence events. Assuming the beam has no micro-structures, that is, the same number of protons are included in all beam bunches, the yield of true coincidence events can be extracted by subtracting the events of one of the accidental bunch from those of the true bunch.

3.4   Track reconstruction of scattered particles

3.4.1   Multi-wire drift chambers

The trajectories of charged particles entering the focal planes of both spectrometers were determined with the GR and LAS-MWDCs. As shown in Fig. 3.5, the position p of an incident charged particle at an anode plane of the MWDC is determined from the drift lengths d_{i-1}, d_i of at least more than two wires in the same cluster. A cluster means that it has at least two adjacent hit wires. Since the X- and γ-rays mostly hit one wire only, background events by photons can be almost excluded. When $|d_i|$ is the

x 10^2
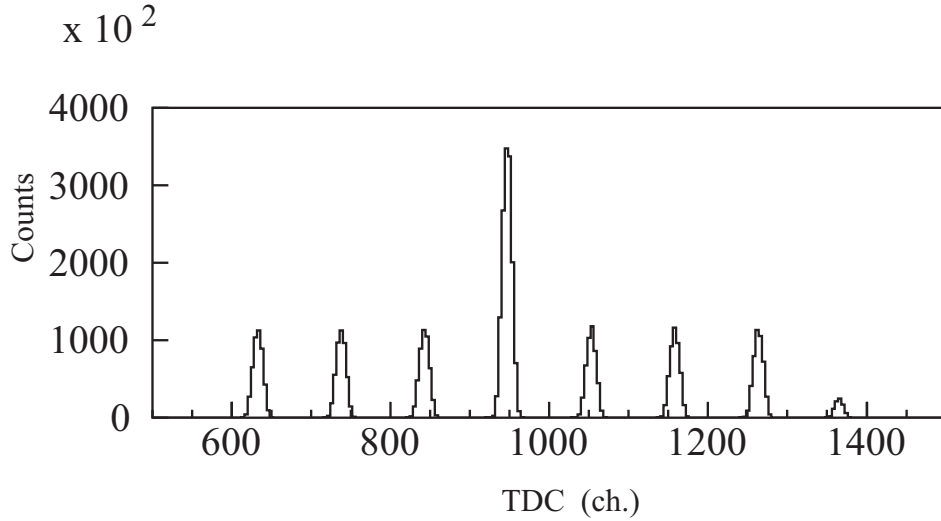
Figure 3.4: TDC spectrum for the time difference between the GR and LAS trigger signals in a measurement of the ^{40}Ca$(p, 2p)$ reaction.
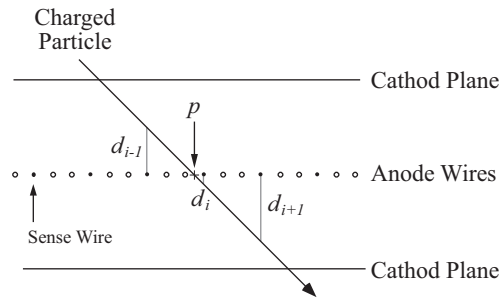
Figure 3.5: Position in a plane of MWDC.

minimum drift length in a cluster with three hit wires, the position p is simply calculated as

$$p = p_i + l_{WS} \frac{d_{i-1} + d_{i+1}}{d_{i-1} - d_{i+1}}, \qquad (d_{i-1} > 0, \quad d_{i+1} < 0) \qquad (3.6)$$

where p_i is the position of i-th wire, l_{WS} is the sense wire spacing, and a negative value is taken for d_{i+1} because electrons moving to $(i - 1)$-th wire and $(i + 1)$-th wire drift in the opposite direction. In the standard setting of both the GR and LAS-MWDCs, particles with correct trajectories usually hit more than three sense wires. The incident angle (θ) are also roughly estimated by $\tan \theta = (d_{i-1} - d_{i+1})/2l_{WS}$ with the angular resolution of about $2°$. The drift velocity is almost constant but it considerably deviates near the sense wires owing to the steep gradient of the electric field. Since the TDC value only gives the drift time of each wire, one must convert this to the drift length. The so-called $x - t$ calibration was made for each wire plane using the real data taken in the present measurements. Typical drift velocity of the uniform region is about 48 μm/ns.
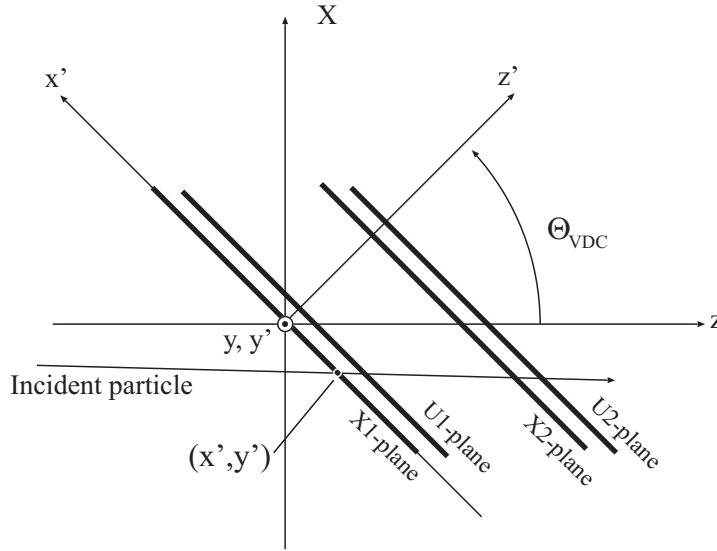
Figure 3.6: Coordinate systems for the ray-tracing with two MWDCs.

The residual distribution defined as

$$Residual = \frac{d_{i-1} + d_{i+1}}{2} - d_i \tag{3.7}$$

was used for the estimation of the resolution, and for all planes of the GR and LAS- MWDCs, the resolutions were less than 400 μm (FWHM). The position resolution δp depends on the incident angle and is mostly better than the residual resolution because the intrinsic resolution δd_i of each wire is $\sqrt{6}/3$ of the residual distribution, which is deduced from Eq. (3.7).

3.4.2 Trajectory of a charged particle

Two sets of X and U positions of anode planes can completely determine the three dimensional trajectory of the charged particle. The wire configurations of the X-planes and U-planes of the GR and LAS-MWDCs are shown in Figs. 2.7 and 2.9.

We define two coordinate systems: the central-ray coordinate in which the z-axis is the momentum direction of the central ray and the focal-plane coordinate in which z'-axis is perpendicular to the anode planes of the MWDCs, as shown in Fig. 3.6. The $z - x$ and $z' - x'$ planes are the median plane of the spectrometer. In both coordinate systems, the center of the X1-plane is taken as the origin.

In the focal-plane coordinate system, the horizontal and vertical positions (x',y') and angles $(\theta'_x = \frac{dx'}{dz'}, \theta'_y = \frac{dy'}{dz'})$ of an incident particle are calculated from p_{x1}, p_{u1}, p_{x2}, and p_{u2}, that are obtained using

Eq. (3.6).

$$\tan \theta'_x = \frac{p_{x2} - p_{x1}}{L_{DC}}, \tag{3.8}$$

$$\tan \theta'_u = \frac{p_{u2} - p_{u1}}{L_{DC}}, \tag{3.9}$$

$$\tan \theta'_y = \frac{\tan \theta'_x}{\tan \psi} - \frac{\tan \theta'_u}{\tan \psi} \tag{3.10}$$

$$x'_0 = p_{x1} \tag{3.11}$$

$$u_0 = p_{u1} - z'_{u1} \cdot \tan \theta'_u \tag{3.12}$$

$$y'_0 = \frac{x'_0}{\tan \psi} - \frac{u'_0}{\tan \psi} \tag{3.13}$$

where $L_{DC} = z'_{x2} - z'_{x1} = z'_{u2} - z'_{u1}$ is the distance of two MWDCs, ψ is the tilting angle of U-planes, and x'_0, y'_0 are the horizontal and vertical positions at the z'_0 plane. L_{DC} was 250 mm for the GR and 164 mm for the LAS. When the position resolution δp is 300 μm and the multiple scattering effect is neglected, the horizontal angular resolution is given as $(0.3 \sqrt{2}/250) \cdot \cos^2 \theta_{GR} \sim 0.85$ mrad for the GR ($\theta_{GR} \sim 45°$) and $(0.3 \sqrt{2}/164) \cdot \cos^2 \theta_{LAS} \sim 0.89$ mrad for the LAS ($\theta_{LAS} \sim 54°$) at FWHM, respectively. The vertical position and angular resolutions are about two times worse than those in the horizontal direction. The position resolution of 300 μm corresponds to about 10 keV for the GR and 10–20 keV for the LAS depending on the magnetic field, and they are smaller than the energy spread of the beam (~ 200 keV) in the present experiments.

In the central-ray coordinate, the horizontal and vertical angles are converted as

$$\theta_x = \theta'_x - \Theta_{VDC} \tag{3.14}$$

$$\tan \theta_y = \tan \theta'_x \cos \Theta_{VDC} \tag{3.15}$$

where Θ_{VDC} is the tilting angle of the MWDC for the GR (45°) or LAS (54°). Using the ion-optical matrix, one can trace these angles back to the scattering angles on the target. The focal plane of the GR almost agreed with the X-plane of MWDC1, and small aberrations were empirically corrected by looking at some two dimensional plots like an $x - \theta$ correlation spectrum. In the case of the LAS, the momentum deviation and scattering angle relative to the central ray was obtained from the trajectory at the focal plane by calculating the 4th-order matrix.

3.4.3 Efficiency of the MWDC

Efficiency of the MWDC was estimated by using $(p, 2p)$ events that a proton is detected with both of the GR and LAS. Estimation of efficiency of the MWDC needs events that a proton surely goes through the MWDC. $(p, 2p)$ events were identified by the following condition in case of the estimation of tracking efficiency of the GR-MWDCs,

I True coincidence between the GR and LAS (TDC between the GR and LAS)

II Identification of a proton for the LAS (ΔE and TOF)

III Success in a track reconstruction with the LAS-MWDCs

IV Identification of a proton for the GR (ΔE and TOF)

　　TOF is raw TDC data which is not corrected by information from the GR-MWDCs.

V Central region of the GR-MWDC

　　Position information obtained by a trigger scintillation counter was used.

　　We used the events that satisfy all the conditions I–V as a sample. For this sample, the number of the events that a track reconstruction was succeeded with the GR-MWDCs was counted; the efficiency was evaluated as the ratio of this number to the number of the sample. The efficiency of the GR-MWDCs was about 95%. The efficiency of the LAS-MWDC was estimated in the same way by replacing a role of the GR and LAS, and was 80–85%.

3.5　Multi-wire proportional chambers

Each MWPC at the entrance of the spectrometer was used to determine the scattering angle of the charged particle that comes to the focal plane. The LeCroy PCOS III system provides hit-wire information by the address of the cluster centroid and the width of the cluster. The cluster centroid with the odd hit wires is given as the wire position at the center of the hit wires, and that with the even hit wires is given as the position between two wires with a half bit address. The address of the cluster centroid is obtained in the accuracy of half pitch of the sense wire, that is, it is determined in the width of 1.01 mm ~ ±0.505 mm. The scattering angle of the particle was determined from the horizontal and vertical positions at the MWPC, assuming that the particle comes from the center of the target. The events with only one hit wire in a cluster was predominant in the measurement. In the present analysis, each anode plane was required to have only one cluster to determine the position of charged particle in the anode plane. When the angular resolution is estimated with the wire spacing of 2.02 mm, it is approximately

$$\sqrt{\left(\frac{2.02}{550}\right)^2 + \left(\frac{1}{550}\right)^2} \sim 0.22° \sim \pm 0.11°, \tag{3.16}$$

where the source width is assumed to be 1 mm in diameter and 550 mm is a approximate distance from the center of the scattering chamber to an anode plane.

　　For an estimation of the efficiency of the MWPC, we used the events that a track reconstruction with the MWDC succeeds for a proton at the focal plane. For this sample, the number of the events that a scattering angle was obtained was counted; the efficiency was evaluated as the ratio of this number to the number of the sample. The efficiency of the GR-MWPC was about 90% and that of the LAS-MWPC

was about 40–60%. The multi-cluster events decreased the efficiency of the LAS-MWPC because the LAS-MWPC has a large active area.

3.6   Solid angles

The horizontal scattering angle obtained with the MWDCs at the focal plane was used for particles coming to the GR, whereas, the horizontal scattering angle obtained with the MWPC at the entrance of the LAS was used for particles coming to the LAS because the resolution of the horizontal stattering angle obtained with the MWDCs at the LAS was worse than that with the MWPC owing to the multiple scattering. The vertical scattering angles obtained with the MWPCs were used for particles coming to the GR and LAS.

Figure 3.7 shows the two dimensional scatter plots of the horizontal (dx/dz) and vertical (dy/dz) scattering angles for protons analyzed with the GR and LAS.

The solid angle for the GR was determined by the lead collimator as 2.4 msr. Although the lead collimator was installed at the entrance of the LAS to determine the solid angle in a rectangle shape, the scattering angle for the LAS shown in Fig. 3.7 (b) doesn't show a rectangle but a hexagonal shape. The chipped corners in Fig. 3.7 (b) indicates that a part of protons which pass through the collimator stopped in the LAS. From the shape of the corners, the vacuum chamber in the quadrupole magnet probably reduced the acceptance. The solid angle for the LAS eliminated the chipped corners was estimated as 19.1 msr, which is a little smaller than 20.0 msr determined by the lead collimator.

When the LAS was set at 56.41°, pp scattering event also measured at large scattering angle part in the solid angle for the LAS. As the cross section for pp scattering is much larger than $(p, 2p)$ reaction, just a tiny part of the protons from pp scattering that lost its energy in the spectrometer possibly overlap the spectrum for the $(p, 2p)$ reaction. Therefore, only at this LAS angle setting (set1a–c), the part of the solid angle that is larger than 58.41° for the horizontal scattering angle was eliminated, and its solid angle 16.4 msr was used.

3.7   Normalization due to the trigger efficiency of the scintillation detectors

For a charged particle, a passage through the two plastic scintillation counters and an aluminum plate, which is placed between the scintillators, provides a trigger signal at each focal plane. The detection efficiency of the scintillation counter system for the GR was previously measured with a proton beam at 300 MeV changing the thickness of the aluminum plate, and the measured results show that the efficiency decreases as the thickness of the aluminum plate increases [66]. The inefficiency must be proportional to the total reaction cross section between proton and materials. The proton-^{27}Al total reaction cross section is almost constant within a 10% fluctuation for the proton energy of below 400 MeV [67].
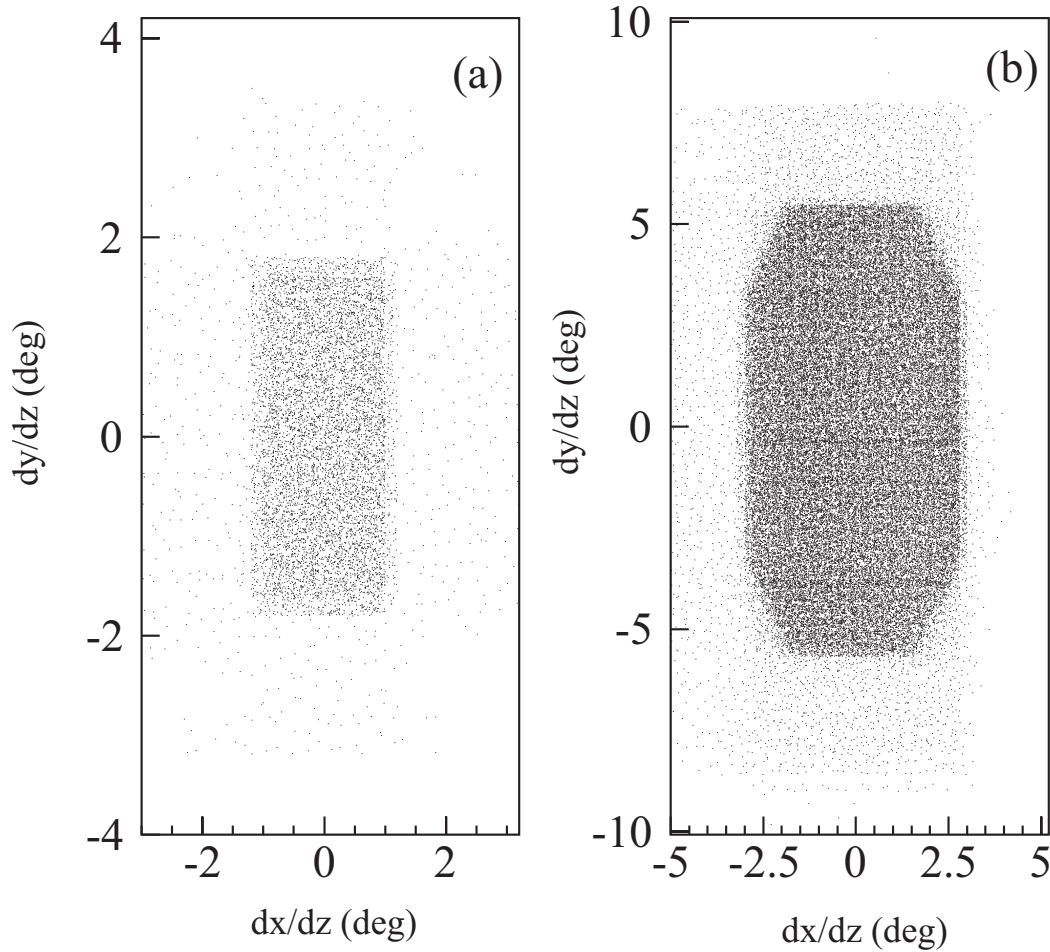
Figure 3.7: Two dimensional scatter plot of the horizontal and vertical scattering angles of protons analyzed with the GR (a) and LAS (b).

Therefore, the proton-energy dependence of the inefficiency was considered to be constant in the energy region of the present $(p, 2p)$ measurement. The inefficiency of the detection for the GR system, which used the aluminum plates with a thickness of 10 mm, was estimated as $\bar{\epsilon}_{GR} = 2.2 \pm 0.2\%$ including the uncertainty of 10% from the energy dependence of the total reaction cross section. The inefficiency of the scintillator-detection system for the LAS, which used the aluminum plates with a thickness of 3 mm, was estimated as $\bar{\epsilon}_{LAS} = 1.4 \pm 0.1\%$ by interpolation from the measurement results for the GR. Combined both the inefficiencies, the detection efficiency by the scintillation detectors for the $(p, 2p)$ measurement was estimated by

$$\epsilon_{GR \times LAS} = (1 - \bar{\epsilon}_{GR}) \times (1 - \bar{\epsilon}_{LAS}) = 96.4 \pm 0.3\,\%. \tag{3.17}$$

This efficiency is due to only the scintillation detectors, which provide a trigger for DAQ system, but it doesn't include the wire-counter efficiencies. The correction using this efficiency was applied on the yield for the $(p, 2p)$ measurement.

3.8   Separation energy of ^{40}Ca$(p, 2p)^{39}$K reaction

In each of the spectrometers, the horizontal position at the focal plane corresponds to the momentum deviation from the central momentum in the spectrometer owing to the ion-optics property. The momentum of the particle at the focal plane was obtained from the horizontal position and Bρ value for the central ray of the spectrometer. The energy loss for protons in the air between the scattering chamber and the spectrometer and in the MWPC was corrected using Bethe-Bloch formula. The momentum of the residual nucleus was calculated using the momentum conservation law. The separation energy was obtained via Eq. (2.1). The two dimensional scatter plot of the energies of coincidence two protons measured with the GR and LAS and the separation-energy spectrum for the ^{40}Ca$(p, 2p)$ reaction at $T_0 = 392$ MeV are shown in Fig. 3.8(a) and (b) The thick loci that correspond to the transitions to the ground and lower excited states in ^{39}K can be seen in Fig. 3.8(a). Several discrete states, such as the ground state $(3/2^+)$ and the first excited state $(2.52$ MeV $1/2^+)$, are observed in Fig. 3.8(b).

3.9   Cross sections and analyzing powers

The differential cross section of the $(p, 2p)$ reaction in the laboratory system is written as

$$\frac{d^4\sigma}{d\Omega_1 d\Omega_2 dT_1 dT_2} = \frac{Y}{QA\epsilon\eta\Delta\Omega_1\Delta\Omega_2\Delta T_1\Delta T_2}, \tag{3.18}$$

where Y is the $(p, 2p)$ coincidence yield, Q is the total number of protons in the incident beam, A is the number of target particles per unit area, ϵ is the detection efficiency, and η is the live time ratio of the data acquisition system. $\Delta\Omega_{1,2}$ are the solid angles of the spectrometers of the GR (1) and LAS (2), and ΔT_1 and ΔT_2 are the energy range of the proton detected with the GR and LAS. $\Delta T_1 = 8$ MeV and $\Delta T_2 = 0.1$ MeV were used for the separation-energy spectra in Chap. 5.

For a certain separation energy E_{sep} of the $(p, 2p)$ reaction, the differential cross section of

$$\frac{d^3\sigma}{d\Omega_1 d\Omega_2 dT_1} = \frac{Y}{QA\epsilon\eta\Delta\Omega_1\Delta\Omega_2\Delta T_1}, \tag{3.19}$$

is used to show its recoil momentum distribution. $\Delta T_1 = 4$ MeV was used for the recoil momentum distributions.

For polarized proton beam, the yields for spin-up ($\uparrow$) and spin-down ($\downarrow$) modes are described as

$$Y^\uparrow = \frac{d^3\sigma}{d\Omega_1 d\Omega_2 dT_1}(1 + p^\uparrow)Q^\uparrow A\epsilon^\uparrow\eta^\uparrow\Delta\Omega_1\Delta\Omega_2\Delta T_1, \tag{3.20}$$

$$Y^\downarrow = \frac{d^3\sigma}{d\Omega_1 d\Omega_2 dT_1}(1 - p^\downarrow)Q^\downarrow A\epsilon^\downarrow\eta^\downarrow\Delta\Omega_1\Delta\Omega_2\Delta T_1. \tag{3.21}$$
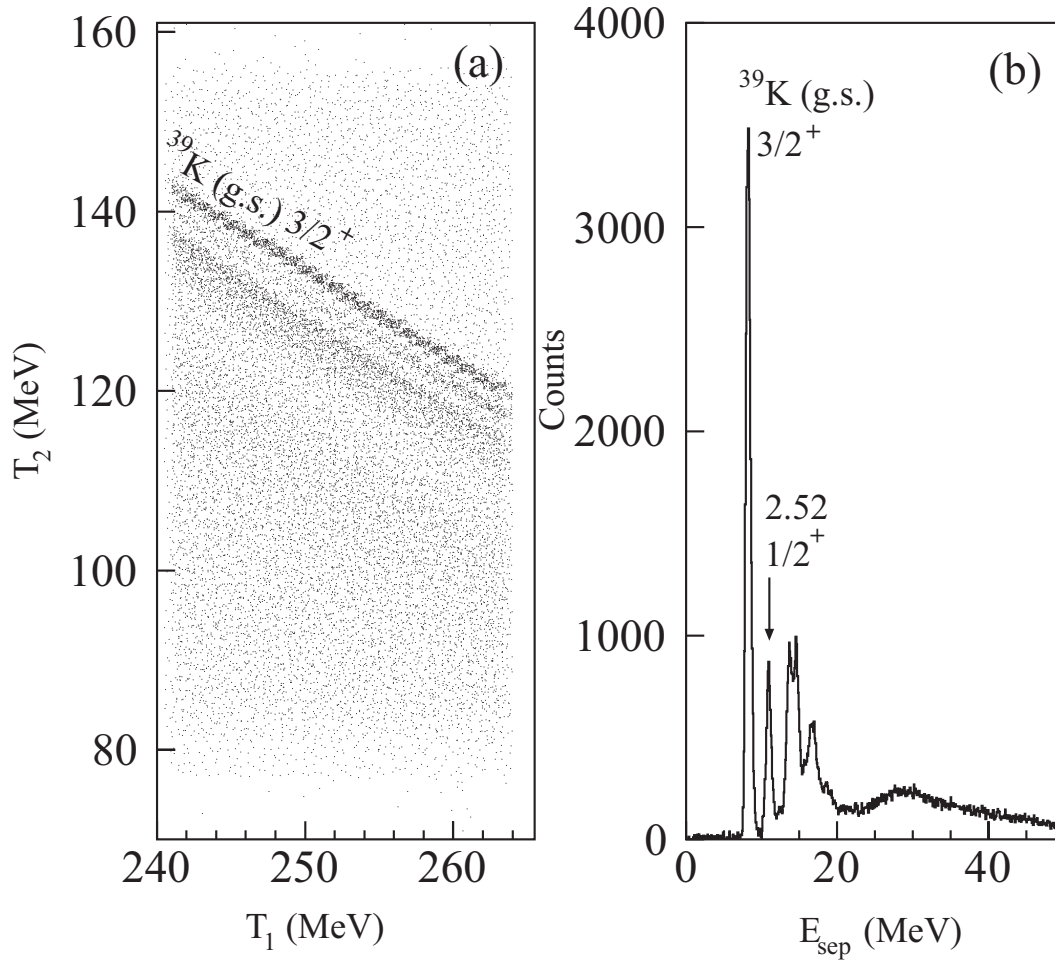
Figure 3.8: (a): Two dimensional scatter plot of the energies of coincidence two protons measured with the GR and LAS in the ^{40}Ca$(p, 2p)$ reaction at $T_0 = 392$ MeV. (b): Separation-energy spectrum for the ^{40}Ca$(p, 2p)$ reaction.

The superscripts of ↑ and ↓ represent the quantities in spin-up (↑) and spin-down (↓) modes. The differential cross section and the analyzing power are written as

$$\frac{d\sigma}{d\Omega_1 d\Omega_2 dT_1} = \frac{p^\downarrow N^\uparrow + p^\uparrow N^\downarrow}{p^\uparrow + p^\downarrow} \frac{1}{A \Delta\Omega_1 \Delta\Omega_2 \Delta T_1}, \tag{3.22}$$

$$A_y = \frac{N^\uparrow - N^\downarrow}{p^\downarrow N^\uparrow + p^\uparrow N^\downarrow}, \tag{3.23}$$

where

$$N^\uparrow = \frac{Y^\uparrow}{Q^\uparrow \epsilon^\uparrow \eta^\uparrow}, \qquad N^\downarrow = \frac{Y^\downarrow}{Q^\downarrow \epsilon^\downarrow \eta^\downarrow}. \tag{3.24}$$

3.10 pp-scattering

To examine the absolute value of the cross section measured with the system that consists of the WS beamline, the GR and LAS spectrometers, and the focal plane detectors, pp scattering was measured at $25.5°$ for the GR and at $60.0°$ for the LAS with 9.2 mg/cm^2 polyethylene targets. The uncertainties of the angle settings for the GR and LAS are quite smaller than $0.1°$. Since the solid angle and the momentum acceptance of the LAS are larger than those of the GR, the acceptance of pp scattering measurement was determined by the GR.

The separation energy defined with only the energies of two scattered protons in the final state as $E'_{\text{sep}} = T_0 - T_1 - T_2$ was used to identify pp scattering event. E'_{sep} must be 0 in case of pp scattering. The analyzing power was obtained in the same way as that for the $(p, 2p)$ reaction.

The measured cross section of pp scattering was 15.52 ± 0.28 mb/sr, which differs by 2.3% from the SAID [68, 69] calculation value of 15.89 mb/sr. The value of 15.89 mb/sr was evaluated by folding over the solid-angle acceptance, as was same as the following calculation for the analyzing power. The difference of 2.3% between the measured cross section and the SAID calculation value is as small as the uncertainty of the thickness of polyethylene target (2%). The measured analyzing power A_y was 0.336 ± 0.005. The difference between the measured value and the SAID calculation value of $A_y = 0.365$ is 0.029 and it is small enough for the following discussion.

Chapter 4

Analysis

We utilized the spectrum at the set1 for the analysis of the discrete peaks, and those at the set2–5 for the analysis of the broad spectrum region. To deduce spectroscopic factors and to compare the recoil-momentum distribution of the cross section and the analyzing power with theoretical calculation, DWIA calculation was carried out.

4.1 Distorted wave impulse approximation calculation

The cross sections and the analyzing powers were calculated for the $^{40}\text{Ca}(p, 2p)^{39}\text{K}$ reaction using a DWIA code THREEDEE [70].

The cross section for the quasi-elastic scattering is calculated assuming that the quasi-elastic scattering is a N–N scattering process in a target nucleus. The program code THREEDEE includes spin-orbit effects in distorting potentials and makes the factorization approximation in separating the matrix elements of the two-body transition operator outside the distorted wave integral. When we consider a quasi-free reaction $A(a, cd)B$ where $A = B + b$, the cross section can be written as [70]

$$
\frac{d^3\sigma}{d\Omega_c \Omega_d dE_c}
$$
$$
= \frac{2\pi}{\hbar v} \omega_B C^2 S \sum_{\substack{\rho_a \rho_c' \rho_d'' \\ JM}} \frac{1}{(2J+1)(2S_a+1)} \left| \sum_{\substack{\sigma_a \sigma_c' \sigma_d'' \\ \Lambda \sigma_b}} (2L+1)^{1/2} \left(L\Lambda S_b \sigma_b | JM \right) T^{L\Lambda}_{\sigma_a \sigma_c' \sigma_d''} \langle \sigma_c' \sigma_d'' | t | \sigma_a \sigma_b \rangle_{\rho_a \rho_c' \rho_d''} \right|^2,
$$

(4.1)

where $S_a = S_b = \frac{1}{2}$ are the spins of the particles a and b, v is the incident velocity, ω_B is the phase space factor, and C^2S is the spectroscopic factor. J, M are the total angular momentum quantum numbers of particle b. The quantities L and Λ are the orbital angular momentum carried by b and its projection. The two-body transition operator t is separated outside the distorted wave integral by the factorization approximation. The spin matrices are given in the different coordinates where the directions of propagation of particles a, c, and d are $\hat{z}$, $\hat{z}'$, and $\hat{z}''$ axes. Spin projections are denoted as ρ_i. The quantity

45

Table 4.1: Bound-state parameters of the Woods-Saxon potential for ^{40}Ca nucleus.

Nucleus	Orbital	r_0 [fm]	a [fm]	$V_{\rm so}$ [MeV]
Elton and Swift [73]	$2s$	1.30	0.60	
	$1_{7/2}$	1.30	0.60	8.3
	$1d$	1.30	0.60	12
	$1p$	1.30	0.60	30
	$1s$	1.30	0.60	
Kramer *et al.* [74]	$1d_{3/2}$	1.295(47)	0.65	7.15 [a]
	$2s_{1/2}$	1.276(59)	0.65	
	$1f_{7/2}$	1.348(67)	0.65	8.45 [b]

[a]This $V_{\rm so}$ value is calculated with Thomas spin-orbit parameter $\lambda = 25$ and depth of the potential-well $V_0 = 51.6$ MeV in Ref. [74].

[b]This $V_{\rm so}$ value is calculated with Thomas spin-orbit parameter $\lambda = 25$ and depth of the potential-well $V_0 = 61.0$ MeV in Ref. [74].

$T^{L\Lambda}$ is defined by

$$T^{L\Lambda}_{\substack{\sigma_a\sigma'_c\sigma''_d \\ \rho_a\rho'_c\rho''_d}} = (2+1)^{-1/2} \int \chi^{(-)}_{\sigma'_c\rho'_c}{}^* \left(\vec{r}'\right) \chi^{(-)}_{\sigma''_d\rho''_d}{}^* \left(\vec{r}''\right) \phi_{L\Lambda}\left(\vec{r}\right) \chi^{(+)}_{\sigma_a\rho_a}\left(\gamma\vec{r}\right) d\vec{r}, \qquad (4.2)$$

where $\gamma = B/A$, the $\chi^{\pm}$ are distorted waves which also convert the spin states from σ to ρ, and $\phi_{L\Lambda}$ is the spatial part of the bound state wave function of particle b. The inclusion of spin-orbit distortion increases the complexity of the description of the distorted waves. For an incident polarized beam, we can omit the average on the spin state of the particle a in the description of the cross section in Eq. (4.1).

In the present calculations, the NN scattering t matrix with the on-shell amplitude was approximately employed in the final energy prescription, although the two-body t matrix used for the $(p, 2p)$ reaction should be evaluated in the nuclear medium including off-shell properties. The t matrix was taken from the solution of the phase shift analysis by Arndt *et al* [71].

The distorted waves were calculated using the Schrödinger equivalent potential from the Dirac global optical model parameters obtained by Cooper *et al.* [72]. The EDAD-1 potential parameter set was used in the calculations. The wave functions for the bound nucleons were calculated by adjusting the depth of the Woods-Saxon potential to reproduce the empirical separation energies. The parameters provided by Elton and Swift [73] were employed for the Woods-Saxon potential and a Coulomb potential for a uniformly charged sphere with a radius of $1.25\, M^{1/3}$ fm, where M is a mass number of the nucleus. The parameters are listed in Table 4.1.

Since the radius of the bound-state potential is critical for calculating the cross section, Elton's parameter choice was confirmed by evaluating the root-mean-square radius (RMSR) of the potential expected from the point nucleon distribution in the nucleus as follows.

The mean-square radius (MSR) of the charge distribution of the nucleus $\langle r_{ch}^2 \rangle$ can be written as

$$\langle r_{ch}^2 \rangle = \langle r_p^2 \rangle + \langle r_{ch}^2 \rangle_p + \frac{N}{Z} \langle r_{ch}^2 \rangle_n \tag{4.3}$$

where $\langle r_p^2 \rangle$, $\langle r_{ch}^2 \rangle_p$, and $\langle r_{ch}^2 \rangle_n$ denote the MSRs of the point proton distribution in the nucleus, the charge distribution of the proton, and the charge distribution of the neutron, respectively. Z and N indicate the number of protons and neutrons in the nucleus. The RMSRs of the charge distribution of the proton and of the ^{40}Ca nucleus are $\langle r_{ch}^2 \rangle_p^{1/2} = 0.8791$ fm [75] and $\langle r_{ch}^2 \rangle_{Ca}^{1/2} = 3.4764$ fm [75], respectively. The MSR of the neutron charge distribution $\langle r_{ch}^2 \rangle_n$ is -0.1149 fm^2 [75]. Note that the negative value of $\langle r_{ch}^2 \rangle_n$ comes from the negative charge distribution in the larger-radius region of the neutron. From Eq. (4.3), the RMSR of the proton distribution in the ^{40}Ca nucleus is estimated as

$$\begin{aligned} \langle r_p^2 \rangle^{1/2} &= \left(\langle r_{ch}^2 \rangle_{Ca} - \langle r_{ch}^2 \rangle_p - \frac{N}{Z} \langle r_{ch}^2 \rangle_n \right)^{1/2} \\ &= 3.38 \text{ fm}. \end{aligned} \tag{4.4}$$

The MSR of the potential in the nucleus can be considered as the sum of the MSR of the nucleon distribution in the nucleus and that of NN interaction range. Assuming the effective interaction range of $\langle r_{int}^2 \rangle = 5.78$ fm^2 calculated from the mass-number-dependent formula $\langle r_{int}^2 \rangle = (0.132 \pm 0.013)A^{2/3} + (4.24 \pm 0.24)$ fm^2 [76], we evaluated the RMSR of the ^{40}Ca potential as

$$\langle r_{pot}^2 \rangle_{Ca}^{1/2} = \left(\langle r_p^2 \rangle + \langle r_{int}^2 \rangle \right)^{1/2} = 4.15 \text{ fm}. \tag{4.5}$$

The MSR of the proton distribution is used instead of the MSR of the nucleon distribution because ^{40}Ca has the same number of protons and neutrons. It was confirmed that the RMSR of 4.14 fm for the Woods-Saxon potential with the Elton parameter is in good agreement with the estimated RMSR of 4.15 fm for the ^{40}Ca potential expected from the point nucleon distribution.

To compare the measured and calculated cross sections, the cross sections calculated with the DWIA code were averaged over the angular and momentum acceptances of the spectrometers.

4.2 Multipole decomposition analysis

Since the deep-hole states induced by nucleon knockout reactions from deeply bound orbitals stay far above the particle-decay threshold and have short lifetimes, these states have large widths and overlap each other. If we assume that the cross sections for different hole states do not coherently interfere with each other, the total cross section can be described by the superposition of the cross sections for different hole states by the $(p, 2p)$ reaction. Since the recoil-momentum distribution of the $(p, 2p)$ reaction cross section predominantly depends on L, a superposition of the cross sections for the $(p, 2p)$ reaction from different L orbitals was used for a fitting to the experimental recoil-momentum distribution data. The single-particle-hole strength for each orbital was obtained by the fitting. This technique is known as l-decomposition [77] or multipole decomposition analysis (MDA).
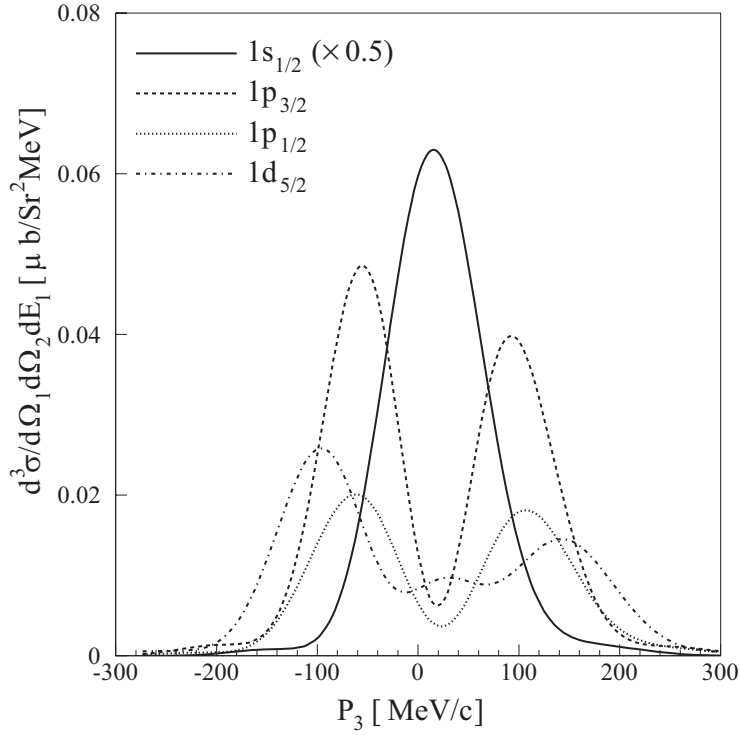
Figure 4.1: Recoil-momentum distributions of the cross sections for the $1s_{1/2}$-, $1p_{3/2}$-, $1p_{1/2}$-, and $1d_{5/2}$-hole states by DWIA calculations. They were calculated with spectroscopic factors of 1 at a separation energy 15 MeV under a certain kinematical condition.

Figure 4.1 shows recoil momentum distributions of the cross sections for some single hole states calculated by the DWIA code. The cross section shows characteristic recoil-momentum distribution depending on the angular momentum (L) of the hole state. As the angular momentum L increases, the maximum position of the cross section moves to larger recoil-momentum region. The MDA utilizes this L-dependence of the cross sections.

The momentum distribution of the cross section at a separation energy E_{sep} is written in terms of the $(p, 2p)$ cross section $\sigma_{\alpha}^{\text{DWIA}}(E_{\text{sep}}, T_1)$ for the single-particle-hole state obtained from a DWIA calculation as follows:

$$\sigma^{\text{calc}}(E_{\text{sep}}, T_1) = \sum_{\alpha} S_{\alpha}(E_{\text{sep}})\sigma_{\alpha}^{\text{DWIA}}(E_{\text{sep}}, T_1), \tag{4.6}$$

where α indicates an occupied single-particle orbital in the nucleus, for example $\alpha = 2s_{1/2}, 1d_{5/2}$, etc. $S_{\alpha}(E_{\text{sep}})$ is the hole-state strength for the orbital α. The quantity $\sigma(E_{\text{sep}}, T_1)$ denotes the triple-differential cross section,

$$\sigma(E_{\text{sep}}, T_1) = \frac{d^3\sigma}{d\Omega_1 d\Omega_2 dT_1}, \tag{4.7}$$

where Ω_1, Ω_2, and T_1 represent the solid angles of the two spectrometers and the kinetic energy of one of the scattered protons, respectively.

The χ^2 for fitting to the cross-section data is defined by:

$$\chi^2 = \chi^2_{cs} = \sum_i \left(\frac{\sigma^{\exp}(E_{\text{sep}}, T_{1i}) - \sigma^{\text{calc}}(E_{\text{sep}}, T_{1i})}{\Delta\sigma(E_{\text{sep}}, T_{1i})} \right)^2, \tag{4.8}$$

where $\sigma^{\exp}(E_{\text{sep}}, T_1)$ and $\Delta\sigma(E_{\text{sep}}, T_i)$ are the measured cross section and its uncertainty including the statistical and the systematic uncertainties. From the analysis of pp scattering in Sec. 3.10, the systematic uncertainty of 2–3% was estimated, and the 6% uncertainty arose from the thicknesses of the calcium targets. Therefore, we added these two kinds of uncertainties in quadrature and included the systematic uncertainty of 7% in the uncertainties for the fittings. The summation index i runs to the number of the data and the S_αs were searched to minimize the χ^2 at each separation energy. The uncertainties in the S_αs correspond to a change of 1 in χ^2 from the minimum value. The spectroscopic factor for the orbital α was given by summing the strengths as

$$S_\alpha = \sum_{E_{\text{sep}}} S_\alpha(E_{\text{sep}}). \tag{4.9}$$

4.3 Multipole decomposition analysis with A_y data

The cross sections of each single-particle state for spin-up and spin-down states of the proton beam with the polarization p are written by using the cross section $\sigma_\alpha^{DWIA}(E_{\text{sep}}, T_1)$ and the analyzing power $A_{y\,\alpha}^{DWIA}(E_{\text{sep}}, T_1)$ as

$$\sigma_\uparrow^{calc}(E_{\text{sep}}, T_1) = \sum_\alpha S_\alpha \sigma_\alpha^{DWIA}(E_{\text{sep}}, T_1)\left\{ 1 + p A_{y\,\alpha}^{DWIA}(E_{\text{sep}}, T_1) \right\}, \tag{4.10}$$

$$\sigma_\downarrow^{calc}(E_{\text{sep}}, T_1) = \sum_\alpha S_\alpha \sigma_\alpha^{DWIA}(E_{\text{sep}}, T_1)\left\{ 1 - p A_{y\,\alpha}^{DWIA}(E_{\text{sep}}, T_1) \right\}, \tag{4.11}$$

where the $\uparrow$ and $\downarrow$ show the spin states of the proton beam.

The analyzing power at E_{sep} is written as

$$
\begin{aligned}
& A_y^{calc}(E_{\text{sep}}, T_1) \\
&= \frac{1}{p} \frac{\sigma_\uparrow^{calc}(E_{\text{sep}}, T_1) - \sigma_\downarrow^{calc}(E_{\text{sep}}, T_1)}{\sigma_\uparrow^{calc}(E_{\text{sep}}, T_1) + \sigma_\downarrow^{calc}(E_{\text{sep}}, T_1)} \\
&= \frac{\sum_\alpha S_\alpha(E_{\text{sep}})\, \sigma_\alpha^{DWIA}(E_{\text{sep}}, T_1)\, A_{y\,\alpha}^{DWIA}(E_{\text{sep}}, T_1)}{\sum_\alpha S_\alpha(E_{\text{sep}})\, \sigma_\alpha^{DWIA}(E_{\text{sep}}, T_1)}.
\end{aligned} \tag{4.12}
$$

In the MDA with the analyzing power data, the χ^2 for the A_y data is defined as

$$\chi^2_{A_y} = \sum_i \left(\frac{A_y^{exp}(E_{\text{sep}}, T_i) - A_y^{calc}(E_{\text{sep}}, T_i)}{\Delta A_y(E_{\text{sep}}, T_i)} \right)^2, \tag{4.13}$$

where $A_y^{exp}(E_{\text{sep}}, T_1)$ and $\Delta A_y(E_{\text{sep}}, T_i)$ are a measured analyzing power and the uncertainty. In the case of MDA including the cross section and the analyzing power, $\chi^2_{A_y}$ is also included and the total χ^2 is defined as $\chi^2 = \chi^2_{cs} + \chi^2_{A_y}$.

Chapter 5

Result

5.1 Separation-energy spectra

Separation-energy spectra at the measured kinematical set1–5 are displayed in Figs. 5.1–5.5. Yields of some parts of the spectra are reduced owing to the limits of the momentum acceptance of the spectrometers. Vertical dotted lines in Fig. 5.3–5.5 show boundaries where the momentum acceptance is guaranteed. Parts of the yields at the outside of the dotted lines are lost owing to the momentum acceptance. The typical separation-energy resolution is 750 keV at full width at half maximum (FWHM).

The spectra display the cross section as a function of the separation energy and show the distribution of hole states. The transitions to the ground and lower excited states in ^{39}K are seen as the discrete peaks in Fig. 5.1 and 5.2. In Fig 5.3, a hump is seen around 30 MeV, where the hole state of the $1p$ orbital is expected from previous experiments [18, 19, 22]. Over 40 MeV, the cross section decreases as the separation energy increases, and no peak or hump cannot be seen.

In these measurements, the vertical acceptances of the spectrometers were able to be decreased in offline analysis by using the information of the installed MWPCs in front of the spectrometers. Following a previous work by Volkov *et al* [22], separation energy spectra with small vertical acceptance gates were prepared, however, any hump structure was not able to be recognized as same as the spectra without the vertical gates.

Two prominent discrete peaks at 8.3 and 10.9 MeV in the separation energy spectra were analyzed at the set1 independently because they are well isolated, and the data of the broad spectrum region at the separation energies above 12 MeV was analyzed by the MDA at the set2–5 to separate the contribution from some hole states.
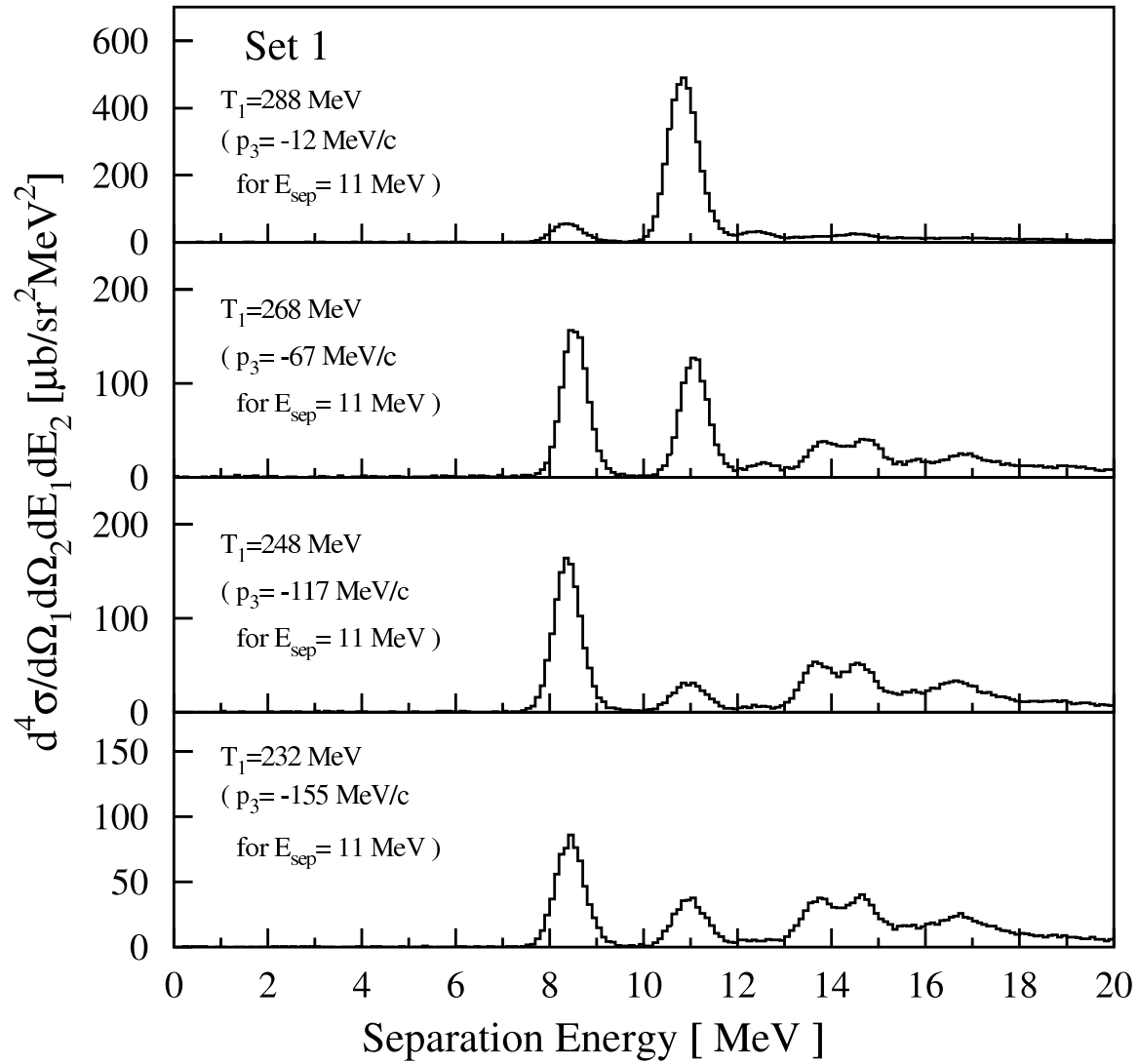
Figure 5.1: Separation-energy spectra at the measured kinematical set1 in Table 2.1.
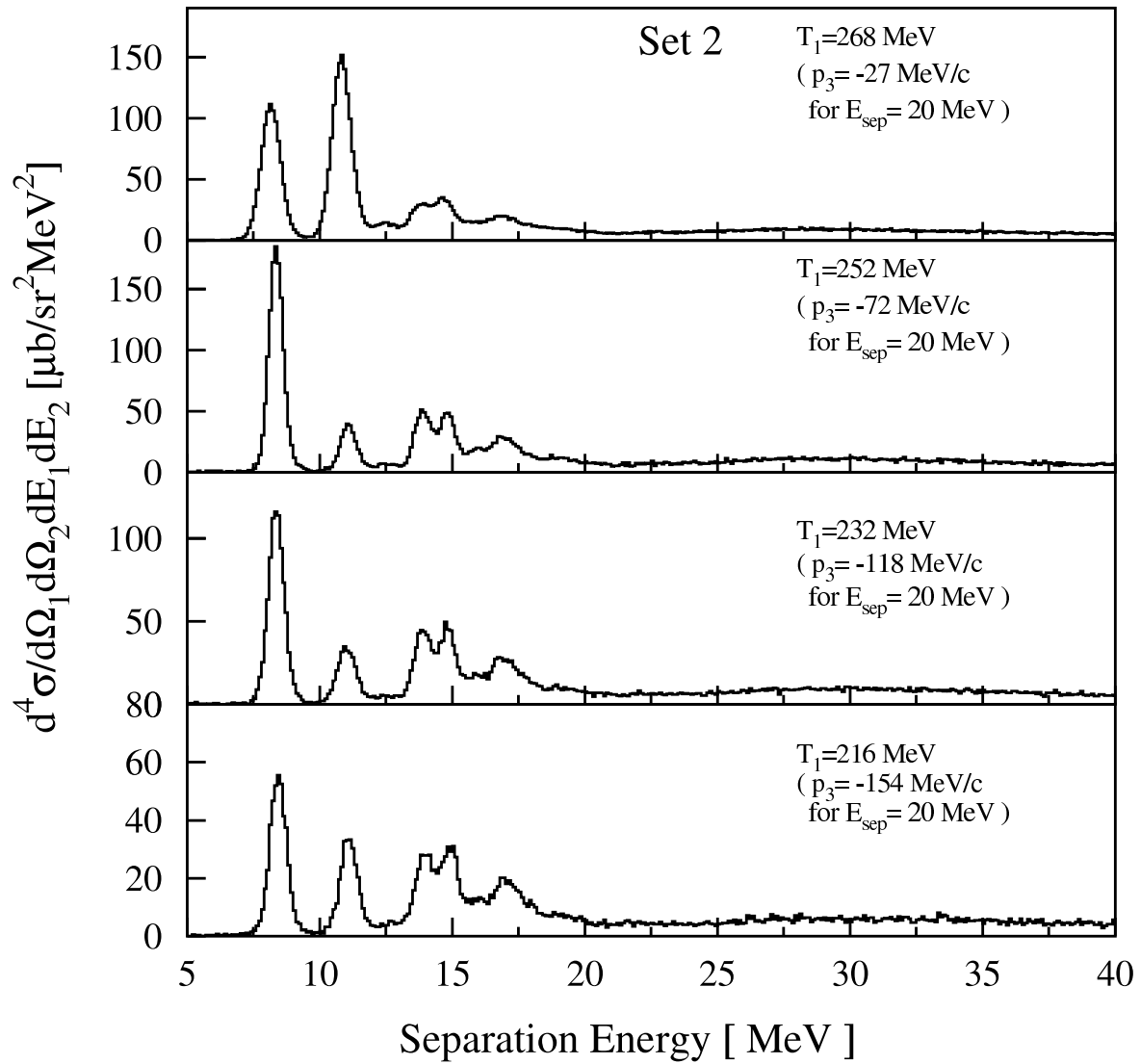
Figure 5.2: Separation-energy spectra at the measured kinematical set2 in Table 2.1.
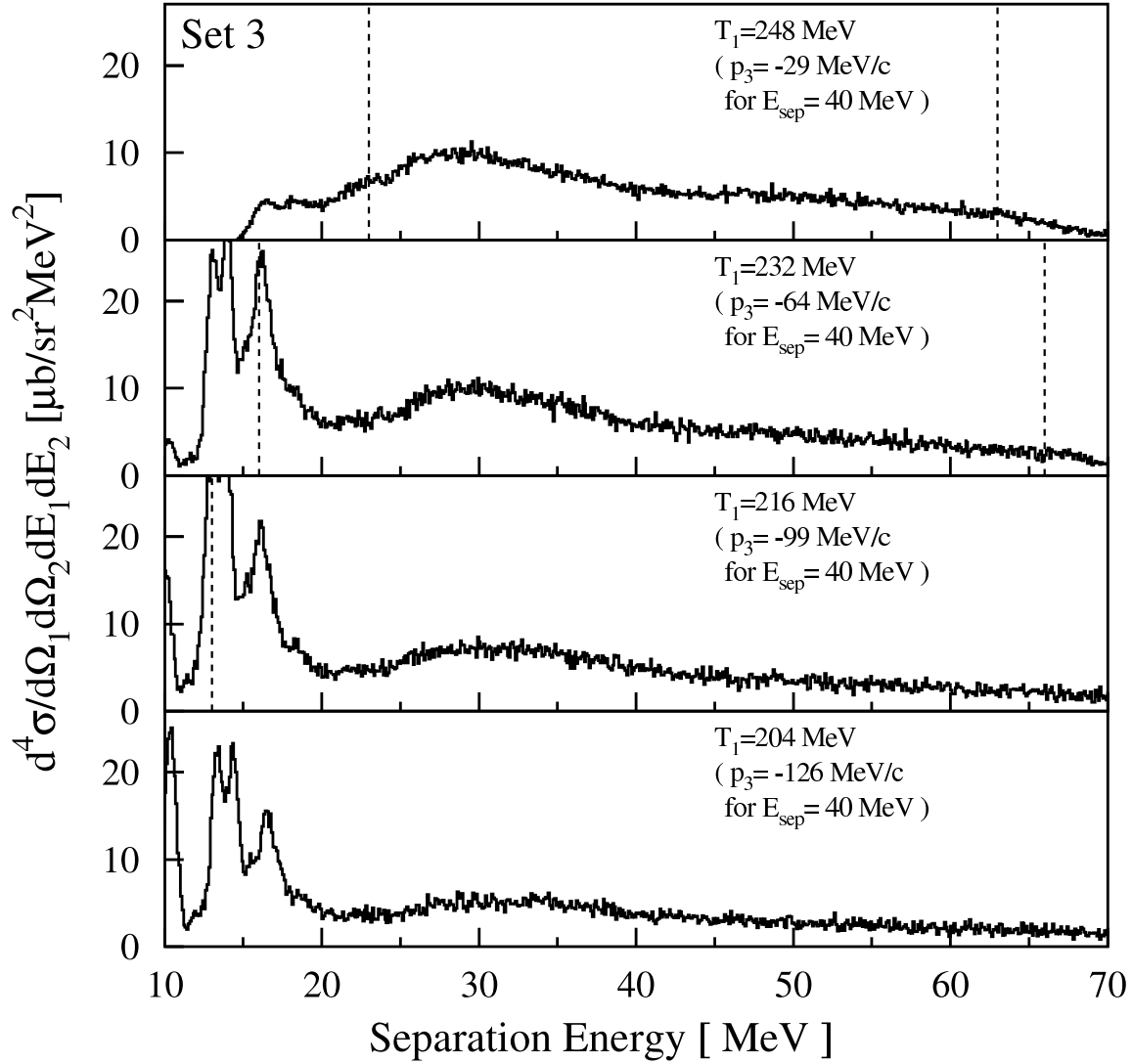
Figure 5.3: Separation-energy spectra at the measured kinematical set3 in Table 2.1. Vertical dotted lines show boundaries where the momentum acceptance is guaranteed. Yields at the outside of the vertical dotted lines decrease due to the finite momentum acceptance of the spectrometers.
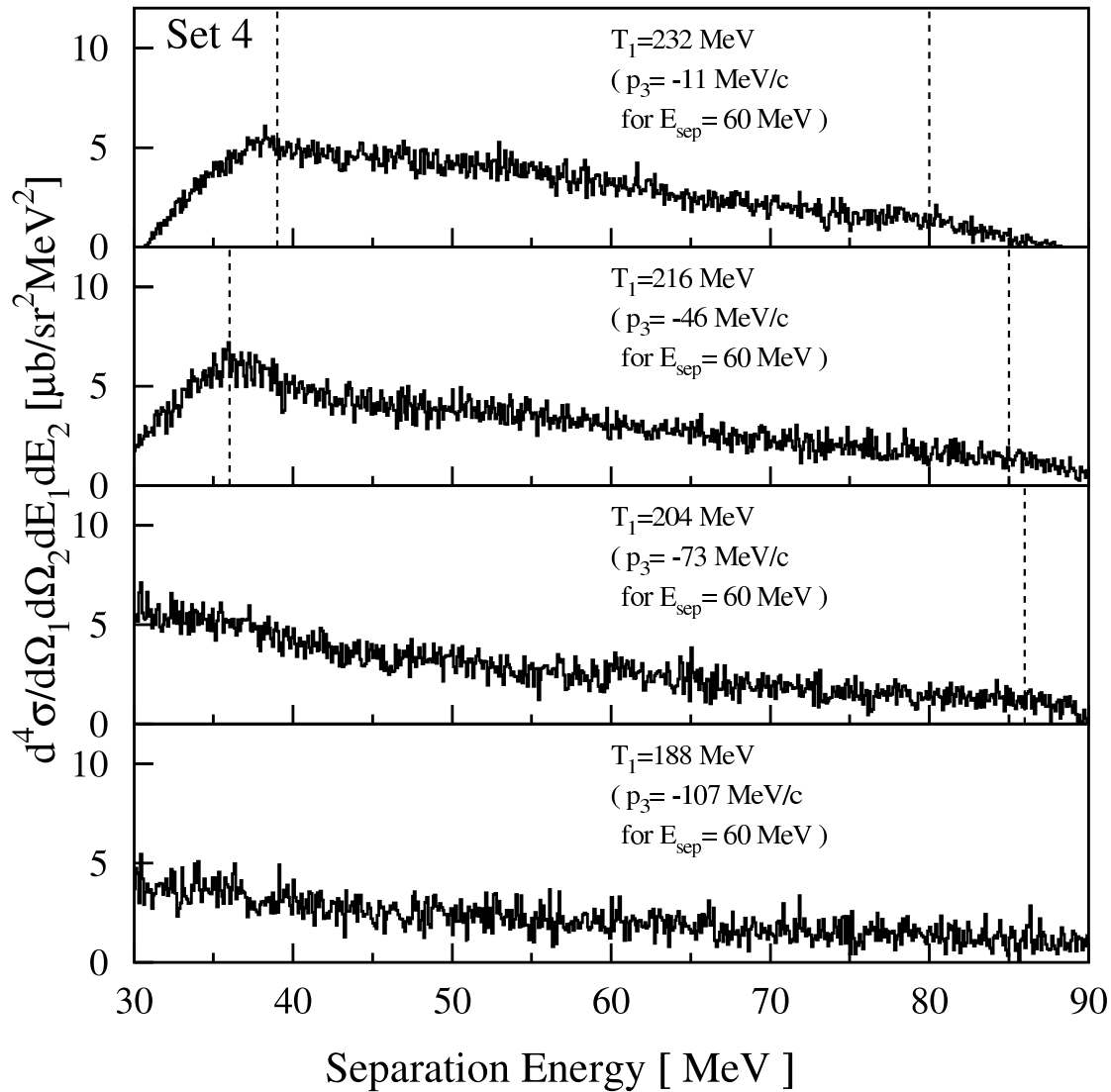
Figure 5.4: Separation-energy spectra at the measured kinematical set4 in Table 2.1. Vertical dotted lines show boundaries where the momentum acceptance is guaranteed. Yields at the outside of the vertical dotted lines decrease due to the finite momentum acceptance of the spectrometers.
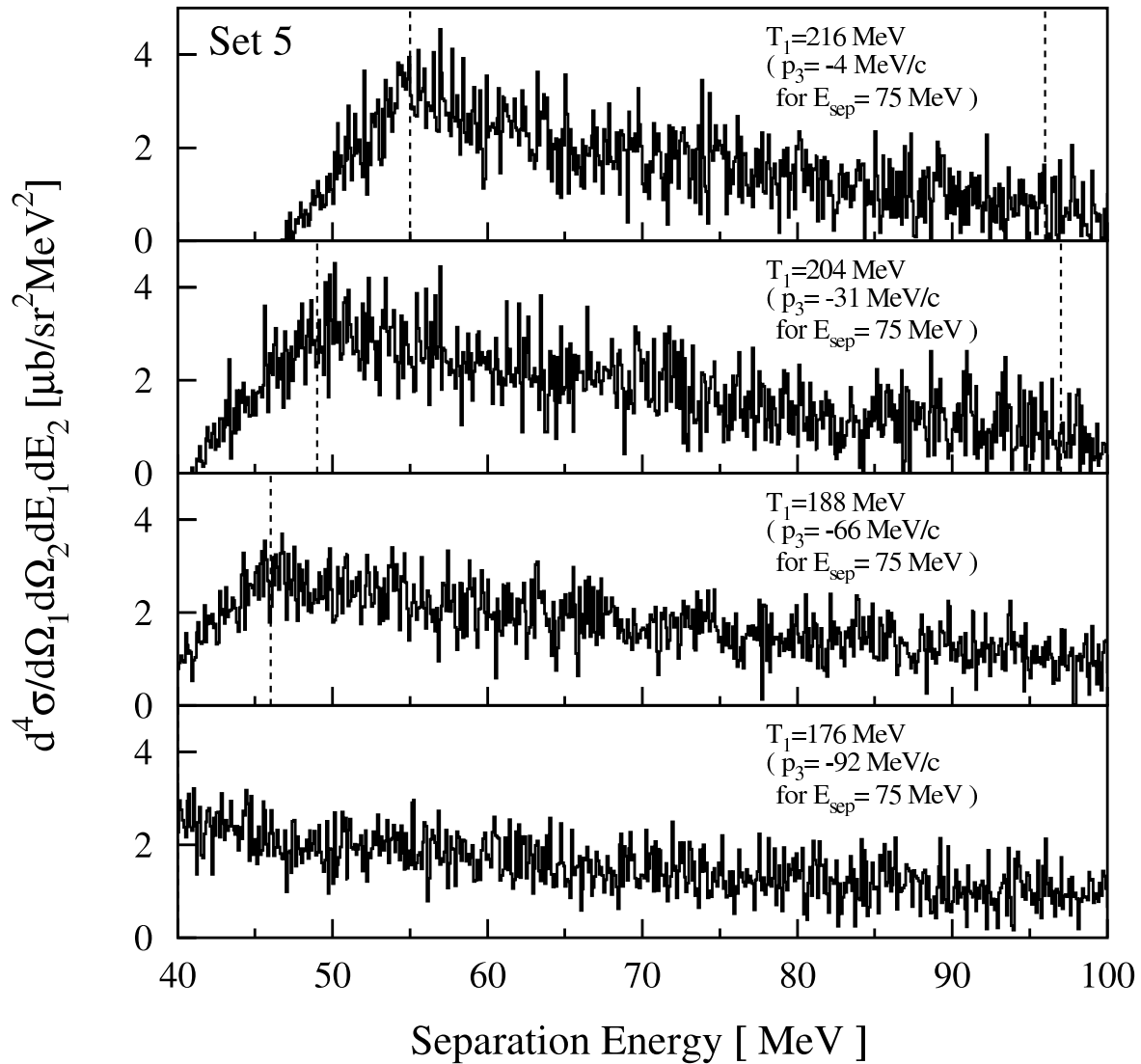
Figure 5.5: Separation-energy spectra at the measured kinematical set5 in Table 2.1. Vertical dotted lines show boundaries where the momentum acceptance is guaranteed. Yields at the outside of the vertical dotted lines decrease due to the finite momentum acceptance of the spectrometers.

5.2 Results for the discrete states

The separation-energy spectrum up to $20\,\mathrm{MeV}$ at the set1 is shown in Fig. 5.6. Two prominent peaks are observed at 8.3 and $10.9\,\mathrm{MeV}$. The recoil-momentum distributions of the cross section and the analyzing power for these peaks are displayed in Figs. 5.7 and 5.8, respectively. The error bars that represent the statistical uncertainties are smaller than the symbols.
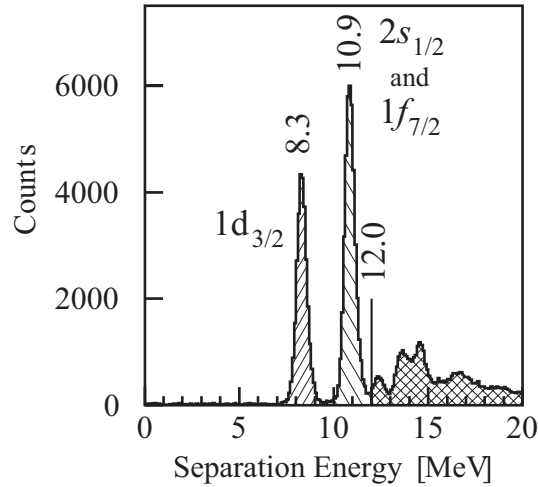
Figure 5.6: Separation-energy spectrum for the ^{40}Ca$(p, 2p)$ reaction up to $E_{\mathrm{sep}} = 20\,\mathrm{MeV}$ at the kinematical set1 (Table 2.1). Two prominent peaks are observed at $8.3\,\mathrm{MeV}$ and $10.9\,\mathrm{MeV}$. The MDA was performed at separation energies above $12\,\mathrm{MeV}$.

In Fig. 5.7, the cross section of the first hole state has a minimum near $p_3 = 0\,\mathrm{MeV}/c$ in the recoil-momentum distribution. This suggests that the peak consists of a hole state of a single-particle orbital with $L \neq 0$, as mentioned in Sec. 2.2.

In ^{40}Ca, the orbital with $L \neq 0$ near the Fermi surface is $1d$ orbital. The $1d$ orbital is split into the $j_<$ and $j_>$ orbitals by the spin-orbit interaction and the $j_>$ orbital is bound more deeply than the $j_<$ orbital. The $j_<$ orbital, that is, the $1d_{3/2}$ orbital ought to contribute a hole state of the first peak. The solid curves in Fig. 5.7 show the recoil-momentum distributions for the hole state of the $1d_{3/2}$ orbital obtained from the DWIA calculation, which are normalized to the measured cross section. The DWIA calculation reproduces the measured cross section reasonably well. The calculation roughly reproduces the dependence of the recoil momentum on the analyzing power, but the value of the analyzing power is systematically overestimated in the entire recoil-momentum range. The spectroscopic factor deduced as the normalization factor is listed in Table 5.1 and is larger than the $2J + 1$ value of 4.

In Fig. 5.8, the recoil-momentum distribution of the cross section for the peak at $10.9\,\mathrm{MeV}$ exhibits a maximum around $0\,\mathrm{MeV}/c$, which is characteristic for a hole state of a single-particle orbital with $L = 0$. Therefore, the hole state of the $2s_{1/2}$ orbital is expected to be dominant in the peak at $10.9\,\mathrm{MeV}$. Comparing with the level structure of ^{39}K [78], we see that the hole states of the $1f_{7/2}$ and $2p_{3/2}$ orbitals
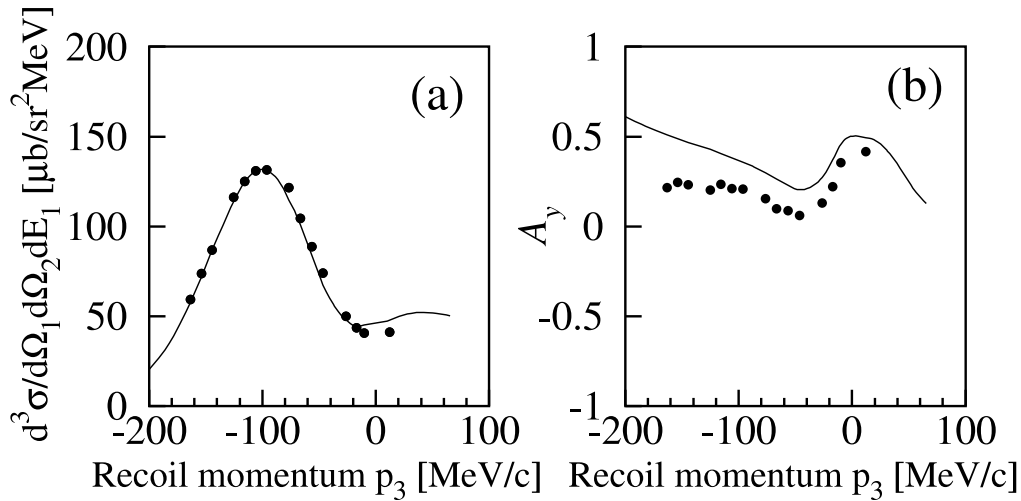
Figure 5.7: Cross section (a) and analyzing power (b) of the ^{40}Ca$(p, 2p)$ reaction for the peak at 8.3 MeV as functions of the recoil momentum p_3. The solid line represents the DWIA calculations fitted by the spectroscopic factor for the $1d_{3/2}$ orbital. The discrepancy in the A_y (b) between the data and the DWIA calculation is discussed in the text (Sec.5.2A.).

will be included in the peak as well. Since the contribution of the $2p_{3/2}$-hole state is negligibly small compared with those of the $2s_{1/2}$- and $1f_{7/2}$-hole states [9], the peak at 10.9 MeV was analyzed as the sum of the $2s_{1/2}$- and $1f_{7/2}$-hole states. We searched the best set of normalization factors for the calculated cross sections for the $2s_{1/2}$- and $1f_{7/2}$-hole states to reproduce the measured cross sections. The result is shown in Fig. 5.8 and the obtained spectroscopic factors are listed in Table 5.1. The fitted thick solid line for the cross section agrees well with the experimental data, but the calculated analyzing power is larger than the measurement, which is similar to the results for the $1d_{3/2}$-hole state.

The spectroscopic factors for the valence orbitals were reported from the previous $(p, 2p)$ [40, 79, 80] $(e, e'p)$ [47] and $(d,^3\mathrm{He})$ [9, 47, 81] reactions as listed in Table 5.1. The values from the $(p, 2p)$ reaction contradict because its measurement angles and used distorting potentials are different. This implies there is uncertainties in spectroscopic factors for the $(p, 2p)$ reaction owing to the distorting potential and the kinematical condition. The spectroscopic factors reported by Doll et $al.$ from the $(d,^3\mathrm{He})$ reaction are systematically larger than those from the $(e, e'p)$ reaction. However, Kramer et $al.$ reanalyzed the same $(d,^3\mathrm{He})$ data in Ref. [9] and showed that the spectroscopic factors for the $1d_{3/2}$ and $2s_{1/2}$ orbitals obtained from the $(e, e'p)$ and $(d,^3\mathrm{He})$ reactions are consistent [47]. As the obtained spectroscopic factors in the present work are larger than those consistent values from the $(e, e'p)$ and $(d,^3\mathrm{He})$ reaction and that for the $1d_{3/2}$-hole state is over the $2J + 1$, the obtained spectroscopic factors are overestimated. This leads that the DWIA calculation underestimated the absolute cross sections.

The phenomena that the measured analyzing powers were smaller than the calculation was previously observed and discussed by Noro et $al.$ [82], Miller et $al.$ [83], and Hatanaka et $al.$ [84]. Furthermore, a similar reduction in the polarization P was observed by Miklukho et $al.$ [85] and Andreev et $al.$ [86]. These authors suggested that the reduction might be caused by the influence of the effective mean
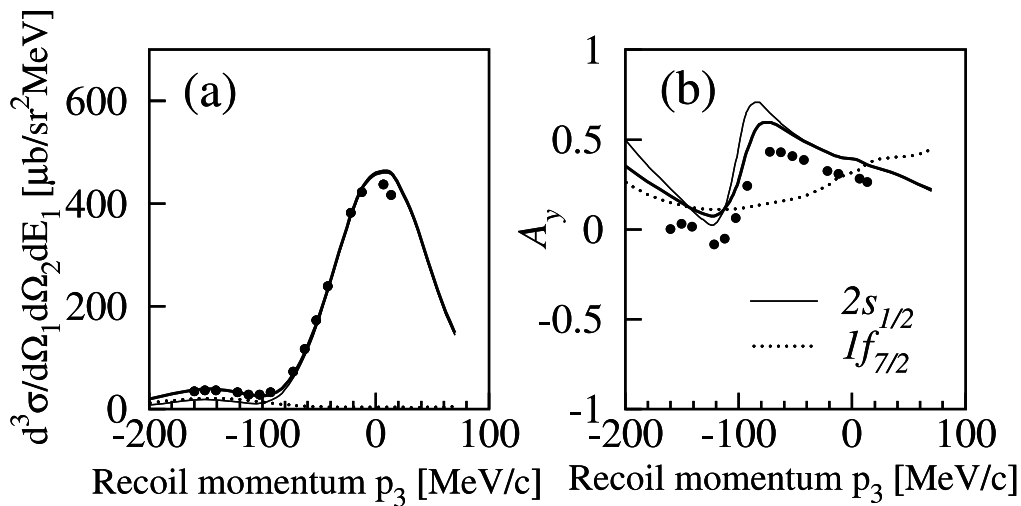
Figure 5.8: Results of the MDA for the peak at 10.9 MeV. The cross section (a) and the analyzing power (b) are shown as functions of the recoil momentum p_3. The thick solid line shows the fitted results. The thin solid line and the dotted line show the contributions of the $2s_{1/2}$ and $1f_{7/2}$ states, respectively. The discrepancy in the A_y (b) between the data and the DWIA calculation is discussed in the text (Sec.5.2A.).

density on the NN interaction. The systematic discrepancies between the experimental data and the DWIA calculation in Figs. 5.7 (b) and 5.8 (b) possibly imply the modification of the NN interaction in the nucleus. Although various extensive theoretical studies have been performed, no theoretical model has succeeded in reproducing the experimental analyzing power quantitatively.

The measured recoil-momentum distributions of the cross section for these two discrete peaks are well reproduced by fitting with the distributions calculated with the DWIA. The absolute values of the cross section might have uncertainties because the obtained spectroscopic factors are larger than those from other measurements. However, it was confirmed for the $L = 0$ and $L = 2$ orbitals that the DWIA calculation reproduces characteristic behavior of the recoil-momentum distribution depending on the orbital angular momentum L. The MDA for the deep-hole states uses the calculated recoil-momentum distributions of the cross section from different L orbitals, and first requires the reliability of them in reproducing a one-hole state for respective L orbitals. The result of these two discrete peaks assures validity for practicing the MDA for deep-hole states.

On the other hand, the recoil-momentum distribution of the analyzing power for the $1d_{3/2}$-hole state was not reproduced by the DWIA calculation even though it is a pure one-hole state. Therefore, the DWIA calculation of the analyzing power is not satisfactorily reliable, and we didn't accept the MDA with the analyzing power data and abandoned to distinguish the hole states of the $j_>$ and $j_<$ orbitals by using the analyzing power data. The results shown in the following sections are obtained from the MDA only with the cross-section data.

Table 5.1: Spectroscopic factors for the discrete peaks in the ^{40}Ca measurement. Kramer *et al.* reanalyzed the previous $(d,^3\text{He})$ data of Doll *et al.* in Ref. [9] in their study [47]. The present result is shown with the statistical uncertainty obtained in the fitting or MDA.

	E_{sep} [MeV]	Orbital	Spectroscopic factor
$(p, 2p)$			
E_p = 392 MeV, RCNP, Osaka			
Present work	8.3	$1d_{3/2}$	4.87 ± 0.09
	10.9	$2s_{1/2}$	1.61 ± 0.04
	10.9	$1f_{7/2}$	1.12 ± 0.06
E_p = 45.0–148.2 MeV, Maryland			
Samanta *et al.* [40]	8.33	$1d_{3/2}$	3.9–6.0
	10.85	$2s_{1/2}$	1.0–1.6
E_p = 200 MeV, TRIUMF, Antonuk *et al.* [38]			
Kudo and Miyazaki [79]	8.33	$1d_{3/2}$	1.46–3.37
Mano and Kudo [80]	8.33	$1d_{3/2}$	2.44–2.80
$(e, e'p)$			
NIKHEF			
Kramer *et al.* [47]	8.328	$1d_{3/2}$	2.58 ± 0.19
	10.850	$2s_{1/2}$	1.03 ± 0.07
$(d,^3\text{He})$			
E_d = 52 MeV, Karlsruhe			
Doll *et al.* [9]	8.33	$1d_{3/2}$	3.70
	10.85	$2s_{1/2}$	1.65
	11.15	$1f_{7/2}$	0.58
Kramer *et al.* [47] (reanalysis)	8.328	$1d_{3/2}$	2.30
	10.850	$2s_{1/2}$	1.03
E_d = 34.4 MeV, Oak Ridge			
Hiebert *et al.* [81]	8.33	$1d_{3/2}$	4.23
	10.86	$2s_{1/2}$	1.62
	11.15	$1f_{7/2}$	0.46

5.3   Results for deeply bound states

The MDA was performed for each 2-MeV bin in the separation energy region of 12–84 MeV with the cross section data. The hole states of the $1s_{1/2}$, $2s_{1/2}$, $1p$ and $1d$ orbitals were taken into account in the MDA since they are expected to dominate in the broad spectrum region from the naive shell-model picture. As hole states of $j_>$ and $j_<$ orbitals with the same L cannot be distinguished in the present MDA without the analyzing power, the single-particle-hole states were treated under the following assumptions.

Since the $1d$ orbital is split into the $1d_{3/2}$ and $1d_{5/2}$ orbitals and the $1d_{5/2}$ orbital is bound more deeply than $1d_{3/2}$ orbital, the hole state of the $1d_{5/2}$ orbital is expected to dominate the d-state strength at separation energies above 12 MeV. The relative strengths for the $1p_{1/2}$- and $1p_{3/2}$-hole states were fixed in the ratio of 2:4 as suggested by the naive shell-model picture. Since the recoil-momentum distributions of the cross sections for the $1s_{1/2}$- and $2s_{1/2}$-hole states are quite similar, the strengths for the $1s_{1/2}$- and $2s_{1/2}$-hole states cannot be distinguished by the MDA. Therefore, the strengths of the $2s_{1/2}$- and $1s_{1/2}$-hole states were assumed to be the s-hole-state strengths in the lower and higher separation-energy regions, respectively.

In Figs. 5.9–5.18, the recoil-momentum dependencies of the cross section and the analyzing power at the kinematical set2–5 are displayed. The error bars for the experimental data represent the statistical uncertainties. The thick solid lines in the figures of the cross section and the analyzing power indicate the fitted results by the MDA, and the other lines represent the contribution of the component hole states. Note that the analyzing power data was not used for the MDA. The lines in the figures of the analyzing power were drawn by using the results of the MDA with the cross section data.

The MDA was carried out for the data at the set2 with both the $2s_{1/2}$- and $1s_{1/2}$-hole states as a s-hole state because the border of the $2s_{1/2}$-and $1s_{1/2}$-hole states were unknown. Figures 5.9 and 5.10 are the results with the $2s_{1/2}$-hole state as a s-hole state while Figs. 5.11 and 5.12 are the results with the $1s_{1/2}$-hole state. The contributions from the $1d_{5/2}$- and $1p$-hole states are almost identical between in Figs. 5.9 and 5.11. The differences between the contributions from the $2s_{1/2}$- and $1s_{1/2}$-hole states are insignificant. The MDA for the data at the set3–5 was carried out with the $1s_{1/2}$-hole states as a s-hole state.

Figure 5.19 shows the typical examples of the fitted recoil-momentum distributions of the cross section and the analyzing power at separation energies of 17, 33, and 53 MeV. The fitted recoil-momentum distributions of the cross section reasonably well reproduce the measured cross-section data at each energy. It is found that the hole states of the $1d_{5/2}$, $1p$, and $1s_{1/2}$ orbitals are dominant in the recoil-momentum distributions of the cross section at 17, 33, and 53 MeV, respectively. However, the calculated analyzing power shown in Figs. 5.19(d)–5.19(f) overestimates the experimental data at all of these energies.

5.3.1 Strength distributions

After the MDA was performed, the strength distributions obtained for the $1s_{1/2}$-, $2s_{1/2}$-, $1p$-, and $1d_{5/2}$-hole states are shown in Fig. 5.20. The differences of the strengths of the $2s_{1/2}$- and $1s_{1/2}$-hole states are due to the differences of the magnitude of the calculated cross section. The strength distributions from the MDA results with the $2s_{1/2}$- and $1s_{1/2}$-hole states are in good agreement for the $1p$, and $1d_{5/2}$-hole states. Since the strength distribution obtained for the s-hole state has a minimum at 24 MeV, the s-hole state strengths were divided into the $2s_{1/2}$ and $1s_{1/2}$ strengths at 24 MeV.

The strength distributions obtained for the $1s_{1/2}$- and $1p$-hole states in Fig. 5.20 have hump structures

around 50 and 30 MeV, respectively. The hump of the $1p$-hole state around 30 MeV is consistent with the hump structure in separation energy spectra in Fig. 5.3.

5.3.2   Background consideration

The continuum physical backgrounds are also observed in the strength distributions. Although the continuum strengths are appreciable at separation energies larger than 80 MeV in the strength distributions for the $1s_{1/2}$ and $1p$-hole states, it is improbable that a single-particle-hole state has such a high separation energy. These strengths are considered to be the contributions of many-body processes such as $(p, 3p)$ or $(p, 2pn)$ reactions or multistep processes that follow the knock-out reaction.

In the $(p, 3p)$ and $(p, 2pn)$ reactions, the final states are four-body systems with the configurations of $3p+^{38}$Ar and $2p + n+^{38}$K, respectively. The phase-space volumes of the four-body final states were considered under the condition that two protons in the final state were detected by the GR and LAS but the other particles in the final states were not detected. The combined phase-space volume was obtained by averaging the phase-space volumes of the $(p, 3p)$ and $(p, 2pn)$ final states with equal weights. Since the ^{40}Ca$(p, 3p)^{38}$Ar and ^{40}Ca$(p, 2pn)^{38}$K reaction channels open at 14.7 and 21.4 MeV in the separation-energy spectrum for the ^{40}Ca$(p, 2p)^{39}$K reaction, respectively, the combined phase-space volume increases from 14.7 MeV.

For the multistep processes, Cowley *et al.* studied the contribution of the rescattering processes that follow the knock-out reaction to the coincidence measurement of the ^{40}Ca$(p, 2p)$ reaction [87]. The theoretical cross sections for the rescattering processes as an incoherent sum of the $(p, p'p'')$ and $(p, 2p)$ reactions well reproduced their experimental coincidence spectra. The contributions of the rescattering processes have shapes similar to the four-body phase space estimated here. Both of them gradually increase from the lower separation energy region. Thus, we have used the estimated four-body phase space as the background-shape model including the four-body and the rescattering processes; the adequacy of the model will be discussed later.

An asymmetric Lorentzian shape was suggested by Sartor and Mahaux to describe the spectral function of a hole state near the particle threshold [88]. It can be written as

$$f(E_{\text{sep}}) = N \frac{1 + (E_{\text{sep}} - E_c)A}{(E_{\text{sep}} - E_c)^2 + \frac{1}{4}\Gamma^2} \tag{5.1}$$

where E_c and Γ are the centroid energy and width of the peak, and N and A are a normalization parameter and an asymmetric parameter. When the parameter A becomes small, the function becomes symmetric. We fitted a combination of the asymmetric Lorentzian function and the estimated phase-space volume to the strength distributions for the $1s_{1/2}$, $1p$, and $1d_{5/2}$-hole states. The dotted lines in Fig. 5.21 show the phase-space volumes that seem to give reasonable background shapes. The background for the $2s_{1/2}$-hole state was determined to be of the same magnitude in the cross section as that for the $1s_{1/2}$-hole state.

The reduced χ^2 of $\chi^2_\nu = 1.0$ and 0.9 were obtained in the fit for the $1s_{1/2}$ and $1p$-hole states. The

Table 5.2: Centroid energies and widths (FWHM) of the strength distributions for the hole states of the $1p$ and $1s_{1/2}$ orbitals in ^{40}Ca. For the present result, the uncertainties were obtained as the region corresponding to a change of 1 in χ^2 from the minimum value in the fitting of the asymmetric Lorentzian and the background.

		Centroid (MeV)	Width (MeV)
Present work			
$(p, 2p)$	$1p$	29.6 ± 0.5	11.4 ± 1.2
	$1s_{1/2}$	48.4 ± 0.6	23.4 ± 1.1
Mougey *et al.*	$1p$	41	
$(e, e'p)$ [16]	$1s_{1/2}$	56	
Amaldi Jr. *et al.* [a]	$1p$	32 ± 4	18 ± 5
$(e, e'p)$ [19]	$1s_{1/2}$	77 ± 14	46 ± 24
Nakamura *et al.* [b]	$1p$	35 ± 1	21 ± 3
$(e, e'p)$ [18]	$1s_{1/2}$ (A)	58.7 ± 1.2	36 ± 1
	$1s_{1/2}$ (B)	58.4 ± 1.1	32 ± 1
Volkov *et al.* [c]	$1p_{1/2}$	29.8 ± 0.1	8.5 ± 1.1
$(p, 2p)$ [22]	$1p_{3/2}$	34.7 ± 0.3	9.4 ± 1.2
	$1s_{1/2}$	53.6 ± 0.7	18.8 ± 14

[a]The values were obtained by fitting Maxwellian curves to the separation-energy spectra. We evaluated the listed widths from the values given in Ref. [19] (where the authors show the distances between the zero and the maximum of the Maxwellian curve) by regarding them as a 3σ in Gaussian function.

[b]Two results (A) and (B) were presented for the $1s_{1/2}$ orbital.

[c]Volkov *et al.* disentangled the $1p_{1/2}$ and $1p_{3/2}$-hole states by fitting the separation-energy spectra with some Gaussian functions.

reduced χ^2 is defined as $\chi^2_\nu = \chi^2/\nu$, where ν is the number of degrees of freedom in the fit. In the χ^2 fit for the $1d_{5/2}$-hole state, χ^2_ν value of 2.3 was obtained, that is, it was larger than 1. If the model in the fit were perfect, χ^2_ν would be 1. The larger χ^2_ν is due to an inadequate model used in the fit. To compensate this inadequacy of the model, the uncertainties in the parameters were estimated in the $1d_{5/2}$-hole state case, following the method of Terashima *et al.* in Ref. [89]. The uncertainties in the strength data were artificially increased by multiplying all the strength uncertainties by a constant factor so that χ^2_ν became 1, and so increased uncertainties in the parameters were obtained. The increased uncertainties involve the model uncertainties that originate in the inadequacy of the model, and they were defined as the total uncertainties. The uncertainties estimated without increase in the uncertainties in the strength data were defined as the statistical uncertainties.

The centroid energies (E_c) and widths (Γ) of the peaks for the $1s_{1/2}$- and $1p$-hole states were obtained as the parameters of the asymmetric Lorentzian function in the fit; they are listed in Table 5.2 with the results from the previous experiments. The total uncertainties in the centroid energies and widths were estimated as mentioned before. The centroid energies of the $1p$ and $1s_{1/2}$-hole states are deduced to be 29.6 ± 0.5 and 48.4 ± 0.6 MeV, respectively.

The spectroscopic factors obtained by subtraction of the fitted four-body background are listed in

Table 5.3: Spectroscopic factors relative to the IPSM limits for the orbitals in ^{40}Ca. They are obtained after the background subtraction in the present study. The second uncertainty, in parentheses, is the statistical uncertainty estimated by the propagation of the strength uncertainties at each 2-MeV bin and the uncertainty of the contribution of the background. The first one is the total uncertainty that includes also the model uncertainty, which is mentioned in the text. The spectroscopic factors deduced by the DWIA calculation with the nonlocality correction are also shown. The detail discussion is given in Chap. 6.

		Spectroscopic factor	
	IPSM limit		with nonlocality correction
$1d_{3/2}$	4	$1.22 \pm 0.02(\pm 0.02)$	$0.92 \pm 0.02(\pm 0.02)$
$1f_{7/2}$	8	$0.14 \pm 0.01(\pm 0.01)$	$0.10 \pm 0.01(\pm 0.01)$
$2s_{1/2}$	2	$1.00 \pm 0.03(\pm 0.03)$	$0.75 \pm 0.02(\pm 0.02)$
$1d_{5/2}$	6	$1.60 \pm 0.12(\pm 0.11)$	$1.19 \pm 0.09(\pm 0.08)$
$1p$	6	$0.93 \pm 0.12(\pm 0.12)$	$0.71 \pm 0.08(\pm 0.08)$
$1s_{1/2}$	2	$1.69 \pm 0.10(\pm 0.10)$	$1.36 \pm 0.12(\pm 0.10)$

Table 5.4: Spectroscopic factors relative to the IPSM limits for the orbitals in ^{40}Ca without background subtraction. The uncertainty is the statistical uncertainty estimated by the propagation of the strength uncertainties at each 2-MeV bin.

		Spectroscopic factor	
	IPSM limit		with nonlocality correction
$2s_{1/2}$	2	1.02 ± 0.03	0.77 ± 0.02
$1d_{5/2}$	6	2.23 ± 0.11	1.73 ± 0.08
$1p$	6	1.87 ± 0.07	1.32 ± 0.05
$1s_{1/2}$	2	2.53 ± 0.05	1.89 ± 0.04

Table 5.3, together with the total and statistical uncertainties. The spectroscopic factors without background subtraction are listed in Table 5.4 with only statistical uncertainties.

The spectroscopic factors of the $2s_{1/2}$ and $1p$ orbitals are consistent with 100% within the uncertainty, whereas the spectroscopic factors of $1d_{3/2}$, $1d_{5/2}$ and $1s_{1/2}$-hole states are over 100% of the $2J+1$ values. The spectroscopic factors of over 100% implies the uncertainty of the DWIA calculation, as mentioned in Sec. 5.2. The absolute value of the spectroscopic factor is discussed in Chap. 6.
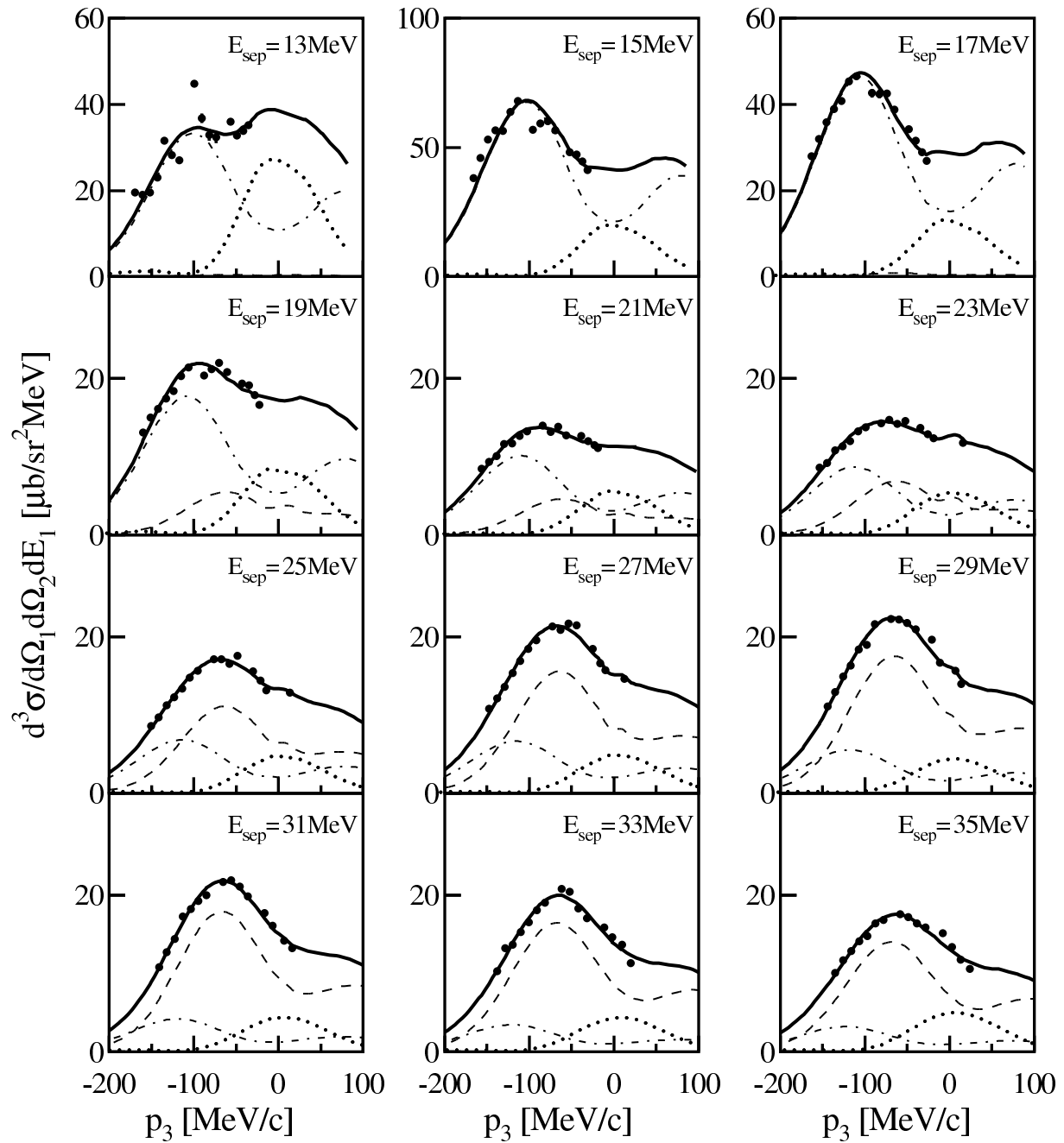
Figure 5.9: Cross section for each 2-MeV bin in the separation energy at the set2 as a function of the recoil momentum p_3. The thick solid line shows the MDA results including $2s_{1/2}$-hole state as a s-hole state. The dotted lines, the short-dashed lines, and the dash-dotted lines show the contributions of $2s_{1/2}$-, $1p$-, and $1d_{5/2}$-hole states, respectively.
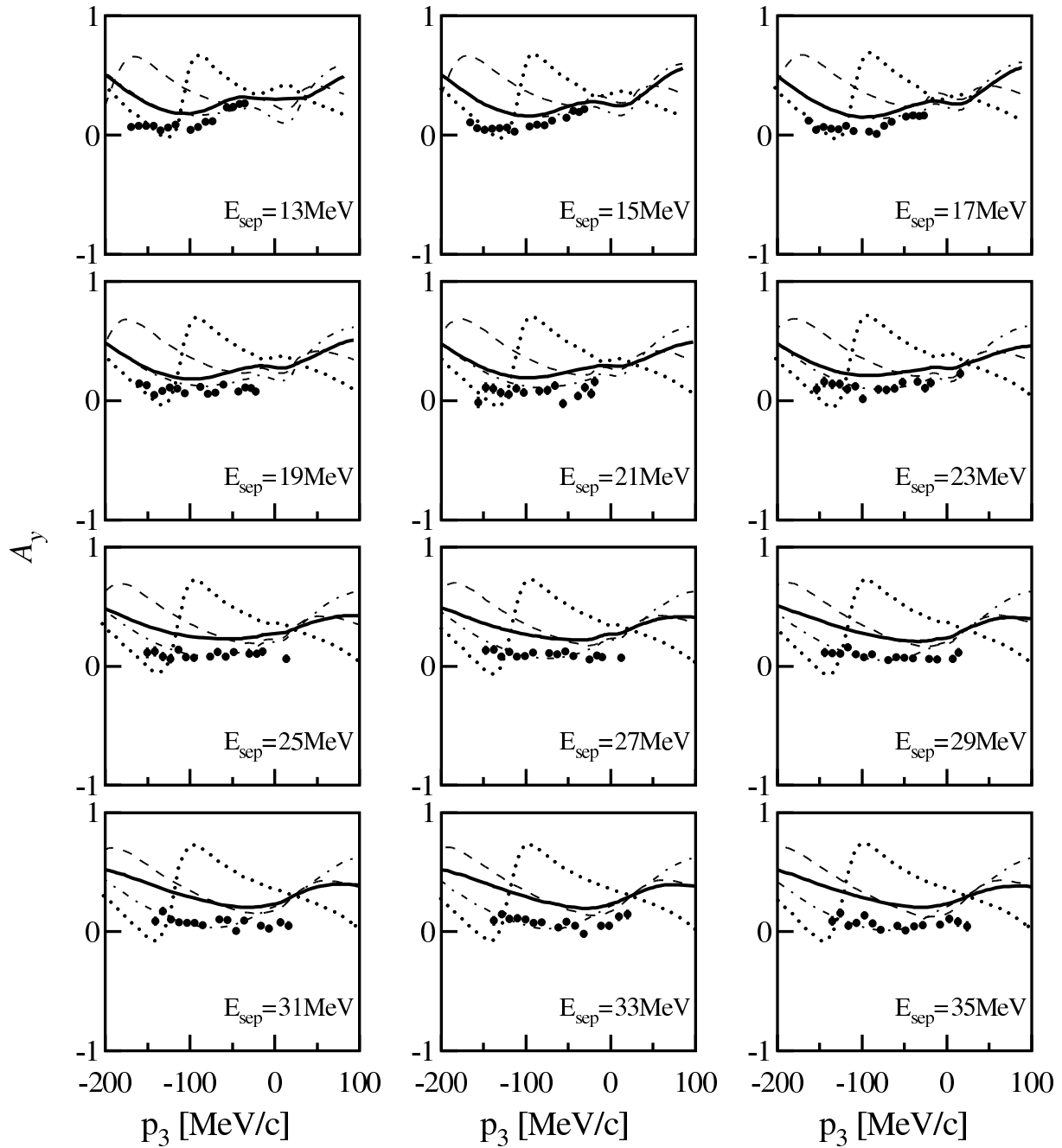
Figure 5.10: Analyzing power for each 2-MeV bin in the separation energy at the set2 as a function of the recoil momentum p_3. The thick solid line shows the MDA results including $2s_{1/2}$-hole state as a *s*-hole state. The analyzing power data was not included in the MDA. The dotted lines, the short-dashed lines, and the dash-dotted lines show the contributions of $2s_{1/2}$-, $1p$-, and $1d_{5/2}$-hole states, respectively.
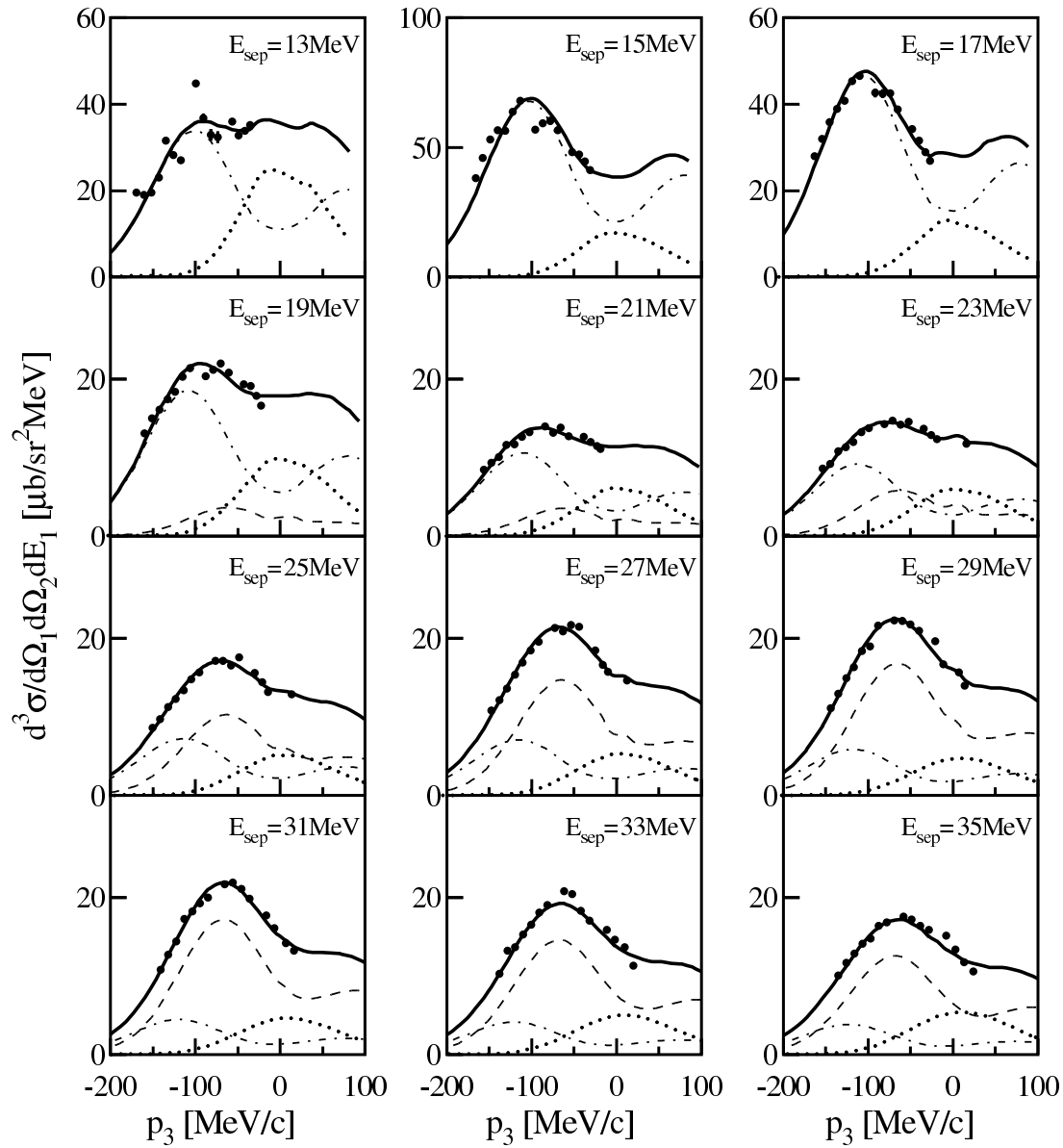
Figure 5.11: Cross section for each 2-MeV bin in the separation energy at the set2 as a function of the recoil momentum p_3. The thick solid line shows the MDA results including $1s_{1/2}$-hole state as a s-hole state. The dotted lines, the short-dashed lines, and the dash-dotted lines show the contributions of $1s_{1/2}$-, $1p$-, and $1d_{5/2}$-hole states, respectively.
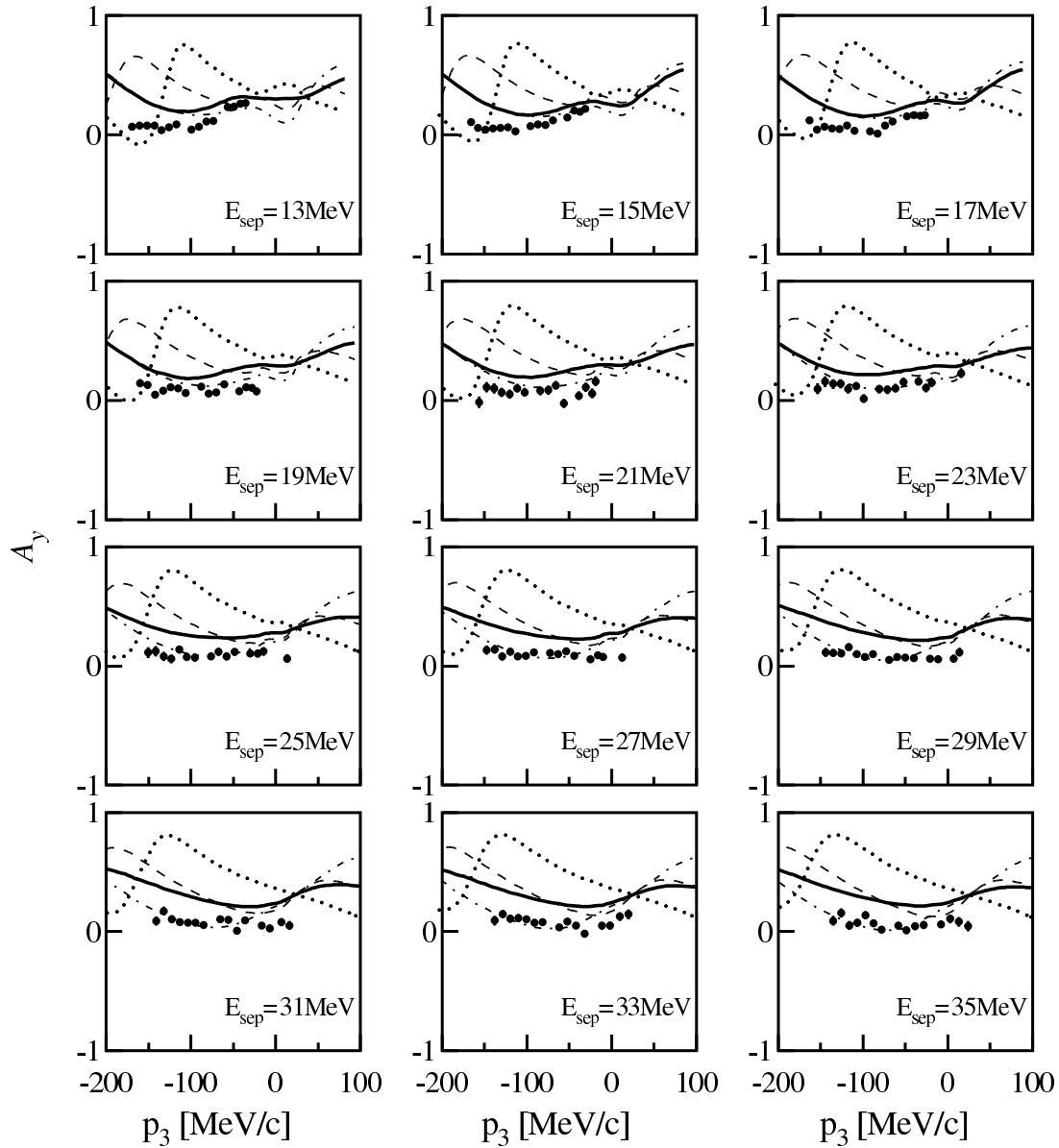
Figure 5.12: Analyzing power for each 2-MeV bin in the separation energy at the set2 as a function of the recoil momentum p_3. The thick solid line shows the MDA results including $1s_{1/2}$-hole state as a s-hole state. The analyzing power data was not included in the MDA. The dotted lines, the short-dashed lines, and the dash-dotted lines show the contributions of $1s_{1/2}$-, $1p$-, and $1d_{5/2}$-hole states, respectively.
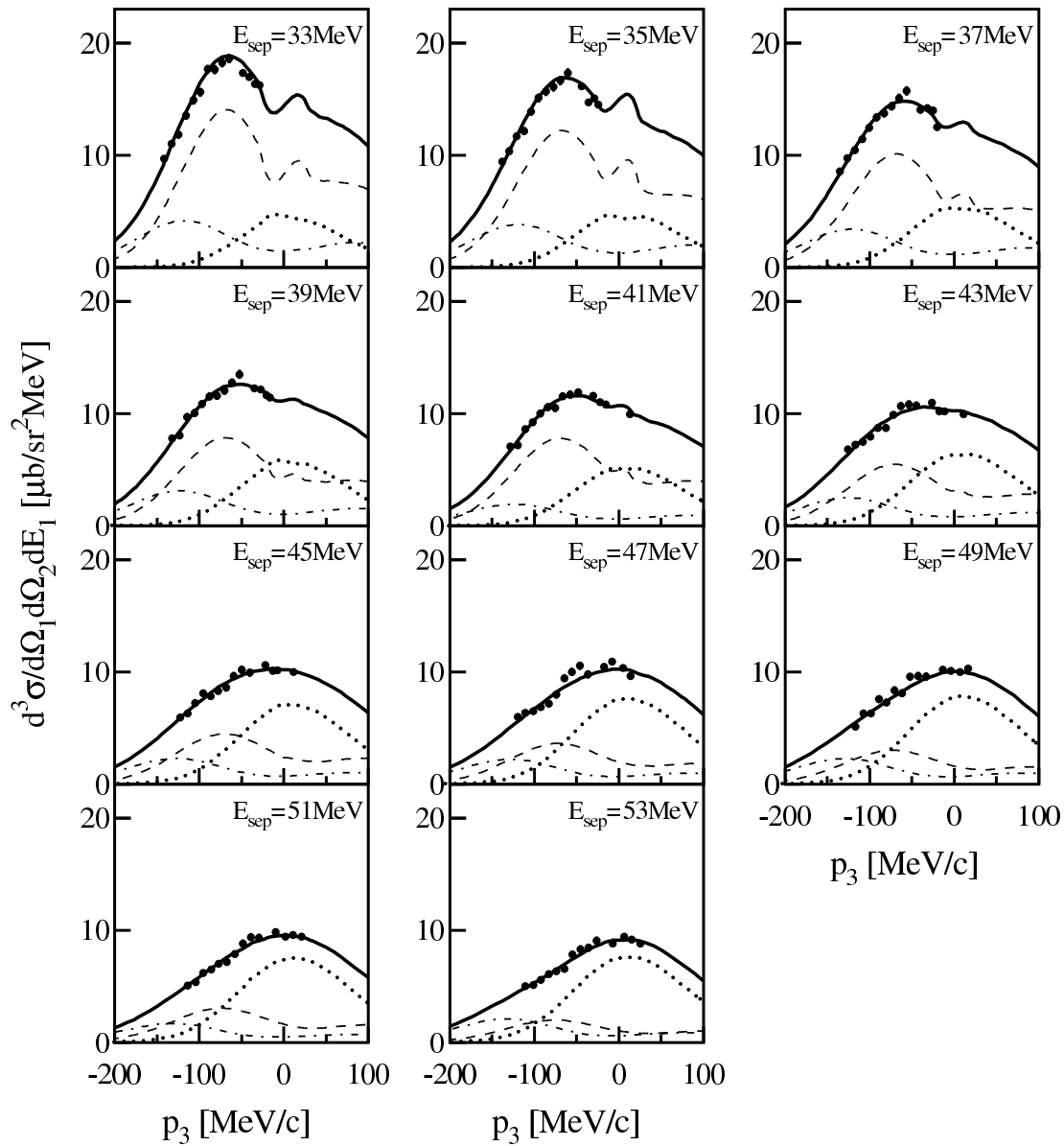
Figure 5.13: Cross section for each 2-MeV bin in the separation energy at the set3 as a function of the recoil momentum p_3. The thick solid line shows the MDA results. The dotted lines, the short-dashed lines, and the dash-dotted lines show the contributions of $1s_{1/2}$-, $1p$-, and $1d_{5/2}$-hole states, respectively.
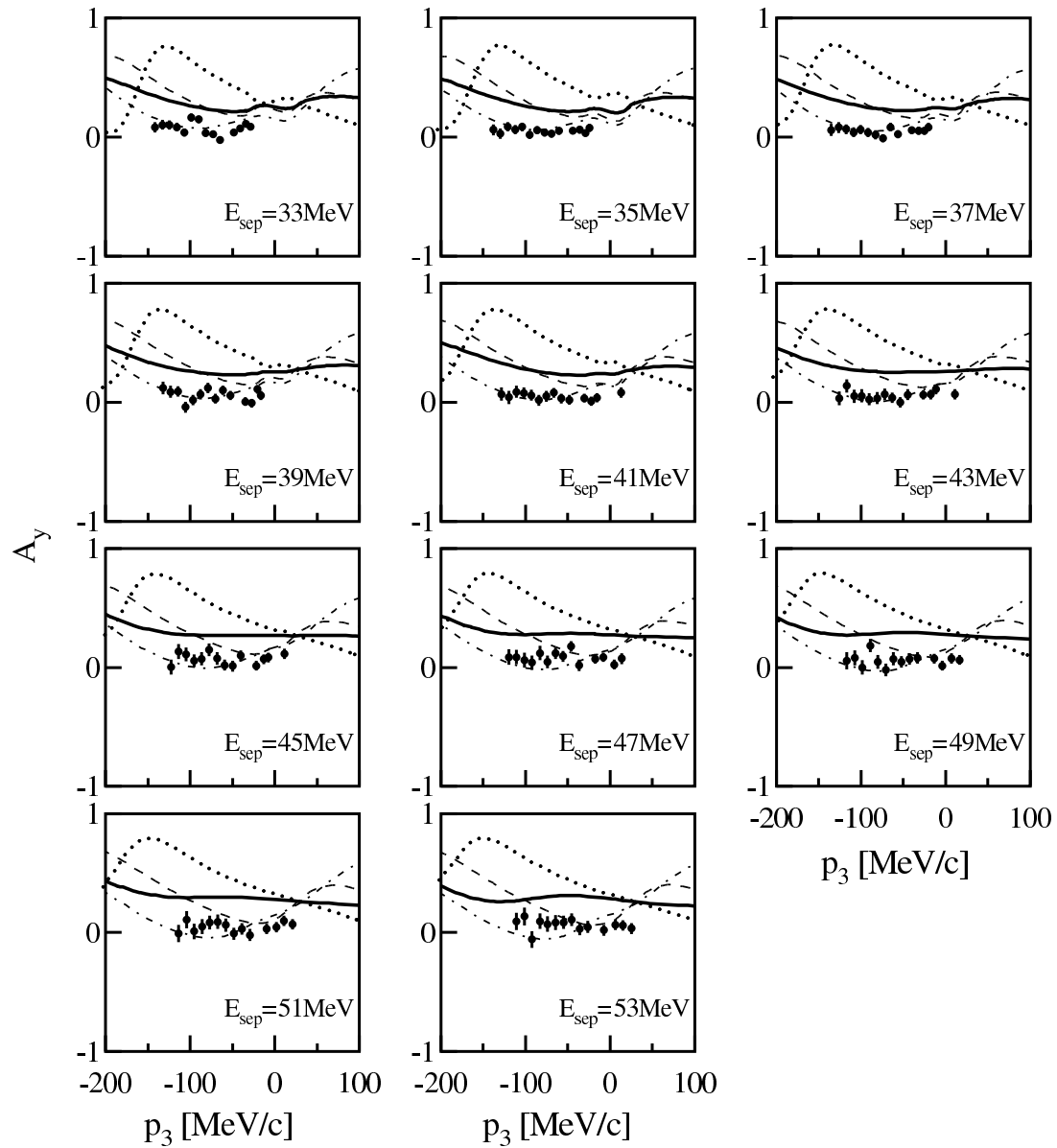
Figure 5.14: Analyzing power for each 2-MeV bin in the separation energy at the set3 as a function of the recoil momentum p_3. The analyzing power data was not included in the MDA. The dotted lines, the short-dashed lines, and the dash-dotted lines show the contributions of $1s_{1/2}$-, $1p$-, and $1d_{5/2}$-hole states, respectively.
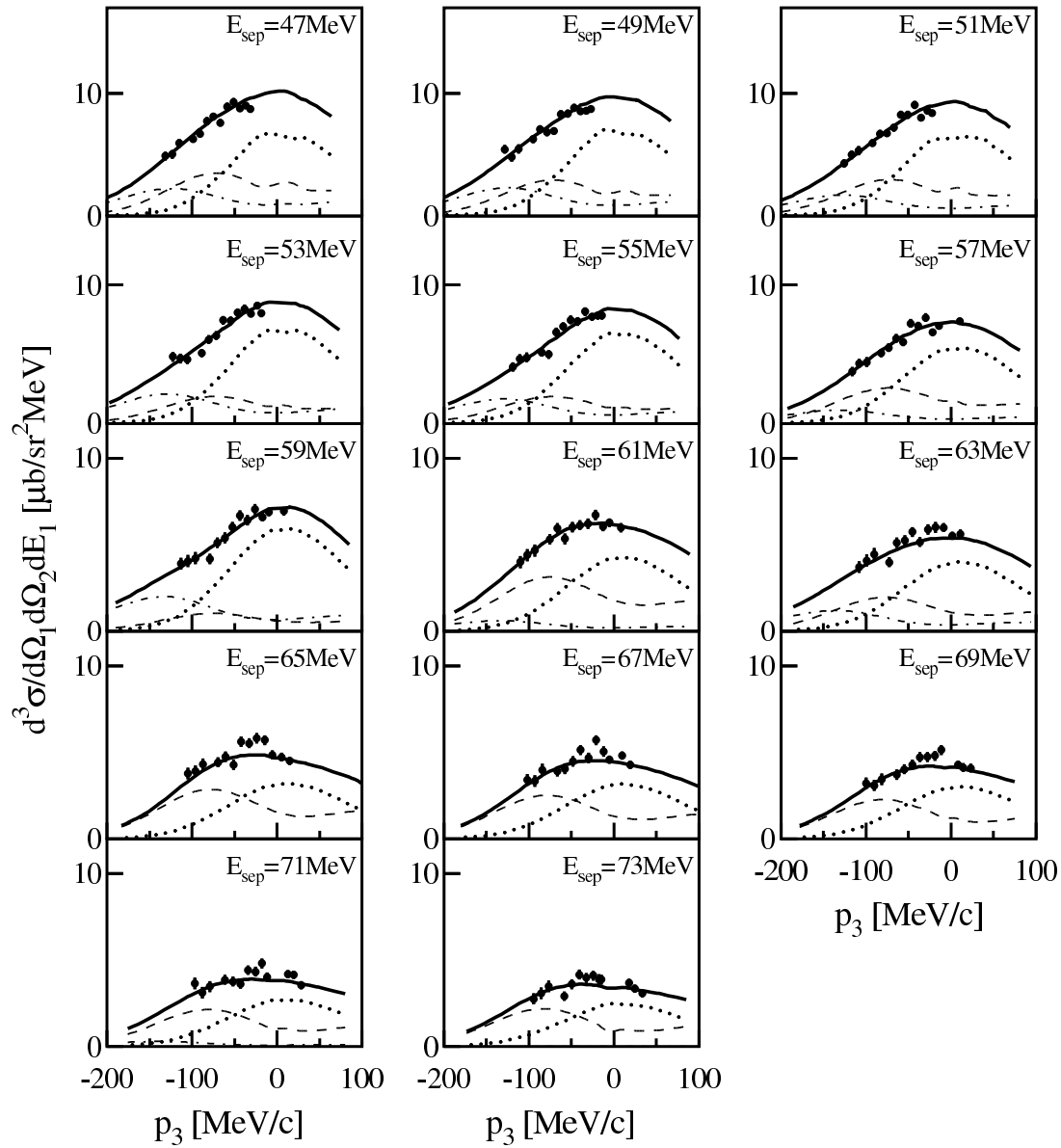
Figure 5.15: Cross section for each 2-MeV bin in the separation energy at the set4 as a function of the recoil momentum p_3. The thick solid line shows the MDA results. The dotted lines, the short-dashed lines, and the dash-dotted lines show the contributions of $1s_{1/2}$-, $1p$-, and $1d_{5/2}$-hole states, respectively.
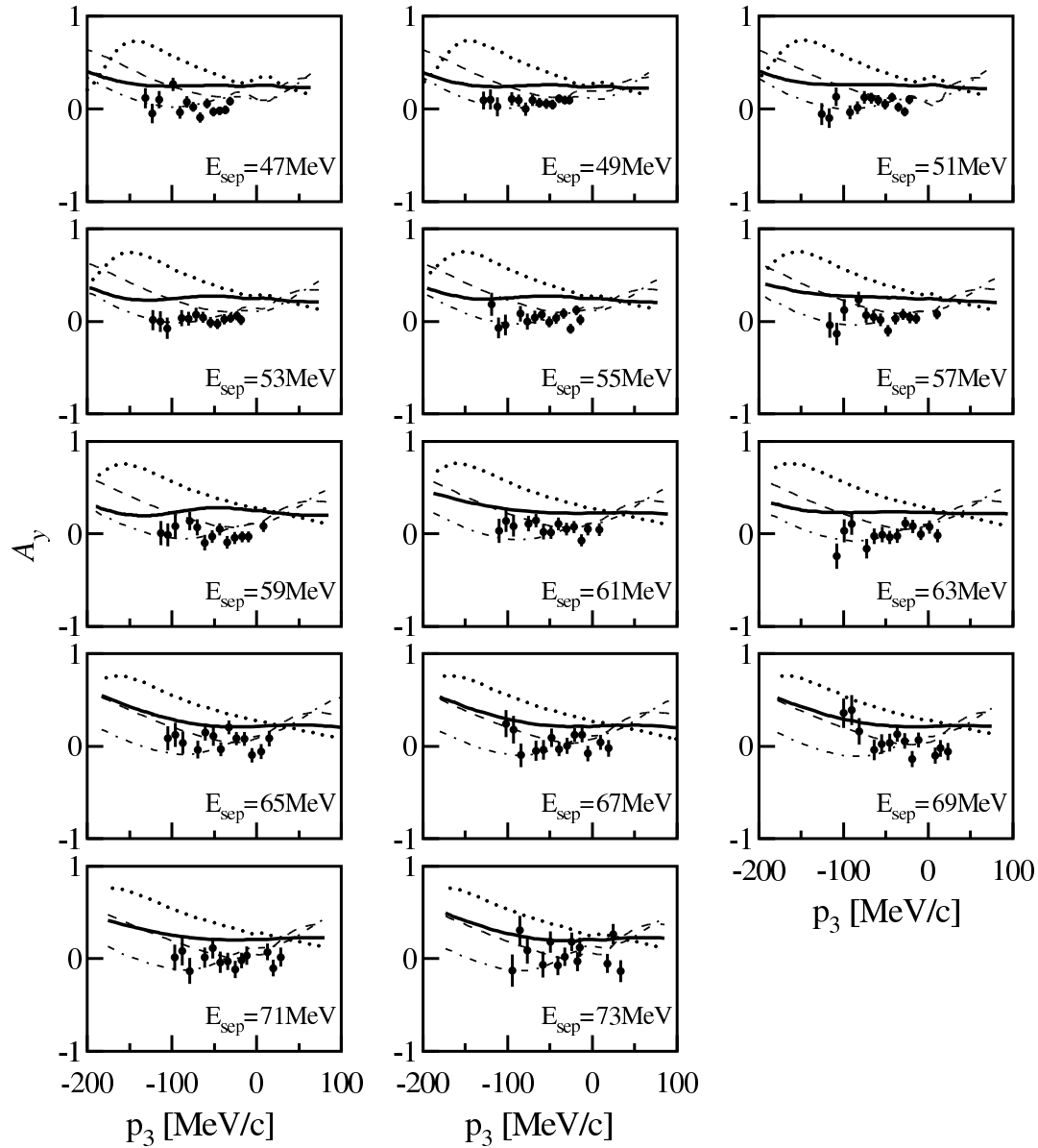
Figure 5.16: Analyzing power for each 2-MeV bin in the separation energy at the set4 as a function of the recoil momentum p_3. The analyzing power data was not included in the MDA. The dotted lines, the short-dashed lines, and the dash-dotted lines show the contributions of $1s_{1/2}$-, $1p$-, and $1d_{5/2}$-hole states, respectively.
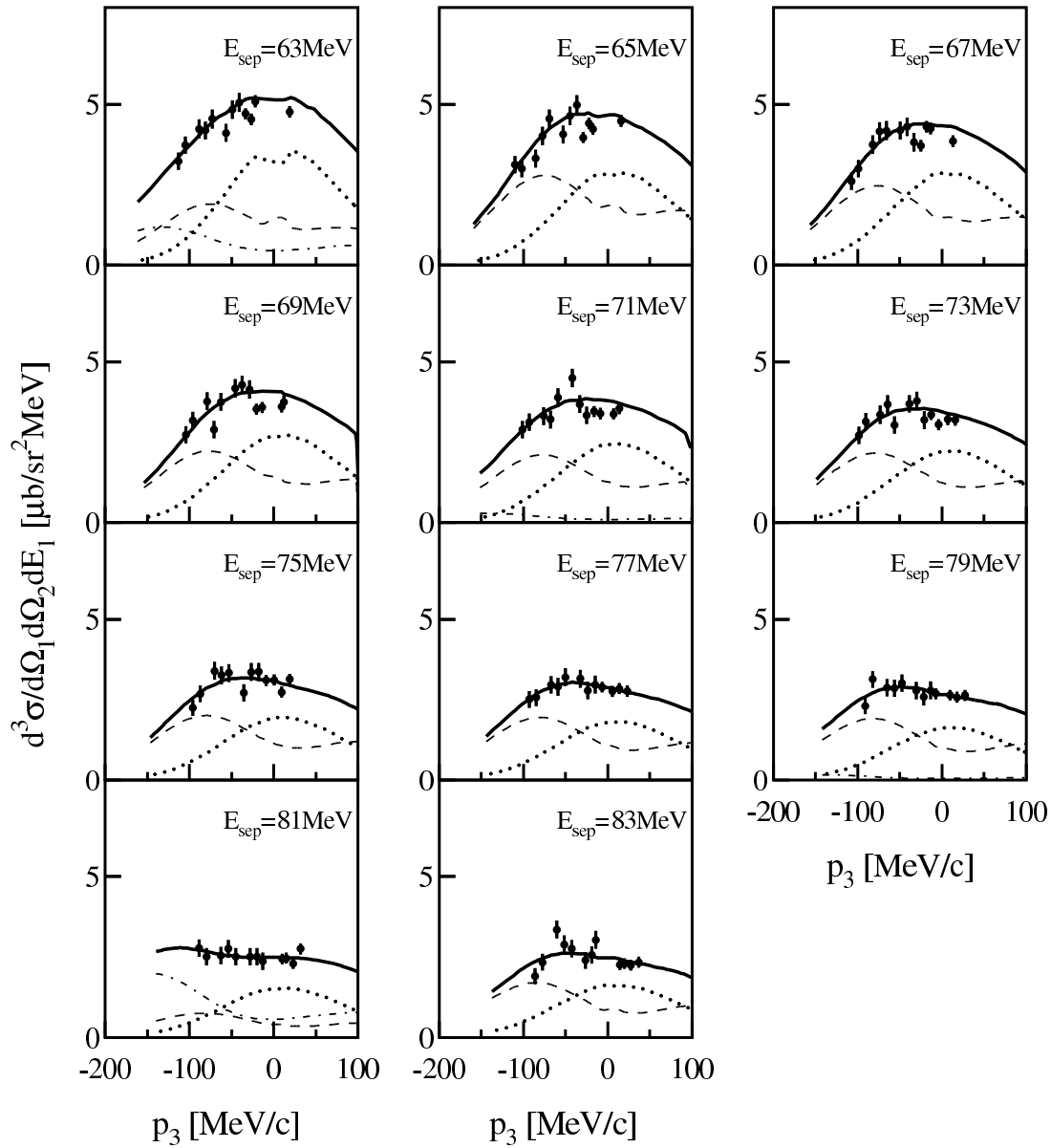
Figure 5.17: Cross section for each 2-MeV bin in the separation energy at the set5 as a function of the recoil momentum p_3. The thick solid line shows the MDA results. The dotted lines, the short-dashed lines, and the dash-dotted lines show the contributions of $1s_{1/2}$-, $1p$-, and $1d_{5/2}$-hole states, respectively.
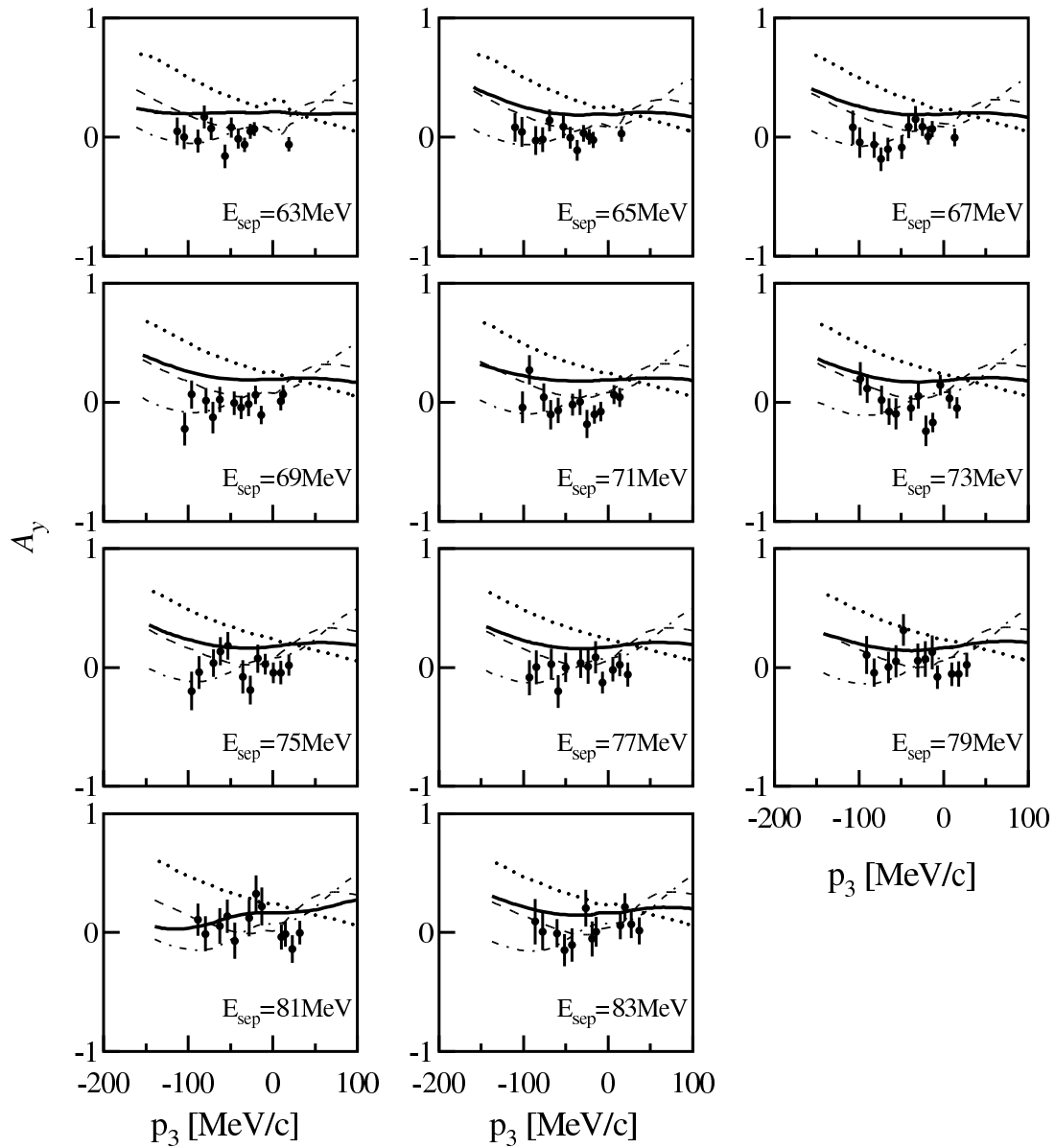
Figure 5.18: Analyzing power for each 2-MeV bin in the separation energy at the set5 as a function of the recoil momentum p_3. The analyzing power data was not included in the MDA. The dotted lines, the short-dashed lines, and the dash-dotted lines show the contributions of $1s_{1/2}$-, $1p$-, and $1d_{5/2}$-hole states, respectively.
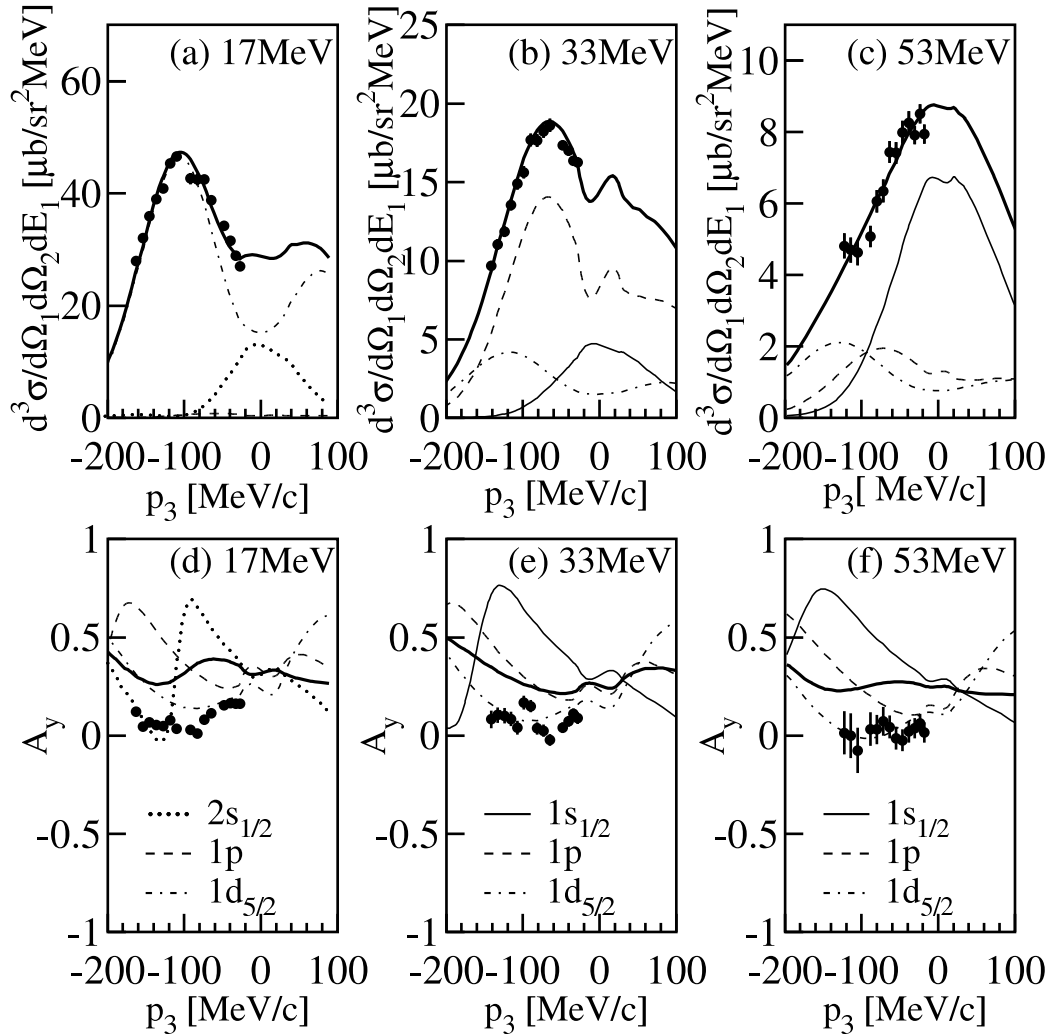
Figure 5.19: Cross section and analyzing power as a function of the recoil momentum p_3 for the selected separation-energy bins at 17 [(a) and (d)], 33 [(b) and (e)] and 53 MeV [(c) and (f)]. The thick solid lines show the MDA results. The thin solid lines, the dotted lines, the short-dashed lines, and the dash-dotted lines show $1p$-, and $1d_{5/2}$-hole states, respectively.
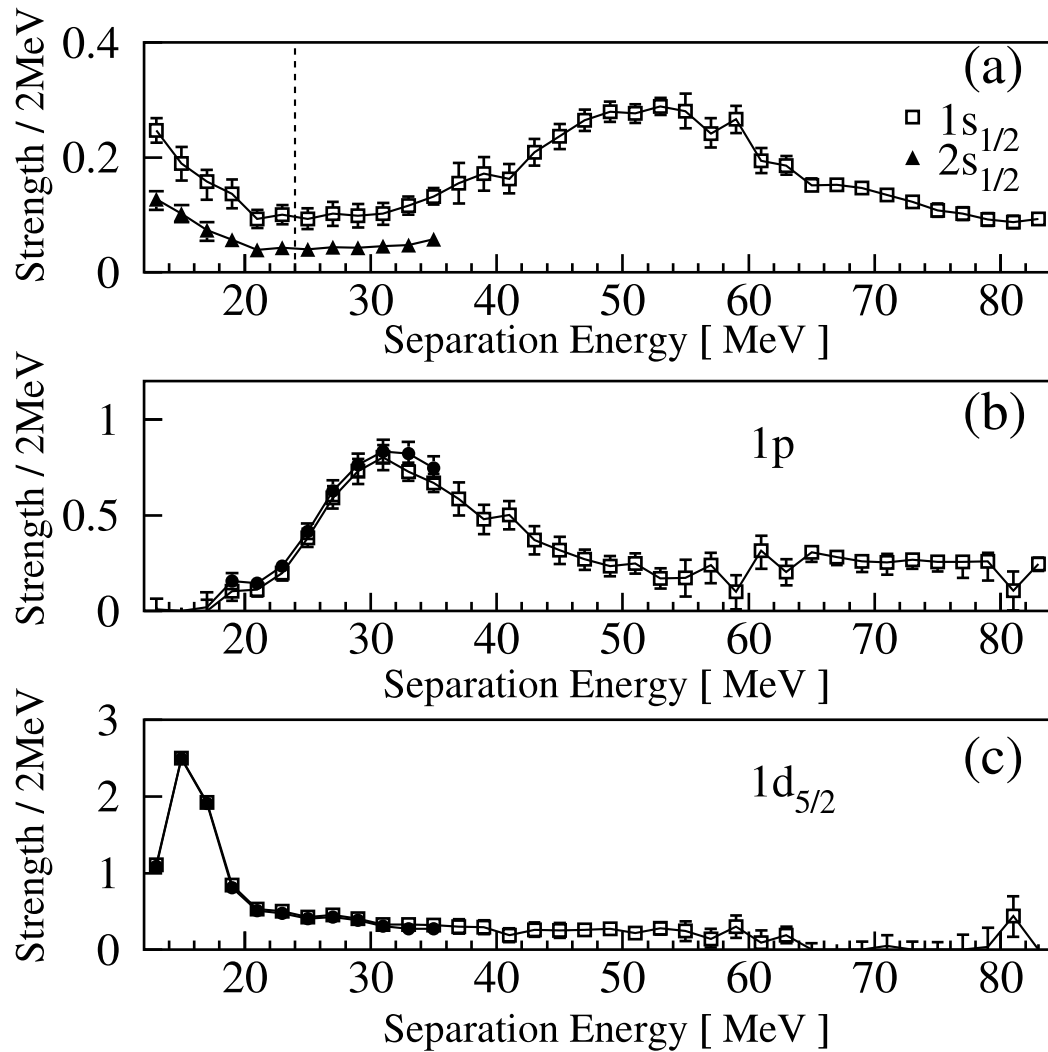
Figure 5.20: Strength distributions obtained in the separation-energy region of 12–84 MeV. The solid lines are shown to guide the eyes. The vertical dotted line at 24 MeV in (a) shows the border where the s-hole state contribution was divided into the contribution of the $2s_{1/2}$-hole state and that of the $1s_{1/2}$-hole state.
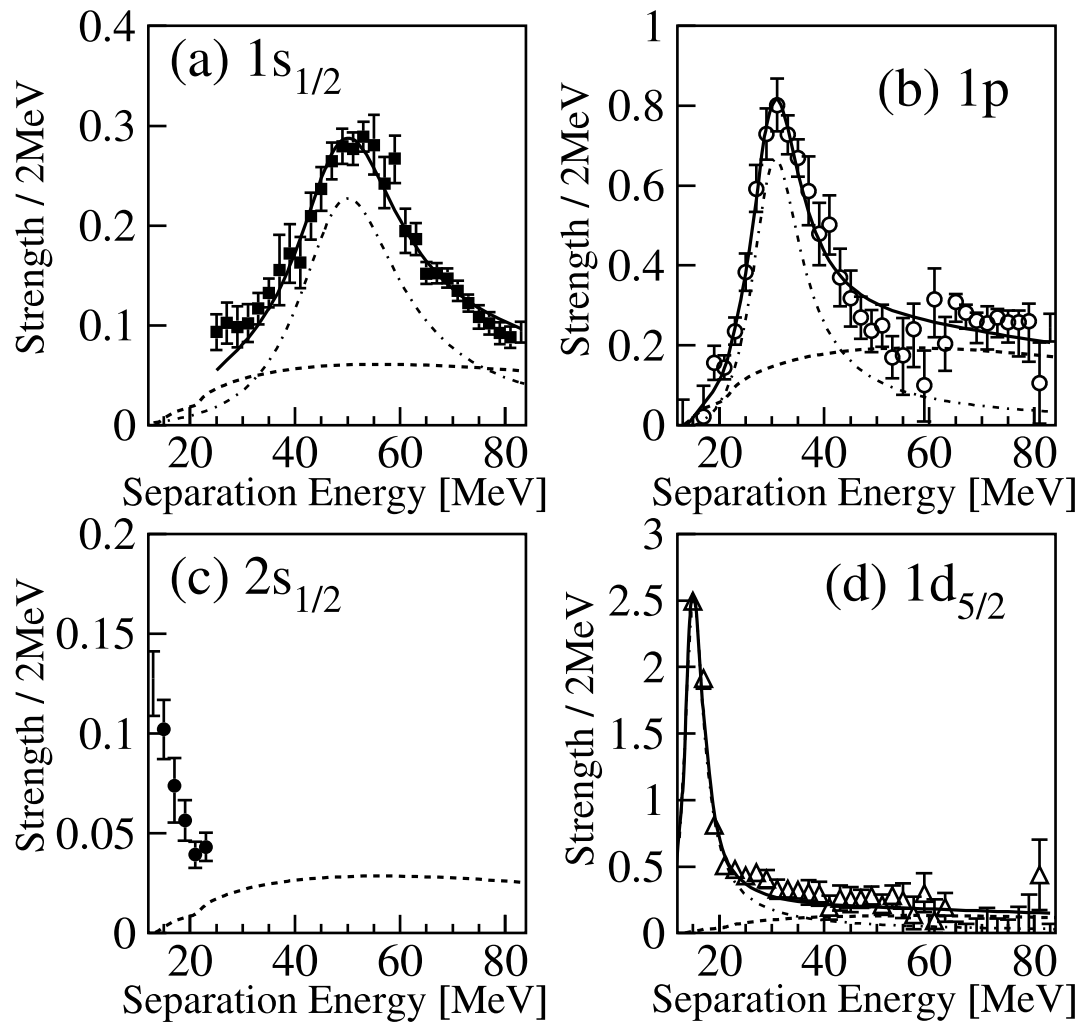
Figure 5.21: Strength distributions for the hole states of the (a) $1s_{1/2}$, (b) $1p$, (c) $2s_{1/2}$, and (d) $1d_{5/2}$ orbitals in the separation energy region of 12–84 MeV. The solid lines and the dash-dotted lines in the figures for the $1s_{1/2}$-, $1p$- and $1d_{5/2}$-hole states show the fitted curves and the fitted asymmetric Lorentzian functions, respectively. The short-dashed lines show the estimated contribution of the four-body background.

Chapter 6

Discussion

6.1 Strength distribution of the deep-hole states

The strengths for the orbital states for each 2-MeV bin were independently obtained by the MDA at each 2-MeV bin, that is, the strength distributions in Fig. 5.20 were obtained without any assumption on the shape of the distribution. This is different from the previous analyses by Volkov *et al.* [22] and by Nakamura *et al.* [18]. The obtained strength distribution shows clearer shapes than those from the previous experiments, which are shown in Figs. 1.3, 1.4, 1.5, and 1.6 in Chap. 1. It was useful to discuss the strength distributions and the contribution of the background.

In Fig. 6.1, the centroids and widths of the strength distributions for the $1p$- and $1s_{1/2}$-hole states are compared with those obtained from the previous experiments listed in Table 5.2. Vertical lines in Fig. 6.1 indicate uncertainties of the centroids as the standard deviation. The centroid energies for the $1p$- and $1s_{1/2}$-hole states were determined with small uncertainties in the present analysis. The obtained centroid energies and widths of the $1p$ and $1s_{1/2}$-hole states are close to the results from the $(p, 2p)$ experiment at PNPI [22]. The centroid values from the present work are the smallest among the listed values.

Since the centroid of the obtained distribution for the $1p$-hole state corresponds to the peak position at 30 MeV in the separation energy spectra in Fig. 5.3, the peak at 30 MeV in the separation energy spectra should be the peak of $1p$-hole state. This correspondence assures that the MDA reliably worked. Furthermore, it shows that a one-hole state can be observed even for such a deeply bound orbital.

The success in obtaining the strength distributions relies on the good reproduction of the recoil-momentum distribution of the cross section for a one-hole state, which is confirmed by analyzing two low-lying discrete peaks.
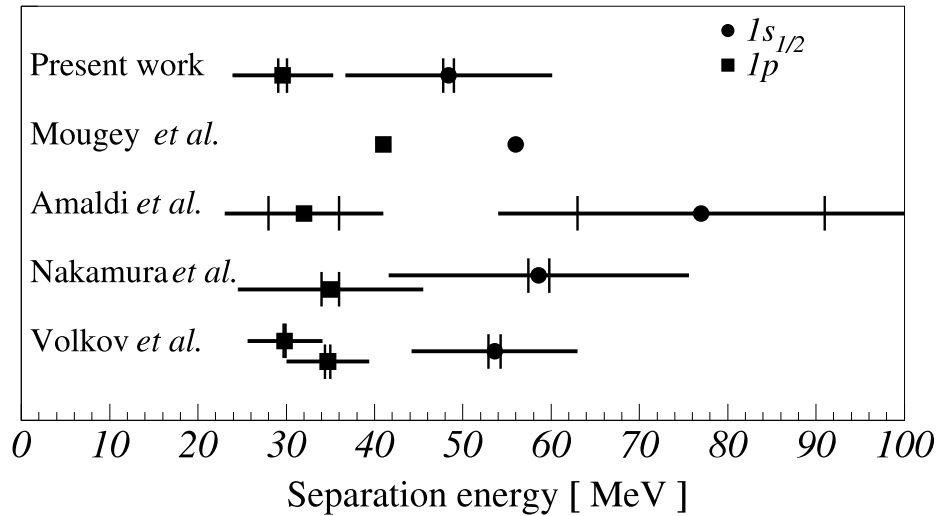
Figure 6.1: Centroids (symbols) and FWHM widths (solid lines) of the strength distributions for the $1p$- and $1s_{1/2}$-hole states with those obtained from the previous experiments, from Table 5.2. Vertical lines indicate uncertainties of the centroids as standard deviation. Mougey *et al.* did not give the uncertainties.

6.2   DWIA calculation

For the first two peaks at 8.3 and 10.9 MeV in the separation energy spectra, the cross sections and the analyzing powers are reproduced by the DWIA calculation qualitatively well as shown in Figs. 5.7 and 5.8, and the peaks seem to involve scarcely any background. Nevertheless the spectroscopic factor for the $1d_{3/2}$-hole state exceeds 100% of the $2J+1$ value, and that of the $2s_{1/2}$-hole state is much larger than the experimental values from the $(e, e'p)$ and $(d, {}^3\text{He})$ reactions as shown in Table 5.1. Here the validity of the DWIA calculation is discussed for the hole states of the valence orbitals in the following paragraphs. For the $1d_{3/2}$, $2s_{1/2}$ and $1f_{7/2}$-hole states, the DWIA calculation was performed with different parameters to examine uncertainties in the obtained spectroscopic factors.

First, the results of the DWIA calculation with various distorting potentials are displayed in Figs. 6.2 and 6.3. The several parameter sets of Cooper *et al.* [72] and Hama *et al.* [90] were used as the distorting potential. The used potentials are listed in Table 6.1; the obtained spectroscopic factors for the respective potentials are shown in Fig 6.4. The calculations by the plane-wave-impulse approximation (PWIA) are also displayed by thick solid lines in Figs. 6.2 and 6.3 to investigate the contribution of the distortion. The contribution from the $2s_{1/2}$-hole state is displayed but that from the $1f_{7/2}$-hole state is not in Fig. 6.3 for simplicity.

In Figs. 6.2 and 6.3, all the results of the DWIA calculation with various potentials qualitatively reproduced the experimental data as well as the result with EDAD1 used in the previous chapter, and the recoil-momentum distributions of the cross section and the analyzing power for the used distorting potentials are almost indistinguishable. Comparing the DWIA calculation with the PWIA calculation in

Table 6.1: Global optical potentials used for the distortion in the DWIA calculation.

Potential	Data for fit	Num. of parameters	Reference
EDAD1	^{12}C, ^{16}O, ^{40}Ca, ^{90}Zr, ^{208}Pb(p, p) 20-1040 MeV	106	[72]
EDAD2	^{12}C, ^{16}O, ^{40}Ca, ^{90}Zr, ^{208}Pb(p, p) 20-1040 MeV	154	[72]
EDAD3	^{12}C, ^{16}O, ^{40}Ca, ^{90}Zr, ^{208}Pb(p, p) 20-1040 MeV	176	[72]
EDAICA	^{40}Ca(p, p) 20-1040 MeV	70	[72]
DP1	^{40}Ca, ^{48}Ca, ^{56}Fe, ^{60}Ni, ^{90}Zr, ^{208}Pb(p, p) 65-1040 MeV	80	[90]
DP2	^{40}Ca, ^{48}Ca, ^{56}Fe, ^{60}Ni, ^{90}Zr, ^{208}Pb(p, p) 65-1040 MeV	84	[90]
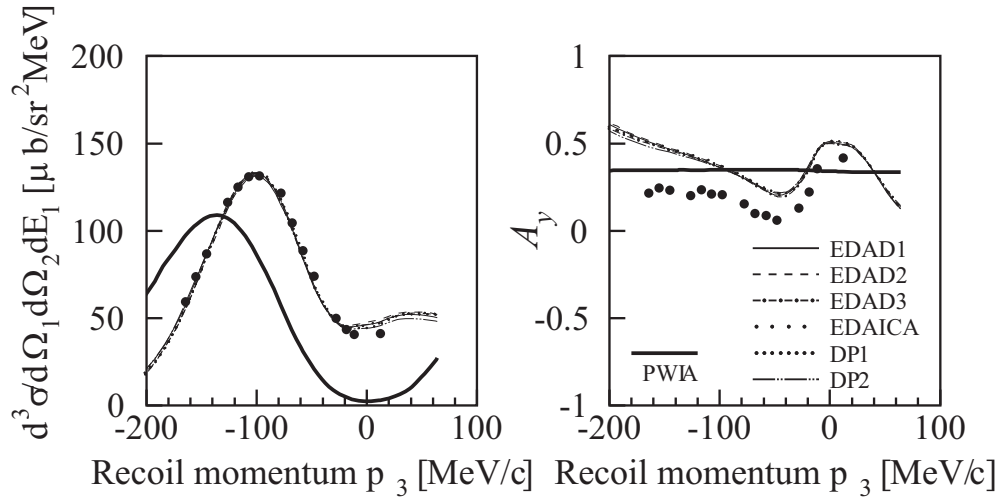
Figure 6.2: DWIA calculations of the ^{40}Ca$(p, 2p)$ reaction for the $1d_{3/2}$-hole state at 8.3 MeV with different optical potentials. The parameter sets of Cooper *et al.* (EDAD2, EDAD3, EDAICA) [72] and of Hama *et al.* (DP1, DP2) [90] were used for the distorting potential. The strengths of the $1d_{3/2}$-hole state were obtained by fitting to the experimental data. The thick solid line indicates the PWIA calculation.

Figs. 6.2 and 6.3, it is found that the distorting potential plays an important role to reproduce the recoil-momentum distribution of the cross section and the analyzing power. The qualitative reproduction of the cross section and the analyzing power shows that the DWIA works well to reproduce the data for the 392-MeV proton. The obtained spectroscopic factors in Fig 6.4 shows that the cross sections by the DWIA calculation are reduced to about 20–30% of the PWIA values and the relative strength between these three orbitals are nearly invariable. However, all of the spectroscopic factors are much larger than the results from the $(e, e'p)$ and $(d,^3$He) reactions.

Second, the sensitivity of the spectroscopic factors to various bound state parameters in the DWIA calculation is investigated. The recoil-momentum distribution of the cross section and the analyzing power with the different radii of the Woods-Saxon potential for the $1d_{3/2}$- and $2s_{1/2}$-hole states are displayed in Figs. 6.5 and 6.6. A change of the diffuseness parameter slightly modifies the distributions
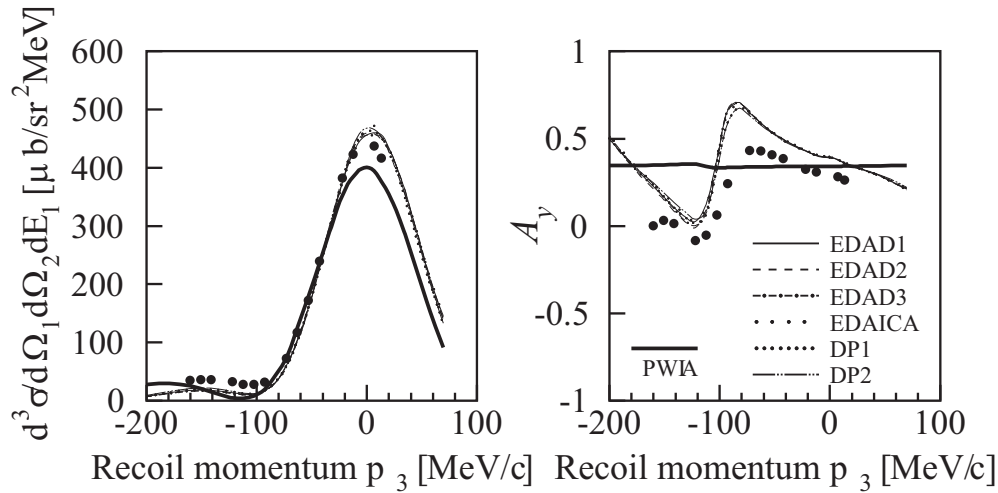
Figure 6.3: DWIA calculations of the ^{40}Ca$(p, 2p)$ reaction for the $2s_{1/2}$-hole state at 10.9 MeV with different optical potentials. The used optical potentials were same as those for the $1s_{3/2}$-hole state in Fig. 6.2. The strength of the $2s_{1/2}$-hole state was determined by the MDA for the peak. The only contribution of $2s_{1/2}$-hole state are displayed for simplicity. The thick solid line indicates the PWIA calculation.

of the cross section and the analyzing power. The relation between the obtained spectroscopic factors and the radius parameter is shown in Fig. 6.7. A change of 0.01 fm in the radius will change the spectroscopic factors by about 3, 2, and 5% for the $1d_{3/2}$-, $2s_{1/2}$-, and $1f_{7/2}$-hole states respectively, relative to the values with 1.30 fm by Elton and Swift. Next, the diffuseness parameter was changed within a range. The relation between the obtained spectroscopic factors and the diffuseness is shown in Fig. 6.8. A change of the diffuseness parameter doesn't modify distributions of the cross section and the analyzing power so much as the radius does, and the change of 0.01 fm in the diffuseness parameter will change the spectroscopic factors by about 1% for all of the $1d_{3/2}$-, $2s_{1/2}$-, and $1f_{7/2}$-hole states relative to the values with 0.60 fm by Elton and Swift. The strength of the spin–orbit term in the optical potential also influences on the spectroscopic factors as shown in Fig. 6.9. The spectroscopic factor gradually changes about 2% by 1 MeV for the $1d_{3/2}$-hole state.

The nonlocality corrections also give sizable influence on the calculation. Although the present analysis shown in Chap. 5 doesn't includes the nonlocality corrections, some recent analyses of the knockout reactions take them into account, and Kramer *et al.* also uses it for their analyses of the $(e, e'p)$ and $(d, {}^3\mathrm{He})$ reactions. In order to investigate the influence of the nonlocality corrections on the spectroscopic factors, the DWIA calculation for the present work was performed with the nonlocality corrections with a nonlocality range of $\beta = 0.85$ fm by Perey and Buck [91] in the bound state wave function and in the reaction. Using the calculated cross sections for the MDA, the obtained spectroscopic factors were shown in Fig. 6.10 with the result obtained in the previous chapter. It is found in Fig. 6.10 that the nonlocality corrections almost uniformly decrease the spectroscopic factors for all of the orbitals though a couple of the spectroscopic factors are still larger than the shell-model limits of the $2J + 1$ values.
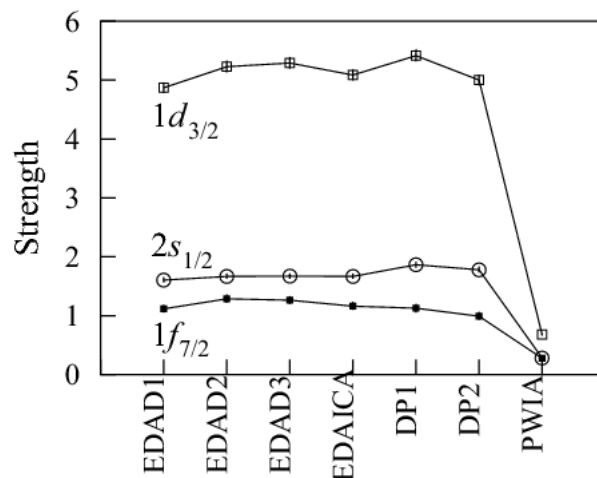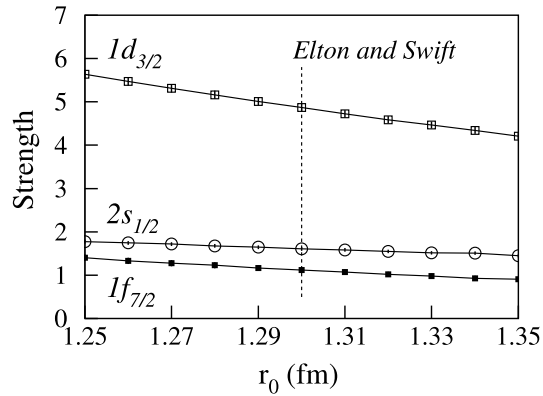
Figure 6.4: Spectroscopic factors obtained with the different distorting potentials for the $1d_{3/2}$-, $2s_{1/2}$-, and $1f_{7/2}$-hole states.

As seen in the previous paragraphs, the bound state parameters give some influence on the spectroscopic factors. The difference of the spectroscopic factors between from the present analysis and from the $(e, e'p)$ reaction by Kramer *et al.* in the reference [47] might be attributed to the difference in the bound state parameters used in the DWIA calculation. The bound-state parameters used by Kramer *et al.* are listed in Table 4.1. Kramer *et al.* performed their analysis with the same bound state wave function for the $(e, e'p)$ and $(d,^3\text{He})$ reactions and obtained consistent spectroscopic factors [47]. The parameters in Table 4.1 were determined by the analysis for the $(e, e'p)$ reaction on the grounds that the $(e, e'p)$ reaction is sensitive to the whole of the bound-state wave function. It should be noted that the radius and diffuseness parameters by Kramer *et al.* are optimized for each orbital although those values by Elton and Swift in Table 4.1, which are used in the present analysis, are same for all the orbitals in ^{40}Ca. The analysis by Kramer *et al.* includes the nonlocality corrections with a nonlocality range of $\beta = 0.85$ fm by Perey and Buck [91] in the bound state wave function and in the reaction. By using the same bound-state parameters with Kramer *et al.*, the cross sections for the $^{40}\text{Ca}(p, 2p)$ reaction are calculated and the spectroscopic factors of 3.23 for the $1d_{3/2}$ and 1.19 for the $2s_{1/2}$ are obtained. Even if the same bound-state parameters and the nonlocality-correction parameters are used for the $(p, 2p)$ and $(e, e'p)$ reactions, the spectroscopic factors from the $(p, 2p)$ reaction are still larger than those from the $(e, e'p)$ reaction by 20% or more. The differences of the spectroscopic factors from the $(p, 2p)$ in the present analysis and the previous result by Kramer *et al.* are not explained by the bound-state parameters only. Therefore, other problems still remain in the DWIA calculation.

It should be noted that the spectroscopic factors from the $(p, 2p)$ reaction are not settled even at the proton-injection energy of 200 MeV, where many $(p, 2p)$ experiments have vigorously been performed [40, 44, 79, 80]. It is seen in Table 5.1 that the spectroscopic factors for the valence orbitals in ^{40}Ca change by a factor of about 2 at the different measured angles.
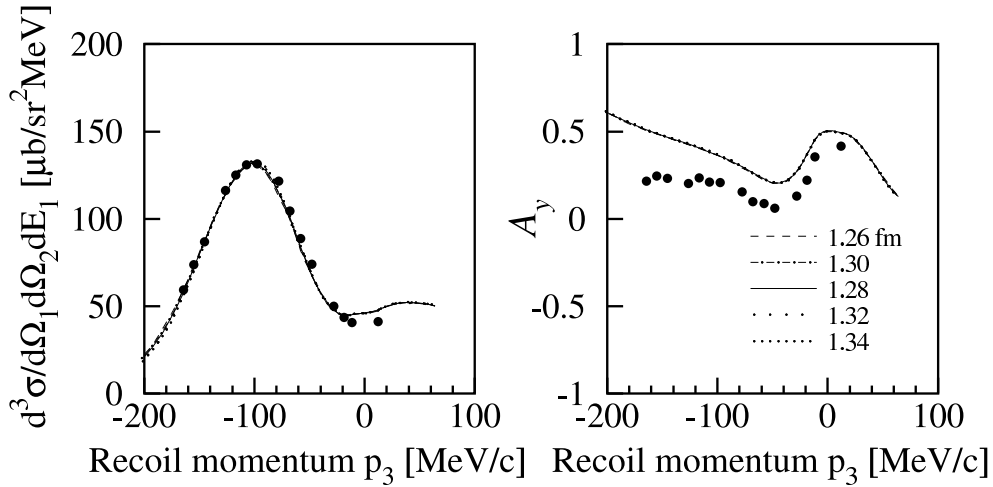
Figure 6.5: DWIA calculations of the ^{40}Ca$(p, 2p)$ reaction for the $1d_{3/2}$-hole state with the different radius parameters of the Woods-Saxon potential. The strengths of the $1d_{3/2}$-hole state were obtained by fitting to the experimental data.

Table 6.2: Normalized spectroscopic factors relative to the IPSM limits for the orbitals in ^{40}Ca. The description of the uncertainty is same as Table 5.3 except that these total uncertainties include also the uncertainty of the normalization.

		Spectroscopic factor	
	IPSM limit		with nonlocality correction
$1d_{3/2}$	4	$0.65 \pm 0.05(\pm0.01)$	$0.65 \pm 0.05(\pm0.01)$
$1f_{7/2}$	8	$0.074 \pm 0.007(\pm0.004)$	$0.069 \pm 0.007(\pm0.04)$
$2s_{1/2}$	2	$0.53 \pm 0.04(\pm0.01)$	$0.53 \pm 0.04(\pm0.01)$
$1d_{5/2}$	6	$0.85 \pm 0.09(\pm0.06)$	$0.83 \pm 0.09(\pm0.05)$
$1p$	6	$0.49 \pm 0.07(\pm0.06)$	$0.49 \pm 0.07(\pm0.06)$
$1s_{1/2}$	2	$0.89 \pm 0.09(\pm0.06)$	$0.95 \pm 0.11(\pm0.07)$

The aim of this work is to investigate the spectroscopic factors for the deeply bound orbitals. In order to discuss them in spite of the unsolved problems of the DWIA calculation, the spectroscopic factors were normalized by using the value from the $(e, e'p)$ reaction. Since there was no way to optimize bound-state parameters for the overlapped deeply bound orbitals, the common bound state parameters by Elton and Swift were used. As the hole state of the $1d_{3/2}$ orbital is well separated from the other orbital contributions in the separation energy spectra, the spectroscopic factor of the $1d_{3/2}$ orbital was used as the normalization reference. The ratio of the spectroscopic factor for the $1d_{3/2}$ orbital from the $(e, e'p)$ reaction by Kramer *et al.* to that obtained from the present analysis was 0.53. Thus, the deduced spectroscopic factors are normalized by the factor of 0.53 as listed in Table 6.2. The uncertainty of 8% from the normalization is added in quadrature for the total uncertainty.
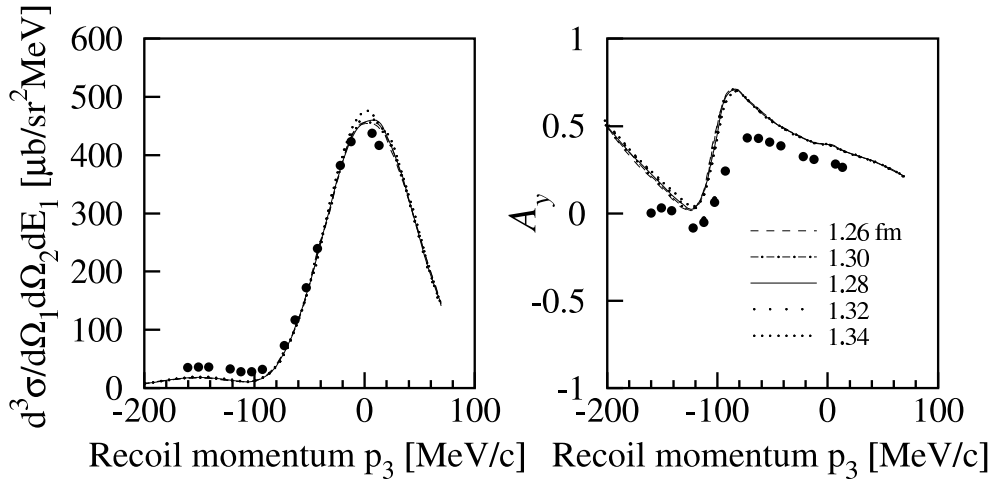
Figure 6.6: DWIA calculations of the ^{40}Ca$(p, 2p)$ reaction for the $2s_{1/2}$-hole state with the different radius parameters of the Woods-Saxon potential. The strength of the $2s_{1/2}$-hole state was determined by the MDA for the peak. The only contribution of $2s_{1/2}$-hole state are displayed for simplicity.

6.3 Spectroscopic factors

6.3.1 Comparison with experimental works

The spectroscopic factors from the present analysis are compared with those obtained from the previous $(e, e'p)$ experiments in Table 6.3, and they are illustrated as a function of the separation energy in Fig. 6.11. They are shown as ratios to the IPSM limits. The experimental uncertainties are not given for the spectroscopic factors obtained by Mougey *et al.* [16].

The spectroscopic factors obtained from the $(e, e'p)$ experiment by Nakamura *et al.* are larger than the sum-rule limits except for the $1d_{5/2}$ orbital [18]. Their large spectroscopic factors for the $1p$ and $1s_{1/2}$ orbitals suggest the underestimation of the cross section in the calculation or the inclusion of the continuum background in the higher-separation-energy region.

The spectroscopic factors of 0.65 and 0.75 obtained by Mougey *et al.* [16] for the $2s_{1/2}$ and $1s_{1/2}$ orbitals are as low as the present results of 0.53 and 0.89, whereas the spectroscopic factor of 0.95 for the $1p$ orbital is much larger than the present result of 0.49. The centroid energy of 41 MeV obtained by Mougey *et al.* for the $1p$ orbital is much higher than the present result of 29.6 MeV as seen in Fig. 6.1. As can be seen in Fig. 6.1, both the centroid energies of the $1p$ and $1s$ orbitals by Mougey *et al.* are higher than those from the present result. The larger spectroscopic factor and the higher centroid energy for the $1p$ orbital can be explained by inclusion of the continuum background in the $1p$-hole strengths in the higher-separation-energy region or by an insufficient separation of the $1p$- and $1s$-hole states. It is also plausible that the extremely high centroid energy of 77 MeV for the $1s_{1/2}$-hole state reported by Amaldi *et al.* [19] is due to the continuum background at higher separation energy.

Figure 6.7: Spectroscopic factors obtained with the different radius parameters of the Woods-Saxon potential for the $1d_{3/2}$-, $2s_{1/2}$- and $1f_{7/2}$-hole states.
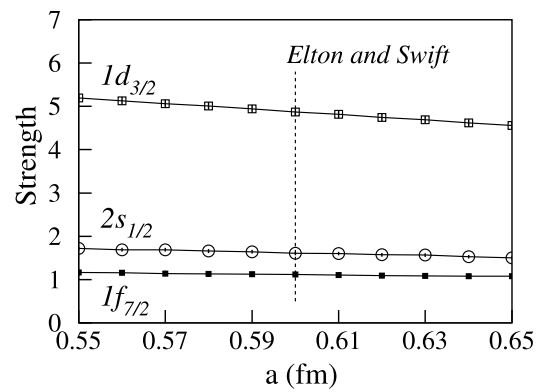
Figure 6.8: Spectroscopic factors obtained with the different diffuseness parameters of the Woods-Saxon potential for the $1d_{3/2}$-, $2s_{1/2}$-, and $1f_{7/2}$-hole states.

The present analysis also depends on the background treatment. The spectroscopic factors obtained without background subtraction for the $1s_{1/2}$, $1p$, and $1d_{5/2}$ orbitals are 1.5–2.0 times larger than those with backgrounds subtraction, as seen in Tables 5.3 and 5.4. This indicates that the spectroscopic factors are greatly affected by the background estimation.

The background from the four-body final states in the high-missing-energy region in the ^{12}C$(e, e'p)$ reaction was investigated by Fissum *et al.* at JLab [92]. The measured separation-energy spectra were compared with calculation of the $(e, e'pp)$ and $(e, e'pn)$ reactions included meson-exchange currents, isobar currents, central short-range correlations, and tensor medium-range correlations. However, the calculated cross section was smaller than the measured cross section by about 50% and did not clarify the total background components.

The contribution of the rescattering processes was studied by Cowley *et al.* [87]. It is remarkable that the calculated rescattering processes well reproduced the experimental coincidence spectra especially in the kinematical region in which the quasi-free events were hardly expected. The rescattering process cannot be ignored in some kinematical regions in the coincidence measurement.

Although the background components are still controversial, in the present study, we used the four-body phase space as the background-shape model, taking account of the four-body and rescattering processes. To compensate the inadequacy of the model, the uncertainties in the deduced observables were estimated to include the model uncertainties, as previously mentioned.

A large reduction in the single-particle strength has also been observed for the strongly bound valence neutrons near the Fermi surface in proton-rich unstable nuclei [93, 94]. This reduction has been suggested to be due to the strong p–n interactions [95]. Although the nucleons in the $1p$ and $1s_{1/2}$ orbitals in ^{40}Ca are also strongly bound, these orbitals are far below the Fermi surface. Therefore, the mechanisms for reducing the spectroscopic factors for the $1p$ and $1s_{1/2}$ orbitals in ^{40}Ca are expected to be different. We need further experimental study on the spectroscopic factors in other nuclei to clarify the
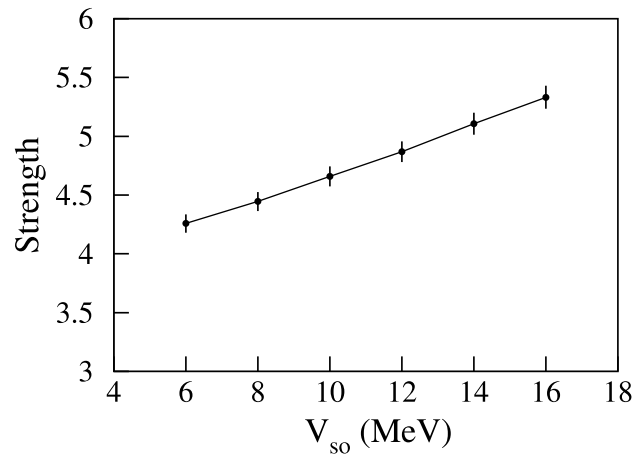
Figure 6.9: Correlation between the spectroscopic factors for the $1d_{3/2}$-hole state and the strength of the spin–orbit term for the bound state.

NN correlations that contribute to the reduction of the spectroscopic factors for deeply bound orbitals.

6.3.2   Comparison with theoretical works

The spectroscopic factors from the present result are compared with those from theoretical studies in Table 6.4, and they are illustrated as a function of the separation energy in Fig. 6.12. They are shown as ratios to the IPSM limits.

The calculations reported by Fabrocini *et al.* [13] and by Bisconti *et al.* [14] used state dependent correlations with central and tensor components, so-called f_6 correlation. Fabrocini *et al.* ignored the Coulomb interaction in the mean-field potential and used the *ls* coupling scheme of the single-particle wave function basis. Bisconti *et al.* followed the calculation in Ref. [13] by Fabrocini *et al.*, and considered the presence of the antiparallel spin terms and distinguished between proton and neutron contributions in the *jj* coupling scheme for sake of completeness. Both calculations suggested that the spectroscopic factor decreases as the binding energy increases, as can be seen in Fig. 6.12. This is contrary to the prediction by the nuclear matter calculation by Benhar *et al.*[12]. Furthermore, Bisconti *et al.* insisted from the results of ^{12}C, ^{16}O, ^{40}Ca, ^{48}Ca, and ^{208}Pb that the spectroscopic factors increase when the principle quantum number *n* and the *lj* values increase. Although the values predicted by Bisconti *et al.* show a rather moderate reduction, the quantitative difference between these calculations was not discussed. The role played by the various correlations have been unclear.

The spectroscopic factors of 0.86 and 0.87 for the $2s_{1/2}$ orbital predicted by Fabrocini *et al.* [13] and Bisconti *et al.* [14] considerably exceed the present result of 0.53. This discrepancy could be explained by surface effects, which are not taken into account in their calculations. It is theoretically known that the surface effects reduce the spectroscopic factors for the orbitals near the Fermi level.

Though the spectroscopic factor of 0.85 for the $1d_{5/2}$ orbital is consistent with the values predicted
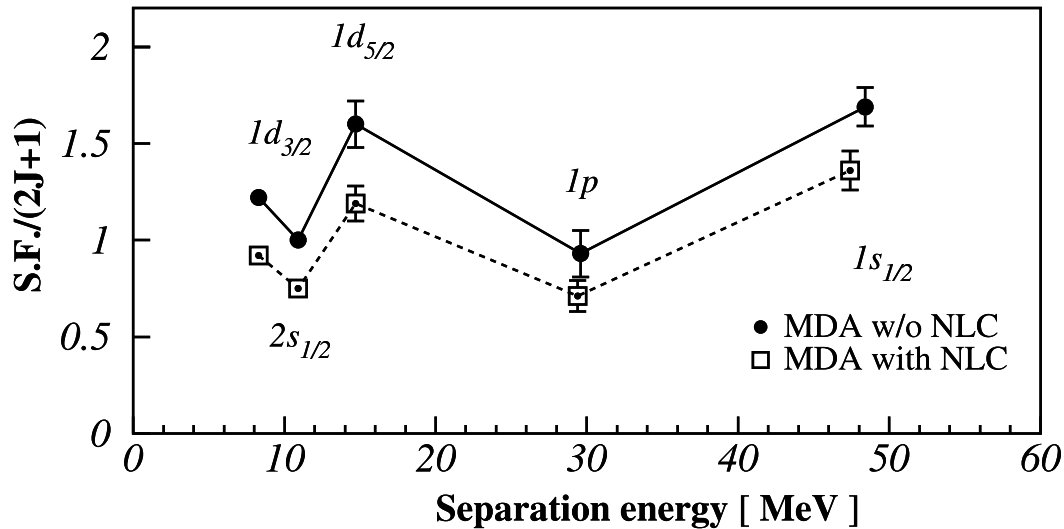
Figure 6.10: Spectroscopic factors relative to the IPSM limits for the orbitals in ^{40}Ca as a function of the separation energy. The solid line and dashed line are shown to guide the eyes. The strengths shown by the squares are obtained by the MDA with the DWIA calculation including the nonlocality correction in the bound state wave function and in the reaction. The nonlocality corrections almost uniformly decrease the spectroscopic factors for all of the orbitals.

by Fabrocini *et al.* and by Bisconti *et al.*, those for the $1s_{1/2}$ and $1p$ orbitals show a different tendency from the predictions. The spectroscopic factor of 0.89 for the $1s_{1/2}$ orbital is slightly smaller than unity, but the reduction of the spectroscopic factor is not significant because the experimental uncertainty is as large as 0.09. On the other hand, the spectroscopic factor of 0.49 for the $1p$ orbital is largely suppressed and is smaller than the predicted value of 0.58 by Fabrocini *et al.* The large reduction of the spectroscopic factor for the $1p$ orbital indicates a strong influence of *NN* correlations in the inner core far below the Fermi surface.

The spectroscopic factors for the $1d_{5/2}$, $1p$ and $1s_{1/2}$ don't show monotonous decrease or increase with respect to binding energy as predicted. The present result possibly suggests other dependence of the *NN* correlations, *e.g.*, l dependence, and a clue to disentangle the role played by the correlations. Therefore, it is interesting to investigate the spectroscopic factor for the $1p$ orbital in detail. The spectroscopic factor for the $1p$ orbital was obtained on the assumption that the relative strengths for the $1p_{1/2}$ and $1p_{3/2}$-hole states are in the ratio of 2:4. It is important to deduce the spectroscopic factors for the $1p_{1/2}$ and $1p_{3/2}$-hole states separately to obtain further information on the reduction of the spectroscopic factor for the deeply bound orbitals.

6.4   Perspectives

The $1p_{1/2}$- and $1p_{3/2}$-hole states could not be separated in the present study because the DWIA calculation of the analyzing power was not fully reliable. It is important to separate the hole states of the $1p_{1/2}$

Table 6.3: Spectroscopic factors relative to the IPSM limits for the orbitals in ^{40}Ca obtained from previous experiments. For the present result, the description of the uncertainty is same as Table 6.2.

	IPSM limit	Present work	Mougey *et al.* [16] [a]	Nakamura *et al.*[18] [b]
$2s_{1/2}$	2	0.53 ± 0.04(±0.01)	0.65	1.0 ± 0.1
$1d$	10		0.77	
$1d_{3/2}$	4	0.65 ± 0.05(±0.01)		1.1 ± 0.4
$1d_{5/2}$	6	0.85 ± 0.09(±0.06)		0.78 ± 0.27
$1p$	6	0.49 ± 0.07(±0.06)	0.95	1.70 ± 0.15
$1s_{1/2}$	2	0.89 ± 0.09(±0.06)	0.75	2.60 ± 0.15 (A)
				1.9 ± 0.1 (B)

[a]The uncertainties were not given for the spectroscopic factors by Mougey *et al.*.

[b]Two results ((A) and (B)) were presented for $1s_{1/2}$ orbital.

Table 6.4: Spectroscopic factors relative to the IPSM limits for the orbitals in ^{40}Ca obtained from theoretical studies. For the present result, the description of the uncertainty is same as Table 6.2.

	IPSM limit	Present work	Fabrocini *et al.* [13]	Bisconti *et al.* [14]
$2s_{1/2}$	2	0.53 ± 0.04(±0.01)	0.86	0.87
$1d$	10		0.87	
$1d_{3/2}$	4	0.65 ± 0.05(±0.01)		0.85
$1d_{5/2}$	6	0.85 ± 0.09(±0.06)		0.86
$1p$	6	0.49 ± 0.07(±0.06)	0.58	
$1p_{1/2}$	2			0.81
$1p_{3/2}$	4			0.82
$1s_{1/2}$	2	0.89 ± 0.09(±0.06)	0.55	0.78

and $1p_{3/2}$ orbitals, that is, the hole states of the $j_>$ and $j_<$ orbitals, by use of the analyzing power data, to obtain further information on the deeply bound orbitals and to understand NN correlations in atomic nuclei. Therefore, progress in the reaction theory is strongly desired because it enables us to use the analyzing power data in the MDA.

Following the present work, another $(p, 2p)$ experiment with a polarized proton beam was done at 200 MeV [96] at RCNP. The analyzing power data was reproduced by the DWIA calculation better than that in the present work, and it encourages us to separate the hole states of the $j_>$ and $j_<$ orbitals. Since that measurement was performed under the symmetric angle condition for ejected protons, the symmetric angle condition seems to be advantageous to the analyzing power measurement. Understanding why the DWIA calculation reproduced the analyzing power data in the lower injection-energy experiment remains to be done. Although background contribution might interfere the analyzing power for deeply bound orbitals, the analyzing power measurement at 200 MeV under the symmetric angle condition
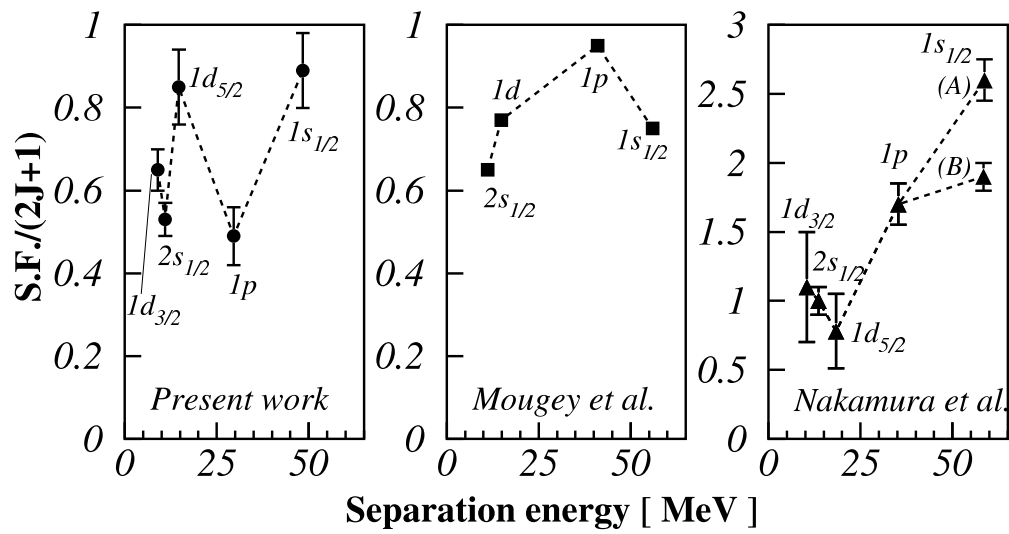
Figure 6.11: Spectroscopic factors relative to the IPSM limits for the orbitals in ^{40}Ca as a function of the separation energy. The dashed lines are shown to guide the eyes.

might be useful to separate the $1p_{1/2}$- and $1p_{3/2}$-hole states.

　　We also need a systematic measurement of the spectroscopic factors for the orbitals far below the Fermi surface in various nuclei. It should be highly helpful for us to clarify the *NN* correlation in the atomic nuclei.
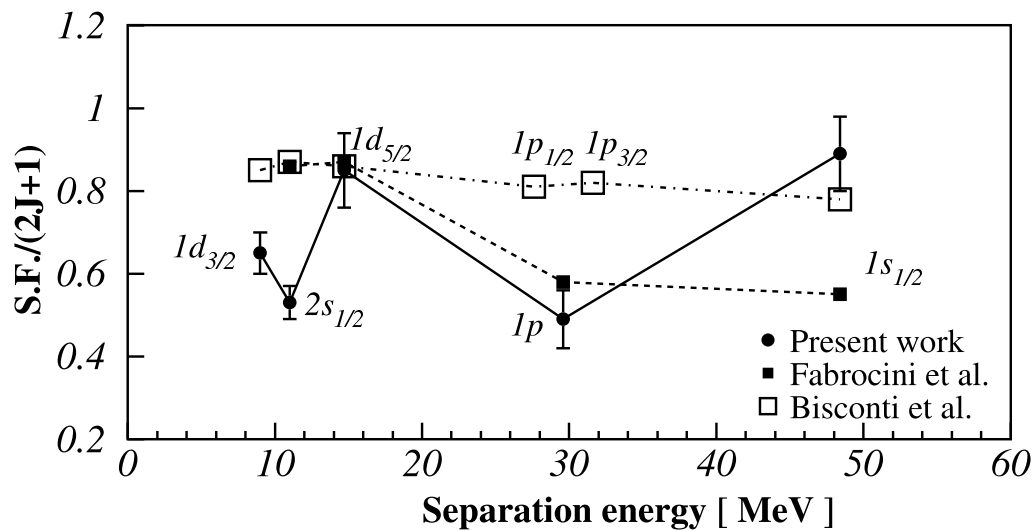
Figure 6.12: Spectroscopic factors relative to the IPSM limits for the orbitals in ^{40}Ca as a function of the separation energy with the predictions by Fabrocini *et al.* [13] and Bisconti *et al.* [14]. For the separation energies of the predictions, the values of the present result are used since no predicted values are given in their papers. The separation energies for the $1p_{1/2}$ and $1p_{3/2}$ orbitals are plotted deviating ± 2 MeV from 29.6 MeV respectively. The solid line (present result), dashed line (Fabrocini *et al.*), and dash-dotted line (Bisconti *et al.*) are shown to guide the eyes.

Chapter 7

Summary

A $^{40}\text{Ca}(\vec{p}, 2p)$ experiment was performed with a 392-MeV polarized proton beam to measure the recoil-momentum distributions of the cross section and the analyzing power in the separation-energy region of 0–89 MeV.

Although a hump structure is seen around 30 MeV in the measured separation energy spectra, no peak or hump cannot be seen above 40 MeV, where $1s$-hole state is expected to be seen.

Two prominent peaks were observed at 8.3 and 10.9 MeV in the separation energy spectra, and their recoil-momentum distributions of the cross section show characteristic behavior for a hole state of a single-particle orbital with $L \neq 0$ and $L = 0$, respectively. The DWIA calculation reproduces the dependence of the recoil momentum on the measured cross section qualitatively well. This assured the validity of the MDA with the cross-section data. Although the DWIA calculation reproduces the dependence of the recoil momentum on the measured analyzing power qualitatively, it systematically overestimates the analyzing power for $1d_{3/2}$ and $2s_{1/2}$-hole states. The obtained spectroscopic factors for the $1d_{3/2}$ and $2s_{1/2}$ are larger than those from the $(e, e'p)$ and $(d,^{3}\text{He})$ reactions. The differences of the spectroscopic factors for the low-lying orbitals between from the $(p, 2p)$ in the present work and from the $(e, e'p)$ reactions are due not only to the bound-state parameters but also to the treatment of the distortion in the $(p, 2p)$ reaction. It is found that there are some uncertainties in the absolute values of the cross section and the analyzing power from the DWIA calculation under the present experimental condition.

The strength distributions for the deep-hole states were obtained by the MDA for each 2-MeV bin in the separation energy without any assumption on the shape of the distribution and were successfully separated from the continuum background by subtraction of a four-body background. The centroid energies and widths of the distributions were deduced to be 29.6 ± 0.5 and 48.4 ± 0.6 MeV for the $1p$ and $1s_{1/2}$-hole states, respectively. The hump of the $1p$-hole state around 30 MeV is consistent with the hump structure in the separation energy spectra.

Taking the uncertainty of the DWIA calculation into the consideration, the spectroscopic factors were normalized by using the value for the $1d_{3/2}$ orbital from the $(e, e'p)$ reaction and discussed. The

normalized spectroscopic factors for the $1p$ and $1s_{1/2}$ orbitals were obtained as $49 \pm 7\%$ and $89 \pm 9\%$ of the IPSM limits, respectively. Although the small quenching for the $1s_{1/2}$ orbital doesn't give a decisive evidence of the influence of the NN correlations, the large quenching for the $1p$ orbital suggests that the spectroscopic factor for the orbital in the inner core is reduced owing to the NN correlations. Further development of the DWIA calculation of the analyzing power is needed to separate the hole states of the $1p_{1/2}$ and $1p_{3/2}$ orbitals and clarify the influence of the NN correlations on the spectroscopic factors.

Acknowledgements

I would like to express my gratitude to Professor H. Sakaguchi, who was my supervisor at the graduate course in Kyoto University. He suggested the study of deep hole states in the medium-mass region by $(p, 2p)$ reaction and have patiently been discussed the subject on physics with me. I have continuously learned experimental technique from him.

I would like to thank Professor T. Kawabata for his helpful discussion and guidance on the present work. I appreciate his critical advice on a draft of a paper.

I acknowledge Professor M. Yosoi, who is kind enough to provide his analysis software and to give the detail of making the MWPCs. As he is one of the experimentalists who have a detailed knowledge of an experiment with the Grand Raiden spectrometer, I have gotten lots of advices from him not only in the experiments but also in the analysis of the data.

I am deeply grateful to Professor T. Noro, from whom I have learned much of $(p, 2p)$ experiment. He gave me chances to join the experiments at the Petersburg Nuclear Physics Institute (PNPI), Gatchina, Russia. We started the study of deep hole states by $(p, 2p)$ reaction since these experiments.

I would like to thank Professor T. Nagae for his thoughtful suggestions for this thesis.

I gratefully thank the scientific and technical staff and cyclotron crew at RCNP, especially Professor K. Hatanaka and Dr. S. Ninomiya, for their support for providing a stable beam during the experiment and for the beam-time management.

I would address my thank to Dr. H. Takeda, who had developed the RDTM module and supported its operation during the beamtime. I am grateful to Dr. M. Itoh for his hard work in the preparation and in the beamtime. I am thankful to Dr. M. Uchida and Dr. H. P. Yoshida for their great contribution to the experiment, especially to the data acquisition. I wish to thank Dr. S. Terashima, Mr. S. Kishi, and Dr. J. Zenihiro, who worked in whole of the experiment and took much of midnight shifts.

I would like to thank Professor T. Wakasa for his support and advices on a draft of a paper.

I would like to thank all other members of the RCNP-E168/217 experiments; Mr. S. Asaji, Dr. K. Fujita, Mr. Y. Hagihara, Dr. T. Ishida, Professor Y. Sakemi, Dr. Y. Shimizu, Dr. Y. Tameshige, and Mr. T. Yonemura for their great contributions.

Appendix A

Revised result

We had already published the result of this work in Ref. [97] in 2010. After the publication, a mistake in the estimation of the cross section was found during the preparation of this thesis. The results in this thesis were obtained after correcting the mistake and improving the inadequate estimation of the MWPC efficiency. The revised result in this thesis is compared with the published result in Ref. [97] in Tables A.1 –A.4. The errata based on the revised result will be published.

In the reanalysis, at first, the spectroscopic factors were evaluated in the same way as that in Ref. [97], which are listed as "Raw" in Tables A.1, A.3, and A.4. However, the obtained spectroscopic factors are considerably larger than the published values, and some of them exceed 100% of the $2J+1$ value. It was concluded that there are some uncertainties in the absolute values of the cross section from the DWIA calculation under the present experimental condition. Taking the uncertainty of the DWIA calculation into the consideration, the spectroscopic factors were normalized by using the value for the $1d_{3/2}$ orbital from the $(e,e'p)$ reaction by Kramer *et al.* in Ref. [47], which are listed as "Normalized" in Tables A.1, A.3, and A.4.

Table A.1: Spectroscopic factors for the discrete peaks in the ^{40}Ca measurement. The first uncertainty is the total uncertainty and the second, in parentheses, is the statistical uncertainty included in the total. In the published results, the uncertainty from the DWIA calculation is included in the total uncertainty. In the reanalyzed results, the uncertainty from the normalization reference [47] is included in the total uncertainty of the normalized results.

E_{sep} [MeV]	Orbital	Spectroscopic factor		
		Published [97]	Reanalyzed	
			Raw	Normalized
8.3	$1d_{3/2}$	$3.12 \pm 0.53 (\pm 0.06)$	$4.87 \pm 0.09 (\pm 0.09)$	$2.58 \pm 0.20 (\pm 0.05)$
10.9	$2s_{1/2}$	$1.01 \pm 0.17 (\pm 0.03)$	$1.61 \pm 0.04 (\pm 0.04)$	$0.85 \pm 0.07 (\pm 0.02)$
10.9	$1f_{7/2}$	$0.78 \pm 0.14 (\pm 0.04)$	$1.12 \pm 0.06 (\pm 0.06)$	$0.59 \pm 0.06 (\pm 0.03)$

Table A.2: Centroid energies and widths (FWHM) of the strength distributions for the hole states of the $1p$ and $1s_{1/2}$ orbitals in ^{40}Ca. The first uncertainty is the total uncertainty, which includes the statistical and the model uncertainties, and the second, in parentheses, is the statistical uncertainty included in the total.

| Orbital | Published [97] | | Reanalyzed | |
| | Centroid | Width | Centroid | Width |
	(MeV)	(MeV)	(MeV)	(MeV)
$1p$	$30.0 \pm 0.4(\pm 0.3)$	$10.3 \pm 1.1(\pm 0.9)$	$29.6 \pm 0.5(\pm 0.5)$	$11.4 \pm 1.2(\pm 1.2)$
$1s_{1/2}$	$49.6 \pm 0.6(\pm 0.6)$	$21.3 \pm 0.9(\pm 0.9)$	$48.4 \pm 0.6(\pm 0.6)$	$23.4 \pm 1.1(\pm 1.1)$

Table A.3: Spectroscopic factors relative to the IPSM limits for the orbitals in ^{40}Ca. They are obtained after subtraction of the background. The first uncertainty is the total uncertainty and the second, in parentheses, is the statistical uncertainty included in the total. The model uncertainty is included in the total uncertainty. The uncertainty from the DWIA calculation are included in the total uncertainty of the published results, while the uncertainty from the normalization reference [47] is included in the total uncertainty of the normalized results.

| Orbital | IPSM limit | Spectroscopic factor | | |
| | | Published [97] | Reanalyzed | |
			Raw	Normalized
$1d_{3/2}$	4	$0.78 \pm 0.13(\pm 0.01)$	$1.22 \pm 0.02(\pm 0.02)$	$0.65 \pm 0.05(\pm 0.01)$
$1f_{7/2}$	8	$0.097 \pm 0.017(\pm 0.005)$	$0.14 \pm 0.01(\pm 0.01)$	$0.074 \pm 0.007(\pm 0.004)$
$2s_{1/2}$	2	$0.60 \pm 0.10(\pm 0.02)$	$1.00 \pm 0.03(\pm 0.03)$	$0.53 \pm 0.04(\pm 0.01)$
$1d_{5/2}$	6	$0.94 \pm 0.17(\pm 0.06)$	$1.60 \pm 0.12(\pm 0.11)$	$0.85 \pm 0.09(\pm 0.06)$
$1p$	6	$0.49 \pm 0.10(\pm 0.06)$	$0.93 \pm 0.12(\pm 0.12)$	$0.49 \pm 0.07(\pm 0.06)$
$1s_{1/2}$	2	$0.78 \pm 0.14(\pm 0.05)$	$1.69 \pm 0.10(\pm 0.10)$	$0.89 \pm 0.09(\pm 0.06)$

Table A.4: Spectroscopic factors relative to the IPSM limits for the orbitals in ^{40}Ca without background subtraction. The first uncertainty is the total uncertainty and the second, in parentheses, is the statistical uncertainty included in the total. The uncertainty from the DWIA calculation are included in the total uncertainty of the published results, while the uncertainty from the normalization reference [47] is included in the total uncertainty of the normalized results.

| Orbital | IPSM limit | Spectroscopic factor | | |
| | | Published [97] | Reanalyzed | |
			Raw	Normalized
$2s_{1/2}$	2	$0.61 \pm 0.11(\pm 0.02)$	$1.02 \pm 0.03(\pm 0.03)$	$0.54 \pm 0.04(\pm 0.01)$
$1d_{5/2}$	6	$1.33 \pm 0.23(\pm 0.05)$	$2.23 \pm 0.11(\pm 0.11)$	$1.18 \pm 0.11(\pm 0.06)$
$1p$	6	$1.41 \pm 0.24(\pm 0.04)$	$1.87 \pm 0.07(\pm 0.07)$	$0.99 \pm 0.08(\pm 0.04)$
$1s_{1/2}$	2	$1.12 \pm 0.19(\pm 0.03)$	$2.53 \pm 0.05(\pm 0.05)$	$1.34 \pm 0.11(\pm 0.03)$

Appendix B

Scattering angles and recoil momentum

B.1 Scattering angle

Scattering angles for the emitted protons from the target were obtained with the MWPCs in front of the spectrometers and with the VDCs at the focal planes. Angular resolution by the MWPC was determined by the wire spacing, a beam-spot size at the target, and the distance between the target and the anode plane. It is estimated at approximately 0.11°, as mentioned in Sec. 3.5.

Horizontal angular resolutions by the MWDC were evaluated by using pp scattering event for reference. The event of pp scattering was measured at 25.5° for the GR and at 60.0° for the LAS. For pp scattering, the measured kinetic energy and horizontal scattering angle of the emitted proton strongly correlate to each other, and they are one-to-one correspondence in the laboratory system since pp scattering event is two body reaction and two particles are identical. Figure B.1 (A) shows two dimensional plot of the horizontal scattering angle (θ_{GR}) and the position at the focal plane (X_{GR}), which corresponds to the kinetic energy. The width of the locus line indicates the resolution of the scattering angle and the kinetic energy. The locus was corrected so that the kinetic-energy dependence of the horizontal scattering angle was canceled, as shown in Fig. B.1 (B). In $-50 \leq X_{GR} \leq 50$, the corrected angle (θ'_{GR}) was projected on the horizontal angle axis , which is shown in Fig. B.1 (C), and fitted with Gaussian function. The estimated angular resolution was 0.08° for the GR. It is smaller than that by the MWPC for the GR. The horizontal angular resolution by the MWDC for the LAS was also estimated in the same way as the GR case and was 0.23°. It is larger than that by the MWPC for the LAS. The worse angular resolution for the LAS is due to the low proton energy and thick film at the exit of the LAS spectrometer.

B.2 Recoil momentum

Recoil momentum ($\vec{p_3}$) of the residual nucleus in the $(p, 2p)$ reaction was calculated on the basis of the momentum conservation law as

$$\vec{p_3} = \vec{p_0} - \vec{p_1} - \vec{p_2} \tag{B.1}$$
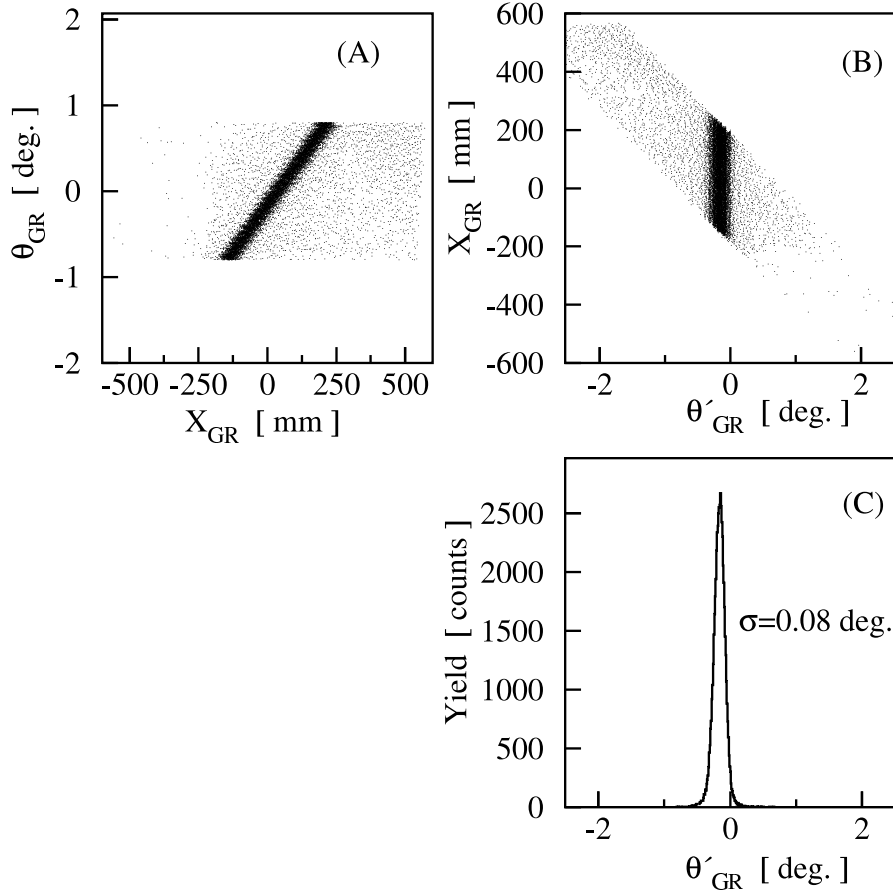
Figure B.1: (A) Two dimensional plot of the horizontal scattering angle (θ_{GR}) and the position at the focal plane (X_{GR}), which corresponds to the kinetic energy, for the GR. (B) Two dimensional plot of the horizontal scattering angle corrected so that the kinetic-energy dependence of the horizontal scattering angle was canceled (θ'_{GR}) and X_{GR}. (C) Corrected angle (θ'_{GR}) projected on the horizontal angle axis in $-50 \leq X_{GR} \leq 50$.

where $\vec{p_i}$ ($i = 0, 1, 2$) are the momentum of the incident proton ($i = 0$), the scattered and knocked-out protons ($i = 1, 2$), respectively. In pp scattering event, the recoil momentum doesn't exist since the residual particle doesn't exist. The momentum $\vec{p_3}$ calculated by Eq. B.1 should be zero for pp scattering event. It is useful to estimate $\vec{p_3}$ and the deviation from zero in pp scattering event for the accuracy of momentum reconstruction.

The information from the MWPCs was used for the vertical scattering angle for particles coming to the GR and the horizontal and vertical scattering angles for particles coming to the LAS. Here, in estimating the momentum $\vec{p_3}$ in pp scattering event, the scattering angles from the MWPCs were randomly deviated in the angular resolution by Monte Carlo technique for smoothing. The obtained result for $|\vec{p_3}|$ in pp scattering event is shown in Fig. B.2. The average deviation from μ defined by

$$\langle |x_i - \mu| \rangle = \int |x - \mu| f(x)\, dx \tag{B.2}$$
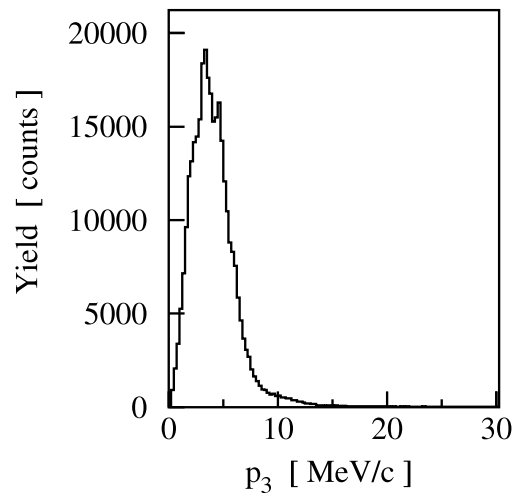
Figure B.2: Momentum $|p_3|$ estimated in pp scattering event. The scattering angles from the MWPCs were randomly deviated in the angular resolution by Monte Carlo technique for smoothing.

was estimated for $x = |\vec{p_3}|$, where $f(x)$ is a distribution function and $\mu=0$. The obtained average deviation was 4.4 MeV/c. If we didn't have any information on the vertical scattering angles and ignored them, that is, the vertical scattering angles were taken as zero, the average deviation would be 2.9 MeV/c and be a little underestimate.

Appendix C

Phase space calculation

C.1 Introduction

The $(p, 3p)$ and $(p, 2pn)$ reactions are possible components of the background in the $(p, 2p)$ reaction, while the dynamical aspects in the $(p, 3p)$ and $(p, 2pn)$ reactions are unclear. In order to estimate the contribution of those reactions in the $(p, 2p)$ reaction measurement without the dynamical details of the $(p, 3p)$ and $(p, 2pn)$ reactions, the phase space for the 4-particle final state was calculated. Phase space describes a kinematical aspect of the process. In this chapter, the four-body phase space is derived from its definition.

As the DWIA calculation in the present study employs the noninvariant form, the noninvariant phase space is employed here. The momentum p_j and energy E_j of the j-th particle satisfy the following relation

$$E_j^2 - p_j^2 = m_j^2,\tag{C.1}$$

where m_j is the mass of the j-th particle. As is defined in Werbrouck's textbook [98], the probability dP_n of a n-particle final state with a total momentum P and total energy E is defined as

$$d^{3n}P_n = d^{3n}\mathcal{R}_n\mathcal{H},\tag{C.2}$$

where $\mathcal{H}$ is the square of the noninvariant matrix element for the process and contains the dynamical aspects of the process, and $\mathcal{R}_n$ is pure kinematical and the Lorentz noninvariant phase space defined by

$$d^{3n}\mathcal{R}_n = \left\{\prod_{j=1}^{n} d^3p_j\right\}\delta^3\left(\sum_{j=1}^{n} p_j - P\right)\delta\left(\sum_{j=1}^{n} E_j - E\right).\tag{C.3}$$

C.2 Phase space for four-particle final state

The processes that we take account of are the $^{40}\text{Ca}(p, 3p)^{38}\text{Ar}$ and $^{40}\text{Ca}(p, 2pn)^{38}\text{K}$ reactions. As the final states have the configuration of $3p+^{38}\text{Ar}$ or of $2p + n+^{38}\text{K}$, respectively, the four-body phase space

$\mathcal{R}_4$ is discussed here. The calculation employs the condition that the two protons in the final states are detected by GR and LAS but the other particles in the final states are not detected, as is same as the experiment.

Let particles 1 and 2 correspond to protons detected by GR and LAS. The particles 3 and 4 are the combination of $p+^{38}$Ar or $n+^{38}$K. The phase space for the four-body final states is given from Eq. (C.3) as

$$d^{4\cdot3}\mathcal{R}_4 = \left\{ \prod_{j=1}^{4} d^3 p_j \right\} \delta^3 \left(\sum_{j=1}^{4} p_j - P \right) \delta \left(\sum_{j=1}^{4} E_j - E \right). \tag{C.4}$$

From Eq. (C.4), we have the four-body phase space in the integral form

$$
\begin{aligned}
\mathcal{R}_4(E, P) &= \int d^3 p_1 \, d^3 p_2 \, d^3 p_3 \, d^3 p_4 \delta^3 \left(p_1 + p_2 + p_3 + p_4 - P \right) \delta \left(E_1 + E_2 + E_3 + E_4 - E \right) \\
&= \int d^3 p_1 \, d^3 p_2 \int d^3 p_3 d^3 p_4 \delta^3 \left(p_3 + p_4 - P' \right) \delta \left(E_3 + E_4 - E' \right),
\end{aligned} \tag{C.5}
$$

where E' and P' are defined by $E' = E - E_1 - E_2$ and $P' = P - p_1 - p_2$, respectively. The last integral in Eq. (C.5) corresponds to the two-body phase space $\mathcal{R}_2(E', P')$ with total momentum P' and total energy E'.

$$\mathcal{R}_2(E', P') = \int d^3 p_3 d^3 p_4 \delta^3 \left(p_3 + p_4 - P' \right) \delta \left(E_3 + E_4 - E' \right) \tag{C.6}$$

Therefore, we have

$$\mathcal{R}_4(E, P) = \int d^3 p_1 \, d^3 p_2 \, \mathcal{R}_2(E', P'). \tag{C.7}$$

Under the condition that only two protons in the final states are detected, the state of the rest particles is indefinite. The 4-particle final states could contribute in the separation energy spectrum for the ^{40}Ca$(p, 2p)^{39}$K reaction. Excluded the reaction Q-value, the separation energy calculated from the energies of the injected and detected protons corresponds to the excitation energy of the residual nucleus in the 3-particle final states, while it corresponds to the effective mass of the particles 3 and 4 in the 4-particle final states. The effective mass M_{34} of the particles 3 and 4 is defined by

$$M_{34}^2 = (E_3 + E_4)^2 - (p_3 + p_4)^2. \tag{C.8}$$

In order to estimate the contribution of the 4 particle final states in the separation energy spectrum for the ^{40}Ca$(p, 2p)^{39}$K reaction, the mass distribution of the four-body phase space

$$\frac{d\mathcal{R}_4}{dM_{34}} \tag{C.9}$$

is needed. By using the conservation laws of momentum and energy, the effective mass M_{34} is expressed as

$$
\begin{aligned}
M_{34}^2 &= (E - E_1 - E_2)^2 - (P - p_1 - p_2)^2 \\
&= (M^2 + m_1^2 + m_2^2 - 2EE_1 + 2P \cdot p_1)^2 - 2EE_2 + 2E_1E_2 - 2P \cdot p_1 - 2p_1 \cdot p_2 . \tag{C.10}
\end{aligned}
$$

Let $p_j = |\boldsymbol{p}_j|$, and differentiating Eq. (C.10) with respect to p_2 gives

$$\frac{dM_{34}}{dp_2} = -\frac{1}{M_{34}}\left((E - E_1)\frac{p_2}{E_2} + P\cos\theta_2 - p_1\cos\theta_{12}\right). \tag{C.11}$$

The use of $\frac{dE_j}{dp_j} = \frac{p_j}{E_j}$ gives the other forms of $d^3\boldsymbol{p}_j$

$$d^3\boldsymbol{p}_j = p_j^2 dp_j d\Omega_j = p_j E_j dE_j d\Omega_j. \tag{C.12}$$

Combining Eq. (C.7), Eq. (C.11), and Eq. (C.12) yields

$$\begin{aligned}
\mathcal{R}_4(E, \boldsymbol{P}) &= \int p_1 E_1 dE_1 d\Omega_1 p_2^2 dp_2 d\Omega_2 \, \mathcal{R}_2(E', \boldsymbol{P'}) \\
&= \int p_1 E_1 dE_1 d\Omega_1 p_2^2 d\Omega_2 \, dM_{34} \left|\frac{dp_2}{dM_{34}}\right| \mathcal{R}_2(E', \boldsymbol{P'}).
\end{aligned} \tag{C.13}$$

Therefore, Eq. (C.9) is obtained as

$$\frac{d\mathcal{R}_4}{dM_{34}} = \int dE_1 d\Omega_1 d\Omega_2 \, p_1 E_1 p_2^2 \left|\frac{dp_2}{dM_{34}}\right| \mathcal{R}_2(E', \boldsymbol{P'}). \tag{C.14}$$

The phase space for the four-body final state is calculated under the condition that two protons from a final state are detected by the GR and LAS. Therefore, the parameters of particle 1 and 2 are given by the measurement condition. The integral range of these parameters are determined by the acceptances of the GR and LAS.

C.3 Phase space for two-particle final state

When the parameters of the particles 1 and 2 are given, the energy E' and momentum $\boldsymbol{P}$' of the rest two-body system are determined.

At the integration of Eq. (C.6) over $\boldsymbol{p_4}$, the integration rules for a δ-function gives

$$\begin{aligned}
\mathcal{R}_2(E', \boldsymbol{P'}) &= \int d^3\boldsymbol{p}_3 \, d^3\boldsymbol{p}_4 \delta^3(\boldsymbol{p}_3 + \boldsymbol{p}_4 - \boldsymbol{P'})\delta(E_3 + E_4 - E') \\
&= \int d^3\boldsymbol{p}_3 \left[\psi(\boldsymbol{p_4})\left|\frac{\partial A}{\partial\boldsymbol{p_4}}\right|^{-1}\right]_{\boldsymbol{p_4}=\boldsymbol{p_4}^*},
\end{aligned} \tag{C.15}$$

where $A = \boldsymbol{p_4} - (\boldsymbol{P'} - \boldsymbol{p}_3)$. Since the solution $\boldsymbol{p_4}^*$ of $A = 0$ is $\boldsymbol{p_4}^* = (\boldsymbol{P'} - \boldsymbol{p}_3)$ and $\frac{\partial A}{\partial\boldsymbol{p_4}} = 1$,

$$\mathcal{R}_2(E', \boldsymbol{P'}) = \int d^3\boldsymbol{p}_3 \, \delta\left(\sqrt{p_3^2 + m_3^2} + \sqrt{(\boldsymbol{P'} - \boldsymbol{p}_3)^2 + m_4^2} - E'\right).$$

The following integration over $\boldsymbol{p_3}$ yields

$$\mathcal{R}_2(E', \boldsymbol{P'}) \;=\; \int d\Omega_3 \int p_3^2 dp_3 \; \delta\left(\sqrt{p_3^2 + m_3^2} + \sqrt{(\boldsymbol{P'} - \boldsymbol{p}_3)^2 + m_4^2} - E' \right)$$

$$\;=\; \int d\Omega_3 \left[p_3^2 \left| \frac{\partial B}{\partial p_3} \right|^{-1} \right]_{p_3 = p_3^*} \tag{C.16}$$

where $B = \sqrt{p_3^2 + m_3^2} + \sqrt{(\boldsymbol{P'} - \boldsymbol{p}_3^2)^2 + m_4^2} - E'$ and $\boldsymbol{p_3}^*$ is the solution of $B = 0$.

Since

$$\frac{\partial B}{\partial p_3} \;=\; \frac{p_3}{\sqrt{p_3^2 + m_3^2}} + \frac{p_3 - P' \cos\theta_3}{\sqrt{(\boldsymbol{P'} - \boldsymbol{p}_3)^2 + m_4^2}}, \tag{C.17}$$

$\mathcal{R}_2(E', \boldsymbol{P'})$ is derived as

$$\mathcal{R}_2(E', \boldsymbol{P'}) \;=\; \int d\Omega_3 \left[p_3^{*2} \left| \frac{p_3^*}{E_3^*} + \frac{p_3^* - P' \cos\theta_3}{E_4^*} \right|^{-1} \right]$$

$$\;=\; 2\pi \int d\cos\theta_3 \left[p_3^{*2} \left| \frac{p_3^*}{E_3^*} + \frac{p_3^* - P' \cos\theta_3}{E_4^*} \right|^{-1} \right] \tag{C.18}$$

where

$$E_3^* = \sqrt{p_3^{*2} + m_3^2}, \quad E_4^* = \sqrt{(\boldsymbol{P'} - \boldsymbol{p}_3^*)^2 + m_4^2}. \tag{C.19}$$

C.4   Two-body kinematics

As defined $P' = |\boldsymbol{P'}|$, $B = 0$ gives

$$\sqrt{p_3^2 + m_3^2} + \sqrt{(\boldsymbol{P'} - \boldsymbol{p}_3^2)^2 + m_4^2} - E' = 0 .$$

This equation is simplified in a straightforward way as

$$a \, p_3^2 + 2 \, b \, p_3 + c = 0 \tag{C.20}$$

where

$$
\begin{aligned}
a &= 4\left(E'^2 - P'^2 \cos^2\theta_3 \right), \\
b &= -2 \, P' \cos\theta_3 \, \alpha , \\
c &= 4 \, E'^2 m_3^2 - \alpha^2 , \\
\alpha &= E'^2 + m_3^2 - m_4^2 - P'^2 .
\end{aligned}
$$

The solution of Eq. (C.20) is

$$p_3 = \frac{-b \pm \sqrt{b^2 - ac}}{a} . \tag{C.21}$$

The physical solution p_3^* of the $B = 0$ is the p_3 solutions that are real and positive. This solution of p_3^* makes the two-body phase space of Eq. (C.18) definite, therefore, the mass distribution of the four-body phase space of Eq. (C.14) is also given.

Here, the condition under which the physical solution exists is discussed at a different viewpoint. In the center of mass system of the particles 3 and 4, the momentum of the particle 3 is given as

$$p_3^c = \frac{\sqrt{\{M_{34}^2 - (m_3 + m_4)^2\}\{M_{34}^2 - (m_3 - m_4)^2\}}}{2M_{34}} .$$ (C.22)

The relative velocities $\beta_3^c = \frac{p_3^c}{E_3^*}$ and $\beta = \frac{P'}{E'}$ are defined, and $\gamma_3^* = \frac{1}{\sqrt{1-\beta_3^{c2}}}$, $\gamma = \frac{1}{\sqrt{1-\beta}}$. There are 3 cases depending on the relative velocities. Let θ_3 be the angle between the directions of $\boldsymbol{p_3}$ and $\boldsymbol{P'}$. The number of the physical solution of p_3 and the maximum of the angle θ_3 are classified by 3 cases.

1. $\beta < \beta_3^c$
   There is one physical solution for p_3 and $(\theta_3)_{max} = 180°$.

2. $\beta = \beta_3^c$
   There is one physical solution for p_3 and $(\theta_3)_{max} = 90°$.

3. $\beta > \beta_3^c$
   There are two physical solutions for p_3 and $(\theta_3)_{max}$ is given as follows.

$$\cos(\theta_3)_{max} = \sqrt{1 - \left(\frac{\beta_3^* \gamma_3^*}{\beta\gamma}\right)^2}$$ (C.23)

C.5   Supplement

The probability of the reaction for the n-particle final state P_n is defined in Lorentz invariant form as

$$d^{4n}P_n = d^{4n}R_n H.$$ (C.24)

H is the square of the invariant matrix element for the process and R_n is the invariant phase space defined by

$$d^{4n}R_n = \prod_{j=1}^{n} d^4q_j \, \delta^4\left(\sum_{j=1}^{n} q_j - Q\right) \prod_{j=1}^{n} \delta(q_j^2 - m_j^2) .$$ (C.25)

q_j represents a four-momentum of the j-th particle that has an energy E_j and a momentum $\boldsymbol{p}_j$,

$$q_j = (E_j, \boldsymbol{p}_j) .$$ (C.26)

It satisfies the following relation

$$q_j^2 = E_j^2 - \boldsymbol{p}_j^2 = m_j^2 .$$ (C.27)

The total four-momentum Q of the system has the components

$$Q = (E, \boldsymbol{P}) \,. \tag{C.28}$$

By using a property of the Dirac δ-function, the following relation is proved.

$$
\begin{aligned}
\int \delta(q_j^2 - m_j^2)\, d(q_j)_0 &= \left[\left| \frac{\partial}{\partial(q_j)_0}\, (q_j^2 - m_j^2) \right|^{-1} \right]_{(q_j)_0 = E_j} \\
&= \left[\left| \frac{\partial}{\partial(q_j)_0}\left((q_j)_0^2 - \boldsymbol{p}_j^2 - m_j^2 \right) \right|^{-1} \right]_{(q_j)_0 = \sqrt{\boldsymbol{P}_j^2 + m_j^2}} \\
&= \left[\frac{1}{2(q_j)_0} \right]_{(q_j)_0 = E_j} \\
&= \frac{1}{2E_j} \tag{C.29}
\end{aligned}
$$

This relation simplify the phase space as

$$d^{3n}R_n = \prod_{j=1}^{n} \frac{d^3 \boldsymbol{p}_j}{2E_j}\, \delta^3 \left(\sum_{j=1}^{n} \boldsymbol{p}_j - \boldsymbol{P} \right) \delta \left(\sum_{j=1}^{n} E_j - E \right) \,. \tag{C.30}$$

The probability in the invariant form is equivalent to that in the noninvariant form provided that

$$\mathcal{H} = \prod_{j=1}^{n} \frac{1}{2E_j} H \,. \tag{C.31}$$

Appendix D

Numerical data tables

Table D.1: Data table for the ^{40}Ca($\vec{p}, 2p$) reaction for the peaks at 8.3 and 10.9 MeV in the separation energy at the set1 in Table 2.1.

E_{sep} (MeV)	E_1 (MeV)	p_3 (MeV/c)	$\frac{d\sigma}{d\Omega_1 d\Omega_2 dE_1}$ (μb/sr^2 MeV)	A_y
8.3	230.0	-164.3	59.23 ± 0.62	0.215 ± 0.015
8.3	234.0	-154.9	73.63 ± 0.70	0.244 ± 0.013
8.3	238.0	-145.4	86.84 ± 0.76	0.231 ± 0.012
8.3	246.0	-126.4	116.27 ± 0.86	0.202 ± 0.010
8.3	250.0	-116.7	124.91 ± 0.91	0.233 ± 0.010
8.3	254.0	-107.1	130.78 ± 0.92	0.209 ± 0.010
8.3	258.0	-97.4	131.42 ± 0.93	0.207 ± 0.010
8.3	266.0	-77.7	121.58 ± 0.90	0.154 ± 0.010
8.3	270.0	-67.8	104.50 ± 0.83	0.097 ± 0.011
8.3	274.0	-57.9	88.61 ± 0.78	0.086 ± 0.012
8.3	278.0	-47.9	74.03 ± 0.72	0.059 ± 0.014
8.3	286.0	-28.0	49.89 ± 0.41	0.130 ± 0.013
8.3	290.0	-18.6	43.50 ± 0.55	0.220 ± 0.020
8.3	294.0	-11.4	40.51 ± 0.55	0.353 ± 0.021
8.3	298.0	12.0	41.09 ± 0.57	0.415 ± 0.021
10.9	230.0	-160.3	34.77 ± 0.48	0.002 ± 0.020
10.9	234.0	-150.9	35.93 ± 1.14	0.031 ± 0.020
10.9	238.0	-141.3	36.34 ± 0.50	0.015 ± 0.020
10.9	246.0	-122.1	32.42 ± 0.49	-0.085 ± 0.021
10.9	250.0	-112.4	28.14 ± 0.46	-0.053 ± 0.023
10.9	254.0	-102.6	27.89 ± 0.47	0.062 ± 0.024
10.9	258.0	-92.8	32.34 ± 0.50	0.242 ± 0.022
10.9	266.0	-73.0	72.82 ± 0.75	0.432 ± 0.014
10.9	270.0	-62.9	116.95 ± 0.96	0.429 ± 0.011
10.9	274.0	-52.8	172.49 ± 1.20	0.409 ± 0.010
10.9	278.0	-42.6	239.18 ± 1.45	0.387 ± 0.008
10.9	286.0	-22.2	382.27 ± 1.43	0.326 ± 0.006
10.9	290.0	-12.5	422.91 ± 2.14	0.310 ± 0.008
10.9	294.0	6.9	437.52 ± 2.11	0.282 ± 0.007
10.9	298.0	13.3	416.79 ± 1.98	0.263 ± 0.007

Table D.2: Data table for the ^{40}Ca($\vec{p}, 2p$) reaction at the set2 in Table 2.1. $\Delta E_{sep} = 2$ MeV.

E_{sep} (MeV)	E_1 (MeV)	p_3 (MeV/c)	$\frac{d\sigma}{d\Omega_1 d\Omega_2 dE_1}$ (μb/sr^2 MeV)	A_y
13.0	214.0	−169.3	19.58 ± 0.37	0.071 ± 0.026
13.0	218.0	−160.6	19.07 ± 0.37	0.078 ± 0.027
13.0	222.0	−151.9	19.54 ± 0.37	0.076 ± 0.027
13.0	226.0	−143.1	23.07 ± 0.40	0.078 ± 0.025
13.0	230.0	−134.4	31.58 ± 0.45	0.039 ± 0.020
13.0	234.0	−125.6	28.20 ± 0.43	0.062 ± 0.022
13.0	238.0	−116.9	27.05 ± 0.43	0.087 ± 0.022
13.0	246.0	−99.3	44.81 ± 0.54	0.044 ± 0.017
13.0	250.0	−90.6	36.81 ± 1.07	0.069 ± 0.019
13.0	254.0	−81.9	32.90 ± 1.35	0.111 ± 0.021
13.0	258.0	−73.3	32.41 ± 1.36	0.117 ± 0.021
13.0	266.0	−56.5	36.02 ± 0.42	0.231 ± 0.018
13.0	270.0	−48.6	32.77 ± 0.40	0.236 ± 0.019
13.0	274.0	−41.4	33.86 ± 0.41	0.260 ± 0.019
13.0	278.0	−35.4	35.18 ± 0.42	0.265 ± 0.018
15.0	214.0	−166.1	38.10 ± 0.80	0.110 ± 0.018
15.0	218.0	−157.3	46.08 ± 0.53	0.057 ± 0.016
15.0	222.0	−148.5	53.07 ± 0.57	0.044 ± 0.015
15.0	226.0	−139.7	56.73 ± 0.59	0.053 ± 0.015
15.0	230.0	−130.9	56.41 ± 0.59	0.060 ± 0.015
15.0	234.0	−122.1	63.88 ± 0.62	0.064 ± 0.014
15.0	238.0	−113.2	68.06 ± 0.64	0.028 ± 0.013
15.0	246.0	−95.5	56.86 ± 0.60	0.072 ± 0.015
15.0	250.0	−86.7	59.41 ± 1.22	0.088 ± 0.014
15.0	254.0	−77.8	60.35 ± 1.54	0.083 ± 0.014
15.0	258.0	−69.1	56.77 ± 1.23	0.121 ± 0.015
15.0	266.0	−52.1	48.26 ± 0.46	0.148 ± 0.015
15.0	270.0	−44.1	47.33 ± 0.47	0.204 ± 0.015
15.0	274.0	−36.9	44.67 ± 0.46	0.194 ± 0.016
15.0	278.0	−31.1	41.20 ± 0.45	0.217 ± 0.017

Table D.2 (Continued)

E_{sep} (MeV)	E_1 (MeV)	p_3 (MeV/c)	$\frac{d\sigma}{d\Omega_1 d\Omega_2 dE_1}$ (μb/sr^2 MeV)	A_y
17.0	214.0	−162.9	27.93 ± 0.43	0.122 ± 0.022
17.0	218.0	−154.1	32.04 ± 0.46	0.046 ± 0.020
17.0	222.0	−145.2	35.90 ± 0.48	0.068 ± 0.019
17.0	226.0	−136.3	39.01 ± 0.50	0.053 ± 0.018
17.0	230.0	−127.5	40.84 ± 0.51	0.049 ± 0.017
17.0	234.0	−118.5	45.33 ± 0.53	0.079 ± 0.017
17.0	238.0	−109.6	46.61 ± 0.54	0.035 ± 0.016
17.0	246.0	−91.7	42.66 ± 1.00	0.030 ± 0.017
17.0	250.0	−82.7	42.46 ± 1.04	0.011 ± 0.018
17.0	254.0	−73.8	42.54 ± 0.54	0.081 ± 0.018
17.0	258.0	−64.9	38.81 ± 0.52	0.113 ± 0.019
17.0	266.0	−47.7	34.27 ± 0.40	0.154 ± 0.018
17.0	270.0	−39.6	31.55 ± 0.40	0.166 ± 0.019
17.0	274.0	−32.4	28.95 ± 0.39	0.162 ± 0.021
17.0	278.0	−26.8	26.97 ± 0.38	0.163 ± 0.022
19.0	214.0	−159.7	13.08 ± 0.32	0.145 ± 0.034
19.0	218.0	−150.8	15.05 ± 0.34	0.129 ± 0.032
19.0	222.0	−141.9	16.14 ± 0.35	0.047 ± 0.031
19.0	226.0	−133.0	17.46 ± 0.36	0.083 ± 0.029
19.0	230.0	−124.0	18.41 ± 0.37	0.110 ± 0.028
19.0	234.0	−115.0	20.30 ± 0.39	0.100 ± 0.027
19.0	238.0	−106.0	21.38 ± 0.40	0.060 ± 0.026
19.0	246.0	−87.9	20.35 ± 0.40	0.117 ± 0.028
19.0	250.0	−78.8	21.21 ± 0.41	0.059 ± 0.027
19.0	254.0	−69.7	22.01 ± 0.42	0.068 ± 0.027
19.0	258.0	−60.7	20.81 ± 0.41	0.135 ± 0.028
19.0	266.0	−43.2	19.35 ± 0.33	0.078 ± 0.027
19.0	270.0	−35.0	19.14 ± 0.34	0.111 ± 0.027
19.0	274.0	−27.8	17.89 ± 0.34	0.106 ± 0.029
19.0	278.0	−22.7	16.64 ± 0.33	0.076 ± 0.031

E_{sep} (MeV)	E_1 (MeV)	p_3 (MeV/c)	$\frac{d\sigma}{d\Omega_1 d\Omega_2 dE_1}$ (μb/sr^2 MeV)	A_y
21.0	214.0	−156.6	8.49 ± 0.28	−0.015 ± 0.046
21.0	218.0	−147.6	9.33 ± 0.29	0.109 ± 0.044
21.0	222.0	−138.6	10.11 ± 0.30	0.101 ± 0.042
21.0	226.0	−129.6	11.67 ± 0.32	0.067 ± 0.038
21.0	230.0	−120.6	11.72 ± 0.32	0.051 ± 0.038
21.0	234.0	−111.5	12.68 ± 0.33	0.102 ± 0.036
21.0	238.0	−102.4	13.22 ± 0.34	0.068 ± 0.036
21.0	246.0	−84.1	13.96 ± 0.36	0.081 ± 0.036
21.0	250.0	−74.9	13.18 ± 0.36	0.086 ± 0.038
21.0	254.0	−65.7	13.82 ± 0.36	0.127 ± 0.037
21.0	258.0	−56.5	12.70 ± 0.36	−0.025 ± 0.040
21.0	266.0	−38.7	12.66 ± 0.30	0.041 ± 0.037
21.0	270.0	−30.4	12.00 ± 0.30	0.109 ± 0.039
21.0	274.0	−23.2	11.47 ± 0.30	0.060 ± 0.041
21.0	278.0	−18.9	11.10 ± 0.30	0.160 ± 0.042
23.0	214.0	−153.4	8.62 ± 0.28	0.098 ± 0.046
23.0	218.0	−144.4	9.18 ± 0.29	0.157 ± 0.044
23.0	222.0	−135.4	10.86 ± 0.31	0.139 ± 0.040
23.0	226.0	−126.3	11.34 ± 0.32	0.140 ± 0.039
23.0	230.0	−117.1	11.97 ± 0.32	0.097 ± 0.038
23.0	234.0	−108.0	13.24 ± 0.33	0.120 ± 0.035
23.0	238.0	−98.8	13.78 ± 0.34	0.016 ± 0.035
23.0	246.0	−80.3	14.26 ± 0.36	0.094 ± 0.035
23.0	250.0	−71.0	14.75 ± 0.37	0.090 ± 0.035
23.0	254.0	−61.7	14.18 ± 0.37	0.102 ± 0.036
23.0	258.0	−52.4	14.59 ± 0.38	0.155 ± 0.036
23.0	266.0	−34.1	13.66 ± 0.31	0.161 ± 0.035
23.0	270.0	−25.7	12.91 ± 0.31	0.105 ± 0.037
23.0	274.0	−18.7	12.41 ± 0.31	0.147 ± 0.038
23.0	278.0	15.6	11.80 ± 0.31	0.228 ± 0.040

E_{sep} (MeV)	E_1 (MeV)	p_3 (MeV/c)	$\frac{d\sigma}{d\Omega_1 d\Omega_2 dE_1}$ (μb/sr^2 MeV)	A_y
25.0	214.0	−150.3	8.64 ± 0.28	0.113 ± 0.046
25.0	218.0	−141.2	9.72 ± 0.30	0.122 ± 0.043
25.0	222.0	−132.1	11.29 ± 0.31	0.079 ± 0.039
25.0	226.0	−122.9	12.32 ± 0.33	0.059 ± 0.037
25.0	230.0	−113.7	13.40 ± 0.33	0.138 ± 0.035
25.0	234.0	−104.5	14.77 ± 0.35	0.075 ± 0.033
25.0	238.0	−95.2	15.66 ± 0.36	0.071 ± 0.032
25.0	246.0	−76.5	17.15 ± 0.38	0.082 ± 0.031
25.0	250.0	−67.1	17.11 ± 0.39	0.119 ± 0.032
25.0	254.0	−57.7	16.53 ± 0.39	0.081 ± 0.033
25.0	258.0	−48.2	17.55 ± 0.40	0.117 ± 0.032
25.0	266.0	−29.6	15.59 ± 0.32	0.105 ± 0.032
25.0	270.0	−21.0	14.45 ± 0.32	0.103 ± 0.034
25.0	274.0	−14.3	13.18 ± 0.31	0.123 ± 0.037
25.0	278.0	13.3	12.91 ± 0.31	0.063 ± 0.037
27.0	214.0	−147.2	10.80 ± 0.30	0.134 ± 0.039
27.0	218.0	−138.0	12.12 ± 0.32	0.140 ± 0.037
27.0	222.0	−128.9	13.62 ± 0.33	0.079 ± 0.034
27.0	226.0	−119.6	15.39 ± 0.35	0.121 ± 0.032
27.0	230.0	−110.4	16.93 ± 0.36	0.080 ± 0.030
27.0	234.0	−101.1	18.44 ± 0.38	0.087 ± 0.029
27.0	238.0	−91.7	19.57 ± 0.39	0.116 ± 0.028
27.0	246.0	−72.8	21.32 ± 0.41	0.110 ± 0.027
27.0	250.0	−63.2	20.88 ± 0.41	0.099 ± 0.028
27.0	254.0	−53.7	21.69 ± 0.42	0.124 ± 0.027
27.0	258.0	−44.1	21.45 ± 0.42	0.087 ± 0.028
27.0	266.0	−25.0	18.49 ± 0.33	0.058 ± 0.028
27.0	270.0	−16.2	16.62 ± 0.33	0.089 ± 0.030
27.0	274.0	−10.2	15.71 ± 0.32	0.076 ± 0.032
27.0	278.0	12.6	14.62 ± 0.32	0.071 ± 0.034

Table D.2 *(Continued)*

E_{sep} (MeV)	E_1 (MeV)	p_3 (MeV/c)	$\frac{d\sigma}{d\Omega_1 d\Omega_2 dE_1}$ (μb/sr^2 MeV)	A_y
29.0	214.0	−144.1	11.09 ± 0.31	0.116 ± 0.039
29.0	218.0	−134.9	12.96 ± 0.32	0.108 ± 0.035
29.0	222.0	−125.7	14.96 ± 0.35	0.107 ± 0.032
29.0	226.0	−116.4	16.33 ± 0.36	0.158 ± 0.031
29.0	230.0	−107.0	18.36 ± 0.37	0.101 ± 0.028
29.0	234.0	−97.6	18.97 ± 0.38	0.077 ± 0.028
29.0	238.0	−88.2	21.63 ± 0.40	0.098 ± 0.026
29.0	246.0	−69.1	22.30 ± 0.42	0.050 ± 0.026
29.0	250.0	−59.4	22.24 ± 0.42	0.077 ± 0.027
29.0	254.0	−49.7	21.76 ± 0.42	0.069 ± 0.027
29.0	258.0	−40.0	20.98 ± 0.42	0.064 ± 0.028
29.0	266.0	−20.5	19.66 ± 0.34	0.059 ± 0.027
29.0	270.0	−11.4	16.71 ± 0.33	0.058 ± 0.030
29.0	274.0	7.1	15.66 ± 0.32	0.061 ± 0.032
29.0	278.0	13.8	13.95 ± 0.32	0.116 ± 0.035
31.0	214.0	−141.0	10.80 ± 0.31	0.088 ± 0.040
31.0	218.0	−131.8	12.74 ± 0.33	0.173 ± 0.036
31.0	222.0	−122.5	14.44 ± 0.34	0.104 ± 0.033
31.0	226.0	−113.1	17.28 ± 0.37	0.080 ± 0.030
31.0	230.0	−103.7	18.20 ± 0.37	0.076 ± 0.029
31.0	234.0	−94.3	19.28 ± 0.38	0.072 ± 0.028
31.0	238.0	−84.7	19.99 ± 0.39	0.056 ± 0.027
31.0	246.0	−65.5	21.69 ± 0.42	0.101 ± 0.027
31.0	250.0	−55.7	21.88 ± 0.42	0.098 ± 0.027
31.0	254.0	−45.9	21.11 ± 0.42	0.009 ± 0.028
31.0	258.0	−36.0	19.84 ± 0.41	0.092 ± 0.029
31.0	266.0	−16.0	17.75 ± 0.33	0.048 ± 0.029
31.0	270.0	−6.6	16.08 ± 0.32	0.028 ± 0.031
31.0	274.0	6.7	14.20 ± 0.32	0.080 ± 0.035
31.0	278.0	16.5	13.25 ± 0.31	0.051 ± 0.036

Table D.2 *(Continued)*

E_{sep} (MeV)	E_1 (MeV)	p_3 (MeV/c)	$\frac{d\sigma}{d\Omega_1 d\Omega_2 dE_1}$ (μb/sr^2 MeV)	A_y
33.0	214.0	−138.0	10.28 ± 0.30	0.092 ± 0.042
33.0	218.0	−128.7	13.24 ± 0.33	0.146 ± 0.035
33.0	222.0	−119.3	13.64 ± 0.34	0.109 ± 0.035
33.0	226.0	−109.9	15.27 ± 0.35	0.113 ± 0.032
33.0	230.0	−100.4	16.53 ± 0.36	0.101 ± 0.031
33.0	234.0	−90.9	18.05 ± 0.38	0.073 ± 0.029
33.0	238.0	−81.3	19.03 ± 0.38	0.077 ± 0.028
33.0	246.0	−61.9	20.78 ± 0.41	0.036 ± 0.028
33.0	250.0	−52.1	20.41 ± 0.41	0.083 ± 0.028
33.0	254.0	−42.1	18.32 ± 0.40	0.051 ± 0.030
33.0	258.0	−32.1	17.08 ± 0.39	−0.020 ± 0.032
33.0	266.0	−11.7	15.86 ± 0.32	0.048 ± 0.032
33.0	270.0	−1.7	14.61 ± 0.32	0.050 ± 0.034
33.0	274.0	9.5	13.71 ± 0.31	0.126 ± 0.036
33.0	278.0	20.2	11.32 ± 0.30	0.146 ± 0.041
35.0	214.0	−135.0	10.07 ± 0.30	0.090 ± 0.042
35.0	218.0	−125.6	11.71 ± 0.32	0.156 ± 0.038
35.0	222.0	−116.2	12.86 ± 0.33	0.052 ± 0.036
35.0	226.0	−106.7	14.15 ± 0.34	0.074 ± 0.034
35.0	230.0	−97.2	14.80 ± 0.35	0.138 ± 0.033
35.0	234.0	−87.6	16.41 ± 0.36	0.071 ± 0.031
35.0	238.0	−78.0	16.86 ± 0.37	0.016 ± 0.031
35.0	246.0	−58.4	17.56 ± 0.39	0.049 ± 0.031
35.0	250.0	−48.5	17.18 ± 0.39	0.009 ± 0.032
35.0	254.0	−38.5	16.43 ± 0.39	0.043 ± 0.033
35.0	258.0	−28.4	15.88 ± 0.38	0.057 ± 0.034
35.0	266.0	−7.9	15.13 ± 0.32	0.061 ± 0.033
35.0	270.0	3.3	13.38 ± 0.31	0.106 ± 0.036
35.0	274.0	13.6	11.74 ± 0.30	0.082 ± 0.040
35.0	278.0	24.4	10.56 ± 0.29	0.044 ± 0.043

Table D.3: Data table for the $^{40}\text{Ca}(\vec{p}, 2p)$ reaction at the set3 in Table 2.1. $\Delta E_{\text{sep}} = 2$ MeV.

E_{sep} (MeV)	E_1 (MeV)	p_3 (MeV/c)	$\frac{d\sigma}{d\Omega_1 d\Omega_2 dE_1}$ (μb/sr^2 MeV)	A_y
29.0	202.0	−147.6	9.30 ± 0.31	0.106 ± 0.045
29.0	206.0	−139.3	11.25 ± 0.33	0.198 ± 0.040
29.0	210.0	−130.9	12.39 ± 0.34	0.147 ± 0.038
29.0	214.0	−122.5	13.30 ± 0.36	−0.009 ± 0.037
29.0	218.0	−114.2	15.23 ± 0.38	0.079 ± 0.034
29.0	222.0	−105.8	17.02 ± 0.39	0.070 ± 0.032
29.0	226.0	−97.5	18.52 ± 0.41	0.088 ± 0.030
29.0	230.0	−89.2	19.17 ± 0.41	0.122 ± 0.029
29.0	234.0	−80.9	20.77 ± 0.43	0.086 ± 0.028
29.0	238.0	−72.8	20.41 ± 0.43	0.081 ± 0.028
29.0	246.0	−57.0	20.00 ± 0.31	0.061 ± 0.024
29.0	250.0	−49.5	19.27 ± 0.31	0.025 ± 0.025
29.0	254.0	−42.7	18.89 ± 0.31	0.046 ± 0.026
29.0	258.0	−37.0	18.70 ± 0.31	0.036 ± 0.026
31.0	202.0	−144.4	9.14 ± 0.31	0.041 ± 0.046
31.0	206.0	−136.0	10.90 ± 0.33	0.149 ± 0.041
31.0	210.0	−127.5	12.89 ± 0.35	0.197 ± 0.037
31.0	214.0	−119.1	13.83 ± 0.36	0.062 ± 0.036
31.0	218.0	−110.6	14.34 ± 0.37	0.019 ± 0.036
31.0	222.0	−102.2	16.30 ± 0.39	0.092 ± 0.033
31.0	226.0	−93.7	18.05 ± 0.41	−0.008 ± 0.031
31.0	230.0	−85.3	18.75 ± 0.41	0.079 ± 0.029
31.0	234.0	−77.0	19.61 ± 0.42	0.021 ± 0.029
31.0	238.0	−68.7	20.23 ± 0.43	0.094 ± 0.028
31.0	246.0	−52.6	18.70 ± 0.30	0.039 ± 0.026
31.0	250.0	−45.1	18.48 ± 0.30	0.030 ± 0.026
31.0	254.0	−38.3	18.38 ± 0.31	0.030 ± 0.026
31.0	258.0	−32.6	17.12 ± 0.30	0.032 ± 0.028

Table D.3 (Continued)

E_{sep} (MeV)	E_1 (MeV)	p_3 (MeV/c)	$\frac{d\sigma}{d\Omega_1 d\Omega_2 dE_1}$ (μb/sr^2 MeV)	A_y
33.0	202.0	−141.2	9.69 ± 0.31	0.083 ± 0.044
33.0	206.0	−132.7	11.04 ± 0.32	0.104 ± 0.040
33.0	210.0	−124.2	11.85 ± 0.34	0.101 ± 0.040
33.0	214.0	−115.6	13.56 ± 0.36	0.085 ± 0.037
33.0	218.0	−107.1	14.92 ± 0.37	0.040 ± 0.035
33.0	222.0	−98.6	15.63 ± 0.39	0.168 ± 0.034
33.0	226.0	−90.0	17.68 ± 0.40	0.150 ± 0.031
33.0	230.0	−81.5	17.64 ± 0.40	0.037 ± 0.031
33.0	234.0	−73.0	18.24 ± 0.41	0.025 ± 0.030
33.0	238.0	−64.6	18.61 ± 0.42	−0.023 ± 0.030
33.0	246.0	−48.2	17.35 ± 0.30	0.040 ± 0.027
33.0	250.0	−40.6	16.99 ± 0.30	0.073 ± 0.028
33.0	254.0	−33.7	16.38 ± 0.30	0.110 ± 0.029
33.0	258.0	−28.3	16.27 ± 0.30	0.089 ± 0.029
35.0	202.0	−138.0	9.46 ± 0.31	0.063 ± 0.045
35.0	206.0	−129.4	10.40 ± 0.32	0.031 ± 0.043
35.0	210.0	−120.8	11.72 ± 0.34	0.088 ± 0.040
35.0	214.0	−112.2	12.18 ± 0.35	0.064 ± 0.040
35.0	218.0	−103.6	13.90 ± 0.37	0.087 ± 0.036
35.0	222.0	−94.9	15.13 ± 0.38	0.021 ± 0.035
35.0	226.0	−86.3	15.69 ± 0.39	0.060 ± 0.034
35.0	230.0	−77.7	16.11 ± 0.39	0.039 ± 0.033
35.0	234.0	−69.1	16.66 ± 0.40	0.028 ± 0.032
35.0	238.0	−60.5	17.34 ± 0.41	0.052 ± 0.032
35.0	246.0	−43.9	16.14 ± 0.29	0.054 ± 0.029
35.0	250.0	−36.1	14.74 ± 0.29	0.063 ± 0.031
35.0	254.0	−29.2	15.08 ± 0.29	0.035 ± 0.031
35.0	258.0	−24.1	14.50 ± 0.29	0.079 ± 0.032

Table D.3 *(Continued)*

E_{sep} (MeV)	E_1 (MeV)	p_3 (MeV/c)	$\frac{d\sigma}{d\Omega_1 d\Omega_2 dE_1}$ (μb/sr^2 MeV)	A_y
37.0	202.0	−134.8	8.56 ± 0.30	0.061 ± 0.049
37.0	206.0	−126.2	9.73 ± 0.32	0.082 ± 0.045
37.0	210.0	−117.5	10.47 ± 0.32	0.067 ± 0.043
37.0	214.0	−108.8	11.46 ± 0.35	0.041 ± 0.042
37.0	218.0	−100.1	12.46 ± 0.35	0.065 ± 0.039
37.0	222.0	−91.4	13.40 ± 0.37	0.041 ± 0.038
37.0	226.0	−82.6	13.74 ± 0.37	0.020 ± 0.037
37.0	230.0	−73.9	14.39 ± 0.38	−0.008 ± 0.035
37.0	234.0	−65.1	15.10 ± 0.39	0.085 ± 0.035
37.0	238.0	−56.4	15.75 ± 0.39	0.026 ± 0.034
37.0	246.0	−39.5	14.05 ± 0.28	0.058 ± 0.032
37.0	250.0	−31.5	14.19 ± 0.28	0.054 ± 0.032
37.0	254.0	−24.7	14.03 ± 0.29	0.052 ± 0.032
37.0	258.0	−20.0	12.50 ± 0.28	0.084 ± 0.036
39.0	202.0	−131.7	7.80 ± 0.30	0.120 ± 0.053
39.0	206.0	−123.0	8.04 ± 0.30	0.089 ± 0.052
39.0	210.0	−114.2	9.72 ± 0.32	0.091 ± 0.045
39.0	214.0	−105.4	10.06 ± 0.33	−0.040 ± 0.046
39.0	218.0	−96.6	10.86 ± 0.34	0.018 ± 0.044
39.0	222.0	−87.8	11.54 ± 0.35	0.067 ± 0.042
39.0	226.0	−78.9	11.58 ± 0.35	0.120 ± 0.042
39.0	230.0	−70.1	12.05 ± 0.36	0.030 ± 0.040
39.0	234.0	−61.2	12.76 ± 0.37	0.100 ± 0.039
39.0	238.0	−52.3	13.51 ± 0.38	0.056 ± 0.038
39.0	246.0	−35.0	12.27 ± 0.27	0.006 ± 0.035
39.0	250.0	−27.0	12.16 ± 0.27	−0.007 ± 0.036
39.0	254.0	−20.1	11.66 ± 0.27	0.109 ± 0.037
39.0	258.0	−16.3	11.46 ± 0.28	0.059 ± 0.038

Table D.3 *(Continued)*

E_{sep} (MeV)	E_1 (MeV)	p_3 (MeV/c)	$\frac{d\sigma}{d\Omega_1 d\Omega_2 dE_1}$ (μb/sr^2 MeV)	A_y
41.0	202.0	−128.6	7.06 ± 0.29	0.070 ± 0.057
41.0	206.0	−119.8	7.20 ± 0.29	0.042 ± 0.056
41.0	210.0	−110.9	8.64 ± 0.31	0.088 ± 0.049
41.0	214.0	−102.1	9.23 ± 0.33	0.079 ± 0.049
41.0	218.0	−93.2	10.01 ± 0.33	0.059 ± 0.046
41.0	222.0	−84.3	10.59 ± 0.34	0.017 ± 0.045
41.0	226.0	−75.3	10.53 ± 0.35	0.051 ± 0.046
41.0	230.0	−66.3	11.57 ± 0.35	0.080 ± 0.041
41.0	234.0	−57.3	11.69 ± 0.36	0.032 ± 0.041
41.0	238.0	−48.3	11.90 ± 0.37	0.020 ± 0.041
41.0	246.0	−30.6	11.60 ± 0.27	0.035 ± 0.037
41.0	250.0	−22.3	11.01 ± 0.27	0.008 ± 0.039
41.0	254.0	−15.6	10.81 ± 0.27	0.037 ± 0.040
41.0	258.0	13.3	9.96 ± 0.27	0.083 ± 0.043
43.0	202.0	−125.5	6.81 ± 0.29	0.036 ± 0.058
43.0	206.0	−116.6	7.22 ± 0.29	0.139 ± 0.056
43.0	210.0	−107.7	7.48 ± 0.30	0.052 ± 0.055
43.0	214.0	−98.8	7.97 ± 0.31	0.055 ± 0.054
43.0	218.0	−89.8	8.74 ± 0.32	0.026 ± 0.051
43.0	222.0	−80.8	8.75 ± 0.33	0.035 ± 0.051
43.0	226.0	−71.7	9.90 ± 0.34	0.067 ± 0.047
43.0	230.0	−62.6	10.70 ± 0.35	0.037 ± 0.044
43.0	234.0	−53.5	10.85 ± 0.36	−0.002 ± 0.044
43.0	238.0	−44.3	10.70 ± 0.36	0.064 ± 0.045
43.0	246.0	−26.2	10.99 ± 0.27	0.063 ± 0.039
43.0	250.0	−17.7	10.19 ± 0.27	0.067 ± 0.041
43.0	254.0	−11.2	10.23 ± 0.27	0.109 ± 0.042
43.0	258.0	11.5	9.94 ± 0.27	0.068 ± 0.043

Table D.3 *(Continued)*

E_{sep} (MeV)	E_1 (MeV)	p_3 (MeV/c)	$\frac{d\sigma}{d\Omega_1 d\Omega_2 dE_1}$ (μb/sr^2 MeV)	A_y
45.0	202.0	−122.4	5.95 ± 0.28	0.003 ± 0.065
45.0	206.0	−113.5	6.28 ± 0.29	0.133 ± 0.063
45.0	210.0	−104.5	7.25 ± 0.30	0.110 ± 0.057
45.0	214.0	−95.5	8.09 ± 0.31	0.055 ± 0.053
45.0	218.0	−86.4	7.84 ± 0.32	0.073 ± 0.055
45.0	222.0	−77.3	8.33 ± 0.33	0.148 ± 0.054
45.0	226.0	−68.2	8.59 ± 0.33	0.077 ± 0.053
45.0	230.0	−58.9	9.66 ± 0.34	0.019 ± 0.047
45.0	234.0	−49.7	10.21 ± 0.35	0.012 ± 0.046
45.0	238.0	−40.3	9.93 ± 0.35	0.097 ± 0.048
45.0	246.0	−21.7	10.63 ± 0.27	0.015 ± 0.040
45.0	250.0	−13.0	10.10 ± 0.26	0.069 ± 0.042
45.0	254.0	−7.3	10.17 ± 0.27	0.084 ± 0.042
45.0	258.0	11.6	10.01 ± 0.27	0.114 ± 0.043
47.0	202.0	−119.4	6.00 ± 0.28	0.087 ± 0.064
47.0	206.0	−110.4	6.34 ± 0.29	0.087 ± 0.062
47.0	210.0	−101.4	6.49 ± 0.29	0.062 ± 0.061
47.0	214.0	−92.3	6.88 ± 0.30	0.040 ± 0.061
47.0	218.0	−83.1	7.16 ± 0.31	0.120 ± 0.059
47.0	222.0	−73.9	7.98 ± 0.32	0.046 ± 0.055
47.0	226.0	−64.7	9.45 ± 0.34	0.118 ± 0.049
47.0	230.0	−55.4	10.02 ± 0.35	0.094 ± 0.046
47.0	234.0	−46.0	10.54 ± 0.35	0.176 ± 0.045
47.0	238.0	−36.5	9.78 ± 0.35	0.019 ± 0.048
47.0	246.0	−17.4	10.47 ± 0.26	0.072 ± 0.040
47.0	250.0	−8.2	10.91 ± 0.27	0.085 ± 0.039
47.0	254.0	5.1	10.35 ± 0.27	0.024 ± 0.041
47.0	258.0	13.6	9.62 ± 0.27	0.073 ± 0.044

Table D.3 *(Continued)*

E_{sep} (MeV)	E_1 (MeV)	p_3 (MeV/c)	$\frac{d\sigma}{d\Omega_1 d\Omega_2 dE_1}$ (μb/sr^2 MeV)	A_y
49.0	202.0	−116.4	5.15 ± 0.27	0.056 ± 0.073
49.0	206.0	−107.3	6.30 ± 0.28	0.080 ± 0.062
49.0	210.0	−98.2	6.33 ± 0.29	0.000 ± 0.062
49.0	214.0	−89.1	7.57 ± 0.31	0.183 ± 0.056
49.0	218.0	−79.9	7.30 ± 0.31	0.048 ± 0.059
49.0	222.0	−70.6	8.37 ± 0.32	−0.020 ± 0.053
49.0	226.0	−61.3	8.11 ± 0.32	0.072 ± 0.055
49.0	230.0	−51.9	9.58 ± 0.34	0.046 ± 0.047
49.0	234.0	−42.4	9.66 ± 0.34	0.072 ± 0.048
49.0	238.0	−32.8	9.59 ± 0.35	0.082 ± 0.048
49.0	246.0	−13.3	10.21 ± 0.26	0.074 ± 0.041
49.0	250.0	−3.5	10.08 ± 0.27	0.014 ± 0.042
49.0	254.0	6.8	10.02 ± 0.27	0.075 ± 0.042
49.0	258.0	17.0	10.31 ± 0.27	0.063 ± 0.041
51.0	202.0	−113.4	5.07 ± 0.27	−0.008 ± 0.074
51.0	206.0	−104.3	5.38 ± 0.28	0.108 ± 0.071
51.0	210.0	−95.2	6.19 ± 0.28	0.009 ± 0.063
51.0	214.0	−86.0	6.51 ± 0.30	0.050 ± 0.064
51.0	218.0	−76.7	7.03 ± 0.31	0.084 ± 0.060
51.0	222.0	−67.4	7.20 ± 0.31	0.091 ± 0.060
51.0	226.0	−58.0	7.87 ± 0.32	0.063 ± 0.056
51.0	230.0	−48.5	8.82 ± 0.34	−0.010 ± 0.051
51.0	234.0	−38.9	9.39 ± 0.34	0.031 ± 0.049
51.0	238.0	−29.3	9.33 ± 0.35	−0.021 ± 0.050
51.0	246.0	−9.7	9.82 ± 0.26	0.032 ± 0.042
51.0	250.0	1.9	9.44 ± 0.26	0.044 ± 0.044
51.0	254.0	10.8	9.57 ± 0.26	0.100 ± 0.044
51.0	258.0	21.0	9.42 ± 0.26	0.069 ± 0.045

Table D.3 (Continued)

E_{sep}	E_1	p_3	$\frac{d\sigma}{d\Omega_1 d\Omega_2 dE_1}$	A_y
(MeV)	(MeV)	(MeV/c)	(μb/sr^2 MeV)	
53.0	202.0	−110.6	5.03 ± 0.27	0.094 ± 0.074
53.0	206.0	−101.4	5.13 ± 0.27	0.135 ± 0.073
53.0	210.0	−92.2	5.56 ± 0.28	−0.058 ± 0.070
53.0	214.0	−83.0	6.11 ± 0.30	0.095 ± 0.067
53.0	218.0	−73.7	6.36 ± 0.30	0.070 ± 0.065
53.0	222.0	−64.3	6.56 ± 0.30	0.083 ± 0.064
53.0	226.0	−54.8	7.81 ± 0.32	0.085 ± 0.056
53.0	230.0	−45.3	8.30 ± 0.33	0.110 ± 0.053
53.0	234.0	−35.7	8.43 ± 0.33	0.032 ± 0.053
53.0	238.0	−26.1	9.08 ± 0.34	0.047 ± 0.051
53.0	246.0	−7.6	8.80 ± 0.26	0.018 ± 0.047
53.0	250.0	6.5	9.44 ± 0.26	0.065 ± 0.044
53.0	254.0	15.4	9.15 ± 0.26	0.059 ± 0.045
53.0	258.0	25.5	8.80 ± 0.26	0.034 ± 0.047

Table D.4: Data table for the ^{40}Ca($\vec{p}, 2p$) reaction at the set4 in Table 2.1. $\Delta E_{\text{sep}} = 2$ MeV.

E_{sep}	E_1	p_3	$\frac{d\sigma}{d\Omega_1 d\Omega_2 dE_1}$	A_y
(MeV)	(MeV)	(MeV/c)	(μb/sr^2 MeV)	
41.0	186.0	−140.9	5.57 ± 0.36	0.088 ± 0.096
41.0	190.0	−133.0	6.41 ± 0.37	0.051 ± 0.087
41.0	194.0	−125.1	7.55 ± 0.39	0.104 ± 0.078
41.0	202.0	−109.3	7.55 ± 0.32	−0.004 ± 0.063
41.0	206.0	−101.5	8.64 ± 0.33	−0.043 ± 0.057
41.0	210.0	−93.7	8.83 ± 0.34	−0.079 ± 0.057
41.0	214.0	−86.0	9.23 ± 0.32	0.031 ± 0.049
41.0	218.0	−78.3	9.74 ± 0.33	0.127 ± 0.048
41.0	222.0	−70.9	9.15 ± 0.32	0.090 ± 0.051
41.0	226.0	−63.6	10.75 ± 0.34	−0.046 ± 0.045
41.0	230.0	−56.6	9.30 ± 0.26	−0.017 ± 0.045
41.0	234.0	−50.1	9.78 ± 0.27	0.066 ± 0.043
41.0	238.0	−44.3	9.93 ± 0.27	0.040 ± 0.043
43.0	186.0	−137.8	5.20 ± 0.35	0.156 ± 0.101
43.0	190.0	−129.7	5.57 ± 0.36	0.051 ± 0.098
43.0	194.0	−121.7	6.25 ± 0.37	−0.054 ± 0.090
43.0	202.0	−105.8	7.35 ± 0.32	0.117 ± 0.063
43.0	206.0	−97.9	7.09 ± 0.32	0.056 ± 0.065
43.0	210.0	−90.0	8.59 ± 0.34	0.032 ± 0.058
43.0	214.0	−82.1	8.48 ± 0.31	0.086 ± 0.052
43.0	218.0	−74.4	8.76 ± 0.32	−0.007 ± 0.052
43.0	222.0	−66.8	9.69 ± 0.33	0.078 ± 0.048
43.0	226.0	−59.4	9.23 ± 0.33	0.050 ± 0.051
43.0	230.0	−52.3	9.28 ± 0.26	0.094 ± 0.045
43.0	234.0	−45.7	8.67 ± 0.26	0.000 ± 0.048
43.0	238.0	−39.9	8.75 ± 0.27	0.056 ± 0.048

Table D.4 *(Continued)*

E_{sep} (MeV)	E_1 (MeV)	p_3 (MeV/c)	$\frac{d\sigma}{d\Omega_1 d\Omega_2 dE_1}$ (μb/sr^2 MeV)	A_y
45.0	186.0	−134.6	4.84 ± 0.35	0.296 ± 0.109
45.0	190.0	−126.5	4.95 ± 0.35	0.195 ± 0.105
45.0	194.0	−118.4	6.70 ± 0.37	0.147 ± 0.084
45.0	202.0	−102.3	6.52 ± 0.31	0.017 ± 0.069
45.0	206.0	−94.3	7.16 ± 0.32	0.083 ± 0.066
45.0	210.0	−86.3	7.44 ± 0.32	−0.024 ± 0.064
45.0	214.0	−78.3	8.03 ± 0.31	0.038 ± 0.055
45.0	218.0	−70.4	8.51 ± 0.31	0.038 ± 0.053
45.0	222.0	−62.7	9.02 ± 0.32	0.003 ± 0.051
45.0	226.0	−55.2	8.94 ± 0.33	0.056 ± 0.052
45.0	230.0	−48.0	9.34 ± 0.26	0.019 ± 0.044
45.0	234.0	−41.3	8.82 ± 0.26	0.052 ± 0.047
45.0	238.0	−35.5	9.35 ± 0.27	0.020 ± 0.045
47.0	186.0	−131.5	4.89 ± 0.35	0.116 ± 0.108
47.0	190.0	−123.3	5.04 ± 0.35	−0.049 ± 0.106
47.0	194.0	−115.1	5.93 ± 0.37	0.099 ± 0.094
47.0	202.0	−98.8	6.30 ± 0.31	0.267 ± 0.072
47.0	206.0	−90.7	6.72 ± 0.31	−0.034 ± 0.069
47.0	210.0	−82.6	7.77 ± 0.33	0.075 ± 0.062
47.0	214.0	−74.5	8.11 ± 0.31	0.022 ± 0.054
47.0	218.0	−66.5	7.63 ± 0.31	−0.092 ± 0.058
47.0	222.0	−58.6	8.95 ± 0.32	0.059 ± 0.051
47.0	226.0	−50.9	9.31 ± 0.33	−0.032 ± 0.051
47.0	230.0	−43.6	8.81 ± 0.26	−0.018 ± 0.047
47.0	234.0	−36.8	9.02 ± 0.27	−0.009 ± 0.047
47.0	238.0	−31.1	8.72 ± 0.26	0.084 ± 0.048

Table D.4 *(Continued)*

E_{sep} (MeV)	E_1 (MeV)	p_3 (MeV/c)	$\frac{d\sigma}{d\Omega_1 d\Omega_2 dE_1}$ (μb/sr^2 MeV)	A_y
49.0	186.0	−128.3	5.44 ± 0.36	0.092 ± 0.098
49.0	190.0	−120.1	4.80 ± 0.35	0.102 ± 0.110
49.0	194.0	−111.9	5.47 ± 0.36	0.023 ± 0.100
49.0	202.0	−95.4	6.27 ± 0.31	0.107 ± 0.071
49.0	206.0	−87.1	7.08 ± 0.32	0.092 ± 0.066
49.0	210.0	−78.9	6.85 ± 0.32	−0.002 ± 0.069
49.0	214.0	−70.7	6.94 ± 0.30	0.092 ± 0.062
49.0	218.0	−62.6	8.34 ± 0.31	0.066 ± 0.054
49.0	222.0	−54.5	8.36 ± 0.32	0.058 ± 0.054
49.0	226.0	−46.7	8.86 ± 0.33	0.046 ± 0.053
49.0	230.0	−39.2	8.56 ± 0.26	0.110 ± 0.048
49.0	234.0	−32.4	8.59 ± 0.26	0.096 ± 0.048
49.0	238.0	−26.7	8.72 ± 0.27	0.096 ± 0.048
51.0	186.0	−125.3	4.30 ± 0.34	−0.056 ± 0.120
51.0	190.0	−116.9	4.98 ± 0.35	−0.098 ± 0.107
51.0	194.0	−108.6	5.34 ± 0.36	0.132 ± 0.101
51.0	202.0	−91.9	5.95 ± 0.30	−0.038 ± 0.075
51.0	206.0	−83.6	6.71 ± 0.32	0.011 ± 0.069
51.0	210.0	−75.3	6.77 ± 0.32	0.124 ± 0.069
51.0	214.0	−66.9	7.20 ± 0.30	0.117 ± 0.059
51.0	218.0	−58.7	8.29 ± 0.32	0.093 ± 0.054
51.0	222.0	−50.5	8.26 ± 0.32	0.051 ± 0.055
51.0	226.0	−42.4	9.08 ± 0.33	0.126 ± 0.052
51.0	230.0	−34.8	8.03 ± 0.26	0.019 ± 0.051
51.0	234.0	−27.9	8.58 ± 0.26	−0.031 ± 0.049
51.0	238.0	−22.4	8.39 ± 0.27	0.102 ± 0.050

Table D.4 *(Continued)*

E_{sep} (MeV)	E_1 (MeV)	p_3 (MeV/c)	$\frac{d\sigma}{d\Omega_1 d\Omega_2 dE_1}$ (μb/sr^2 MeV)	A_y
53.0	186.0	−122.2	4.82 ± 0.35	0.015 ± 0.111
53.0	190.0	−113.8	4.70 ± 0.35	−0.001 ± 0.113
53.0	194.0	−105.4	4.63 ± 0.35	−0.075 ± 0.114
53.0	202.0	−88.5	5.08 ± 0.30	0.034 ± 0.086
53.0	206.0	−80.1	6.07 ± 0.31	0.031 ± 0.076
53.0	210.0	−71.6	6.35 ± 0.32	0.074 ± 0.073
53.0	214.0	−63.2	7.45 ± 0.30	0.044 ± 0.058
53.0	218.0	−54.8	7.42 ± 0.30	−0.014 ± 0.059
53.0	222.0	−46.4	8.00 ± 0.32	−0.024 ± 0.056
53.0	226.0	−38.2	8.26 ± 0.32	0.020 ± 0.056
53.0	230.0	−30.4	7.91 ± 0.26	0.038 ± 0.051
53.0	234.0	−23.3	8.51 ± 0.26	0.063 ± 0.049
53.0	238.0	−18.1	7.95 ± 0.26	0.016 ± 0.053
55.0	186.0	−119.2	4.08 ± 0.34	0.183 ± 0.125
55.0	190.0	−110.7	4.66 ± 0.35	−0.070 ± 0.113
55.0	194.0	−102.2	4.77 ± 0.35	−0.038 ± 0.110
55.0	202.0	−85.2	5.12 ± 0.30	0.083 ± 0.086
55.0	206.0	−76.6	4.99 ± 0.30	−0.002 ± 0.088
55.0	210.0	−68.1	6.60 ± 0.32	0.044 ± 0.071
55.0	214.0	−59.5	7.01 ± 0.30	0.070 ± 0.061
55.0	218.0	−50.9	7.47 ± 0.31	−0.005 ± 0.059
55.0	222.0	−42.4	7.37 ± 0.31	0.033 ± 0.060
55.0	226.0	−34.0	8.08 ± 0.32	0.087 ± 0.056
55.0	230.0	−25.9	7.70 ± 0.26	−0.080 ± 0.053
55.0	234.0	−18.7	7.79 ± 0.26	0.122 ± 0.053
55.0	238.0	−14.1	7.79 ± 0.26	0.016 ± 0.054

Table D.4 *(Continued)*

E_{sep} (MeV)	E_1 (MeV)	p_3 (MeV/c)	$\frac{d\sigma}{d\Omega_1 d\Omega_2 dE_1}$ (μb/sr^2 MeV)	A_y
57.0	186.0	−116.2	3.74 ± 0.33	−0.038 ± 0.135
57.0	190.0	−107.6	4.34 ± 0.34	−0.134 ± 0.120
57.0	194.0	−99.1	4.43 ± 0.35	0.125 ± 0.119
57.0	202.0	−81.9	5.08 ± 0.30	0.237 ± 0.085
57.0	206.0	−73.2	5.48 ± 0.31	0.068 ± 0.082
57.0	210.0	−64.5	6.15 ± 0.32	0.050 ± 0.075
57.0	214.0	−55.8	5.90 ± 0.29	0.016 ± 0.070
57.0	218.0	−47.1	7.23 ± 0.30	−0.103 ± 0.061
57.0	222.0	−38.4	7.03 ± 0.31	0.029 ± 0.063
57.0	226.0	−29.7	7.64 ± 0.32	0.076 ± 0.059
57.0	230.0	−21.4	6.60 ± 0.25	0.041 ± 0.060
57.0	234.0	−14.1	7.06 ± 0.26	0.032 ± 0.058
57.0	238.0	10.5	7.39 ± 0.26	0.081 ± 0.056
59.0	186.0	−113.2	3.90 ± 0.34	0.007 ± 0.131
59.0	190.0	−104.6	4.05 ± 0.34	−0.011 ± 0.127
59.0	194.0	−96.0	4.21 ± 0.34	0.083 ± 0.123
59.0	202.0	−78.6	4.17 ± 0.29	0.138 ± 0.102
59.0	206.0	−69.9	5.10 ± 0.30	0.071 ± 0.086
59.0	210.0	−61.1	5.38 ± 0.31	−0.097 ± 0.084
59.0	214.0	−52.2	6.02 ± 0.29	−0.028 ± 0.070
59.0	218.0	−43.3	6.68 ± 0.30	0.050 ± 0.064
59.0	222.0	−34.4	6.41 ± 0.30	−0.094 ± 0.068
59.0	226.0	−25.6	7.04 ± 0.31	−0.044 ± 0.063
59.0	230.0	−17.0	6.59 ± 0.25	−0.032 ± 0.060
59.0	234.0	−9.5	6.88 ± 0.25	−0.032 ± 0.059
59.0	238.0	8.2	6.93 ± 0.26	0.079 ± 0.059

Table D.4 *(Continued)*

E_{sep} (MeV)	E_1 (MeV)	p_3 (MeV/c)	$\frac{d\sigma}{d\Omega_1 d\Omega_2 dE_1}$ (μb/sr^2 MeV)	A_y
61.0	186.0	−110.3	3.99 ± 0.34	0.033 ± 0.130
61.0	190.0	−101.7	4.39 ± 0.35	0.138 ± 0.118
61.0	194.0	−93.0	4.66 ± 0.35	0.085 ± 0.114
61.0	202.0	−75.4	5.32 ± 0.30	0.110 ± 0.082
61.0	206.0	−66.6	5.95 ± 0.31	0.146 ± 0.075
61.0	210.0	−57.7	5.33 ± 0.30	0.023 ± 0.084
61.0	214.0	−48.7	6.01 ± 0.29	0.014 ± 0.070
61.0	218.0	−39.7	6.12 ± 0.30	0.108 ± 0.069
61.0	222.0	−30.6	6.21 ± 0.30	0.053 ± 0.069
61.0	226.0	−21.5	6.71 ± 0.31	0.075 ± 0.065
61.0	230.0	−12.6	6.03 ± 0.25	−0.072 ± 0.065
61.0	234.0	−4.9	6.27 ± 0.25	0.049 ± 0.063
61.0	238.0	8.4	5.97 ± 0.25	0.045 ± 0.067
63.0	186.0	−107.5	3.71 ± 0.34	−0.241 ± 0.139
63.0	190.0	−98.8	4.09 ± 0.34	0.033 ± 0.126
63.0	194.0	−90.0	4.44 ± 0.35	0.107 ± 0.118
63.0	202.0	−72.3	3.99 ± 0.29	−0.161 ± 0.107
63.0	206.0	−63.4	5.11 ± 0.30	−0.026 ± 0.086
63.0	210.0	−54.4	5.24 ± 0.30	−0.009 ± 0.085
63.0	214.0	−45.4	5.73 ± 0.29	−0.037 ± 0.072
63.0	218.0	−36.2	5.15 ± 0.29	−0.021 ± 0.079
63.0	222.0	−27.0	5.88 ± 0.30	0.112 ± 0.072
63.0	226.0	−17.7	5.99 ± 0.30	0.081 ± 0.072
63.0	230.0	−8.4	5.98 ± 0.25	−0.002 ± 0.066
63.0	234.0	1.7	5.51 ± 0.25	0.075 ± 0.071
63.0	238.0	10.9	5.61 ± 0.25	−0.020 ± 0.072

Table D.4 *(Continued)*

E_{sep} (MeV)	E_1 (MeV)	p_3 (MeV/c)	$\frac{d\sigma}{d\Omega_1 d\Omega_2 dE_1}$ (μb/sr^2 MeV)	A_y
65.0	186.0	−104.7	3.78 ± 0.33	0.085 ± 0.133
65.0	190.0	−95.9	3.92 ± 0.34	0.124 ± 0.130
65.0	194.0	−87.1	4.31 ± 0.35	0.039 ± 0.121
65.0	202.0	−69.3	4.42 ± 0.29	−0.038 ± 0.096
65.0	206.0	−60.3	4.74 ± 0.30	0.151 ± 0.092
65.0	210.0	−51.3	4.27 ± 0.29	0.109 ± 0.101
65.0	214.0	−42.2	5.61 ± 0.29	−0.033 ± 0.074
65.0	218.0	−33.0	5.52 ± 0.29	0.201 ± 0.075
65.0	222.0	−23.7	5.82 ± 0.29	0.084 ± 0.072
65.0	226.0	−14.4	5.70 ± 0.30	0.077 ± 0.074
65.0	230.0	−5.1	4.86 ± 0.24	−0.097 ± 0.079
65.0	234.0	5.3	4.72 ± 0.24	−0.055 ± 0.081
65.0	238.0	14.7	4.50 ± 0.24	0.084 ± 0.086
67.0	186.0	−102.0	3.40 ± 0.33	0.244 ± 0.148
67.0	190.0	−93.1	3.35 ± 0.33	0.181 ± 0.150
67.0	194.0	−84.3	3.99 ± 0.34	−0.097 ± 0.129
67.0	202.0	−66.4	3.89 ± 0.28	−0.048 ± 0.107
67.0	206.0	−57.4	4.05 ± 0.29	−0.039 ± 0.105
67.0	210.0	−48.3	4.47 ± 0.30	0.092 ± 0.097
67.0	214.0	−39.2	5.14 ± 0.28	−0.029 ± 0.079
67.0	218.0	−30.0	4.68 ± 0.29	0.004 ± 0.087
67.0	222.0	−20.8	5.69 ± 0.29	0.125 ± 0.073
67.0	226.0	−11.8	5.04 ± 0.29	0.124 ± 0.082
67.0	230.0	−5.2	4.58 ± 0.24	−0.079 ± 0.083
67.0	234.0	10.0	4.80 ± 0.24	0.045 ± 0.080
67.0	238.0	19.1	4.27 ± 0.24	−0.022 ± 0.090

Table D.4 *(Continued)*

E_{sep} (MeV)	E_1 (MeV)	p_3 (MeV/c)	$\frac{d\sigma}{d\Omega_1 d\Omega_2 dE_1}$ (μb/sr^2 MeV)	A_y
69.0	186.0	−99.3	3.19 ± 0.34	0.358 ± 0.159
69.0	190.0	−90.5	3.08 ± 0.33	0.389 ± 0.162
69.0	194.0	−81.6	3.44 ± 0.33	0.160 ± 0.146
69.0	202.0	−63.6	3.71 ± 0.29	−0.037 ± 0.113
69.0	206.0	−54.6	4.02 ± 0.29	0.021 ± 0.106
69.0	210.0	−45.5	4.28 ± 0.29	0.039 ± 0.099
69.0	214.0	−36.5	4.72 ± 0.28	0.132 ± 0.084
69.0	218.0	−27.4	4.73 ± 0.28	0.057 ± 0.086
69.0	222.0	−18.6	4.80 ± 0.29	−0.137 ± 0.086
69.0	226.0	−10.9	5.13 ± 0.29	0.066 ± 0.081
69.0	230.0	8.6	4.27 ± 0.24	−0.102 ± 0.089
69.0	234.0	14.8	4.12 ± 0.24	−0.021 ± 0.091
69.0	238.0	23.8	4.09 ± 0.24	−0.058 ± 0.094
71.0	186.0	−96.8	3.64 ± 0.33	0.012 ± 0.138
71.0	190.0	−87.9	3.11 ± 0.33	0.083 ± 0.159
71.0	194.0	−79.0	3.46 ± 0.33	−0.132 ± 0.142
71.0	202.0	−61.0	3.85 ± 0.28	0.013 ± 0.108
71.0	206.0	−52.0	3.76 ± 0.29	0.116 ± 0.111
71.0	210.0	−43.0	3.62 ± 0.29	−0.039 ± 0.116
71.0	214.0	−34.1	4.41 ± 0.28	−0.029 ± 0.091
71.0	218.0	−25.4	4.32 ± 0.28	−0.117 ± 0.092
71.0	222.0	−17.4	4.81 ± 0.28	−0.017 ± 0.084
71.0	226.0	−11.9	4.01 ± 0.28	0.034 ± 0.099
71.0	230.0	13.0	4.18 ± 0.24	0.073 ± 0.089
71.0	234.0	19.8	4.15 ± 0.24	−0.102 ± 0.092
71.0	238.0	28.6	3.55 ± 0.23	0.017 ± 0.104

Table D.4 *(Continued)*

E_{sep} (MeV)	E_1 (MeV)	p_3 (MeV/c)	$\frac{d\sigma}{d\Omega_1 d\Omega_2 dE_1}$ (μb/sr^2 MeV)	A_y
73.0	186.0	−94.3	2.75 ± 0.32	−0.129 ± 0.174
73.0	190.0	−85.4	3.07 ± 0.33	0.306 ± 0.160
73.0	194.0	−76.5	3.47 ± 0.33	0.089 ± 0.145
73.0	202.0	−58.6	2.90 ± 0.28	−0.064 ± 0.140
73.0	206.0	−49.7	3.59 ± 0.28	0.180 ± 0.116
73.0	210.0	−40.8	4.15 ± 0.29	−0.076 ± 0.102
73.0	214.0	−32.2	3.96 ± 0.27	0.023 ± 0.099
73.0	218.0	−24.1	4.10 ± 0.28	0.182 ± 0.097
73.0	222.0	−17.4	3.88 ± 0.28	−0.031 ± 0.103
73.0	226.0	−14.5	3.86 ± 0.28	0.122 ± 0.102
73.0	230.0	17.6	3.68 ± 0.23	−0.052 ± 0.101
73.0	234.0	24.7	3.33 ± 0.23	0.262 ± 0.111
73.0	238.0	33.5	3.08 ± 0.23	−0.134 ± 0.121

Table D.5: Data table for the ^{40}Ca$(\vec{p}, 2p)$ reaction at the set4 in Table 2.1. ΔE_{sep} = 2 MeV.

E_{sep} (MeV)	E_1 (MeV)	p_3 (MeV/c)	$\frac{d\sigma}{d\Omega_1 d\Omega_2 dE_1}$ (μb/sr^2 MeV)	A_y
59.0	174.0	−119.0	3.36 ± 0.27	0.165 ± 0.114
59.0	178.0	−111.1	3.74 ± 0.27	0.074 ± 0.105
59.0	186.0	−95.3	4.19 ± 0.29	0.094 ± 0.098
59.0	190.0	−87.5	4.35 ± 0.29	−0.092 ± 0.095
59.0	194.0	−79.7	4.52 ± 0.29	0.034 ± 0.093
59.0	202.0	−64.2	4.82 ± 0.28	0.085 ± 0.086
59.0	206.0	−56.6	4.97 ± 0.29	0.146 ± 0.085
59.0	210.0	−49.2	5.98 ± 0.30	−0.005 ± 0.074
59.0	214.0	−42.2	4.76 ± 0.18	0.061 ± 0.134
59.0	218.0	−35.7	5.18 ± 0.18	0.134 ± 0.057
59.0	222.0	−30.2	5.01 ± 0.18	0.076 ± 0.059
59.0	226.0	−26.4	5.60 ± 0.19	−0.039 ± 0.055
61.0	174.0	−115.9	3.48 ± 0.27	0.039 ± 0.111
61.0	178.0	−108.0	3.67 ± 0.27	−0.116 ± 0.106
61.0	186.0	−92.0	3.94 ± 0.28	0.112 ± 0.102
61.0	190.0	−84.1	3.82 ± 0.28	−0.086 ± 0.106
61.0	194.0	−76.1	4.07 ± 0.29	0.108 ± 0.101
61.0	202.0	−60.4	4.54 ± 0.28	0.102 ± 0.090
61.0	206.0	−52.7	4.94 ± 0.29	−0.041 ± 0.085
61.0	210.0	−45.1	4.84 ± 0.29	−0.036 ± 0.088
61.0	214.0	−37.9	4.52 ± 0.18	−0.028 ± 0.063
61.0	218.0	−31.3	5.00 ± 0.18	−0.020 ± 0.058
61.0	222.0	−25.8	5.07 ± 0.18	0.022 ± 0.058
61.0	226.0	−22.5	5.21 ± 0.19	−0.072 ± 0.058

Table D.5 *(Continued)*

E_{sep} (MeV)	E_1 (MeV)	p_3 (MeV/c)	$\frac{d\sigma}{d\Omega_1 d\Omega_2 dE_1}$ (μb/sr^2 MeV)	A_y
63.0	174.0	−112.9	3.23 ± 0.27	0.049 ± 0.118
63.0	178.0	−104.9	3.73 ± 0.27	0.001 ± 0.103
63.0	186.0	−88.7	4.24 ± 0.29	−0.032 ± 0.097
63.0	190.0	−80.7	4.19 ± 0.28	0.169 ± 0.097
63.0	194.0	−72.6	4.54 ± 0.30	0.072 ± 0.093
63.0	202.0	−56.6	4.11 ± 0.28	−0.160 ± 0.099
63.0	206.0	−48.7	4.84 ± 0.29	0.081 ± 0.086
63.0	210.0	−41.0	5.05 ± 0.29	−0.012 ± 0.085
63.0	214.0	−33.6	4.70 ± 0.18	−0.064 ± 0.061
63.0	218.0	−26.8	4.53 ± 0.18	0.052 ± 0.063
63.0	222.0	−21.5	5.09 ± 0.18	0.071 ± 0.058
63.0	226.0	18.9	4.77 ± 0.18	−0.059 ± 0.063
65.0	174.0	−110.0	3.13 ± 0.27	0.082 ± 0.121
65.0	178.0	−101.8	3.01 ± 0.26	0.043 ± 0.125
65.0	186.0	−85.5	3.32 ± 0.28	−0.027 ± 0.120
65.0	190.0	−77.3	4.01 ± 0.28	−0.021 ± 0.102
65.0	194.0	−69.1	4.55 ± 0.29	0.141 ± 0.091
65.0	202.0	−52.8	4.06 ± 0.27	0.088 ± 0.097
65.0	206.0	−44.8	4.65 ± 0.29	−0.003 ± 0.090
65.0	210.0	−36.9	4.99 ± 0.29	−0.111 ± 0.086
65.0	214.0	−29.2	3.97 ± 0.17	0.033 ± 0.070
65.0	218.0	−22.4	4.42 ± 0.18	0.004 ± 0.065
65.0	222.0	−17.2	4.23 ± 0.18	−0.022 ± 0.069
65.0	226.0	15.7	4.49 ± 0.18	0.029 ± 0.066

Table D.5 *(Continued)*

E_{sep} (MeV)	E_1 (MeV)	p_3 (MeV/c)	$\frac{d\sigma}{d\Omega_1 d\Omega_2 dE_1}$ (μb/sr^2 MeV)	A_y
67.0	174.0	−107.0	2.61 ± 0.26	0.081 ± 0.143
67.0	178.0	−98.8	3.00 ± 0.27	−0.043 ± 0.128
67.0	186.0	−82.3	3.74 ± 0.28	−0.064 ± 0.108
67.0	190.0	−74.0	4.16 ± 0.29	−0.184 ± 0.099
67.0	194.0	−65.7	4.19 ± 0.29	−0.102 ± 0.100
67.0	202.0	−49.1	4.19 ± 0.28	−0.084 ± 0.098
67.0	206.0	−40.9	4.30 ± 0.29	0.090 ± 0.097
67.0	210.0	−32.8	3.82 ± 0.28	0.152 ± 0.108
67.0	214.0	−24.9	3.72 ± 0.17	0.087 ± 0.074
67.0	218.0	−17.8	4.30 ± 0.18	0.006 ± 0.066
67.0	222.0	−13.0	4.26 ± 0.18	0.068 ± 0.068
67.0	226.0	13.4	3.86 ± 0.18	−0.002 ± 0.075
69.0	174.0	−104.1	2.73 ± 0.26	−0.223 ± 0.138
69.0	178.0	−95.8	3.17 ± 0.26	0.066 ± 0.119
69.0	186.0	−79.2	3.77 ± 0.28	0.014 ± 0.107
69.0	190.0	−70.8	2.89 ± 0.27	−0.129 ± 0.135
69.0	194.0	−62.4	3.75 ± 0.28	0.025 ± 0.107
69.0	202.0	−45.5	4.17 ± 0.28	−0.007 ± 0.099
69.0	206.0	−37.1	4.27 ± 0.29	−0.046 ± 0.097
69.0	210.0	−28.7	4.14 ± 0.29	−0.017 ± 0.101
69.0	214.0	−20.6	3.53 ± 0.17	0.062 ± 0.077
69.0	218.0	−13.3	3.58 ± 0.17	−0.109 ± 0.077
69.0	222.0	9.3	3.60 ± 0.17	0.009 ± 0.078
69.0	226.0	12.6	3.76 ± 0.18	0.066 ± 0.077

Table D.5 *(Continued)*

E_{sep} (MeV)	E_1 (MeV)	p_3 (MeV/c)	$\frac{d\sigma}{d\Omega_1 d\Omega_2 dE_1}$ (μb/sr^2 MeV)	A_y
71.0	174.0	−101.3	2.89 ± 0.27	−0.043 ± 0.132
71.0	178.0	−92.9	3.12 ± 0.27	0.272 ± 0.124
71.0	186.0	−76.1	3.31 ± 0.27	0.042 ± 0.118
71.0	190.0	−67.6	3.20 ± 0.28	−0.104 ± 0.123
71.0	194.0	−59.1	3.89 ± 0.28	−0.068 ± 0.105
71.0	202.0	−42.0	4.50 ± 0.28	−0.021 ± 0.091
71.0	206.0	−33.4	3.68 ± 0.28	0.002 ± 0.109
71.0	210.0	−24.8	3.34 ± 0.27	−0.183 ± 0.120
71.0	214.0	−16.3	3.46 ± 0.17	−0.103 ± 0.079
71.0	218.0	−8.7	3.39 ± 0.17	−0.079 ± 0.081
71.0	222.0	6.7	3.38 ± 0.17	0.065 ± 0.082
71.0	226.0	13.4	3.54 ± 0.18	0.042 ± 0.080
73.0	174.0	−98.5	2.71 ± 0.26	0.198 ± 0.139
73.0	178.0	−90.1	3.13 ± 0.27	0.117 ± 0.122
73.0	186.0	−73.1	3.36 ± 0.28	0.018 ± 0.121
73.0	190.0	−64.6	3.67 ± 0.28	−0.077 ± 0.111
73.0	194.0	−56.0	3.03 ± 0.27	−0.097 ± 0.129
73.0	202.0	−38.6	3.69 ± 0.27	−0.047 ± 0.106
73.0	206.0	−29.9	3.78 ± 0.28	0.054 ± 0.108
73.0	210.0	−21.1	3.19 ± 0.28	−0.241 ± 0.128
73.0	214.0	−12.3	3.36 ± 0.17	−0.168 ± 0.081
73.0	218.0	−4.0	3.05 ± 0.17	0.144 ± 0.089
73.0	222.0	6.9	3.21 ± 0.17	0.031 ± 0.086
73.0	226.0	15.8	3.20 ± 0.17	−0.047 ± 0.088

E_{sep} (MeV)	E_1 (MeV)	p_3 (MeV/c)	$\frac{d\sigma}{d\Omega_1 d\Omega_2 dE_1}$ (μb/sr^2 MeV)	A_y
75.0	174.0	−95.9	2.25 ± 0.25	−0.200 ± 0.162
75.0	178.0	−87.4	2.68 ± 0.26	−0.042 ± 0.138
75.0	186.0	−70.3	3.39 ± 0.28	0.037 ± 0.117
75.0	190.0	−61.6	3.26 ± 0.27	0.136 ± 0.120
75.0	194.0	−53.0	3.33 ± 0.27	0.182 ± 0.118
75.0	202.0	−35.4	2.72 ± 0.27	−0.077 ± 0.141
75.0	206.0	−26.6	3.36 ± 0.28	−0.192 ± 0.121
75.0	210.0	−17.6	3.36 ± 0.28	0.075 ± 0.119
75.0	214.0	−8.6	3.10 ± 0.17	0.027 ± 0.087
75.0	218.0	0.7	3.11 ± 0.17	−0.045 ± 0.088
75.0	222.0	9.8	2.74 ± 0.17	−0.044 ± 0.099
75.0	226.0	19.1	3.13 ± 0.17	0.018 ± 0.089
77.0	174.0	−93.2	2.51 ± 0.26	−0.085 ± 0.147
77.0	178.0	−84.7	2.56 ± 0.26	0.001 ± 0.143
77.0	186.0	−67.5	2.96 ± 0.27	0.026 ± 0.130
77.0	190.0	−58.8	2.90 ± 0.27	−0.202 ± 0.136
77.0	194.0	−50.1	3.20 ± 0.28	−0.001 ± 0.124
77.0	202.0	−32.5	3.15 ± 0.27	0.035 ± 0.125
77.0	206.0	−23.7	2.78 ± 0.27	0.006 ± 0.142
77.0	210.0	−14.8	2.97 ± 0.27	0.086 ± 0.135
77.0	214.0	−6.4	2.89 ± 0.17	−0.129 ± 0.093
77.0	218.0	5.4	2.76 ± 0.17	−0.021 ± 0.097
77.0	222.0	13.8	2.84 ± 0.17	0.023 ± 0.095
77.0	226.0	23.1	2.77 ± 0.17	−0.060 ± 0.101

E_{sep} (MeV)	E_1 (MeV)	p_3 (MeV/c)	$\frac{d\sigma}{d\Omega_1 d\Omega_2 dE_1}$ (μb/sr^2 MeV)	A_y
79.0	174.0	−90.7	2.31 ± 0.26	0.103 ± 0.159
79.0	178.0	−82.1	3.13 ± 0.26	−0.043 ± 0.120
79.0	186.0	−64.9	2.87 ± 0.27	0.001 ± 0.135
79.0	190.0	−56.2	2.85 ± 0.27	0.051 ± 0.136
79.0	194.0	−47.4	3.01 ± 0.27	0.315 ± 0.131
79.0	202.0	−29.9	2.78 ± 0.27	0.058 ± 0.142
79.0	206.0	−21.3	2.59 ± 0.27	0.070 ± 0.149
79.0	210.0	−13.0	2.79 ± 0.27	0.127 ± 0.143
79.0	214.0	−7.1	2.69 ± 0.16	−0.082 ± 0.099
79.0	218.0	10.1	2.64 ± 0.16	−0.057 ± 0.101
79.0	222.0	18.3	2.57 ± 0.17	−0.056 ± 0.105
79.0	226.0	27.4	2.63 ± 0.17	0.022 ± 0.103
81.0	174.0	−88.3	2.78 ± 0.26	0.109 ± 0.135
81.0	178.0	−79.7	2.51 ± 0.26	−0.012 ± 0.148
81.0	186.0	−62.4	2.55 ± 0.27	0.055 ± 0.151
81.0	190.0	−53.7	2.76 ± 0.27	0.137 ± 0.142
81.0	194.0	−45.0	2.51 ± 0.27	−0.069 ± 0.153
81.0	202.0	−27.8	2.51 ± 0.27	0.122 ± 0.155
81.0	206.0	−19.6	2.52 ± 0.27	0.327 ± 0.154
81.0	210.0	−12.6	2.37 ± 0.27	0.219 ± 0.158
81.0	214.0	10.2	2.45 ± 0.16	−0.037 ± 0.106
81.0	218.0	14.9	2.47 ± 0.17	−0.014 ± 0.108
81.0	222.0	22.9	2.31 ± 0.16	−0.138 ± 0.116
81.0	226.0	31.9	2.76 ± 0.17	−0.002 ± 0.099

Table D.5 *(Continued)*

Table D.5 *(Continued)*

E_{sep} (MeV)	E_1 (MeV)	p_3 (MeV/c)	$\frac{d\sigma}{d\Omega_1 d\Omega_2 dE_1}$ (μb/sr^2 MeV)	A_y
83.0	174.0	−86.0	1.90 ± 0.25	0.092 ± 0.190
83.0	178.0	−77.4	2.34 ± 0.26	0.007 ± 0.157
83.0	186.0	−60.1	3.36 ± 0.28	−0.007 ± 0.118
83.0	190.0	−51.5	2.89 ± 0.27	−0.150 ± 0.135
83.0	194.0	−42.9	2.76 ± 0.27	−0.103 ± 0.140
83.0	202.0	−26.3	2.40 ± 0.26	0.205 ± 0.153
83.0	206.0	−19.0	2.56 ± 0.27	−0.054 ± 0.149
83.0	210.0	−14.0	3.04 ± 0.27	0.007 ± 0.127
83.0	214.0	14.3	2.27 ± 0.16	0.058 ± 0.114
83.0	218.0	19.8	2.30 ± 0.16	0.213 ± 0.115
83.0	222.0	27.7	2.24 ± 0.16	0.070 ± 0.119
83.0	226.0	36.6	2.34 ± 0.16	0.015 ± 0.114
85.0	174.0	−83.8	2.79 ± 0.26	0.034 ± 0.134
85.0	178.0	−75.2	2.37 ± 0.25	0.108 ± 0.153
85.0	186.0	−58.0	2.53 ± 0.27	0.034 ± 0.153
85.0	190.0	−49.5	3.26 ± 0.27	−0.008 ± 0.120
85.0	194.0	−41.1	2.86 ± 0.27	−0.047 ± 0.135
85.0	202.0	−25.5	2.84 ± 0.27	0.101 ± 0.136
85.0	206.0	−19.4	2.44 ± 0.26	−0.079 ± 0.155
85.0	210.0	−16.6	1.94 ± 0.26	0.343 ± 0.203
85.0	214.0	18.7	2.11 ± 0.16	0.203 ± 0.122
85.0	218.0	24.7	2.41 ± 0.16	0.099 ± 0.109
85.0	222.0	32.6	2.03 ± 0.16	0.212 ± 0.129
85.0	226.0	41.4	2.05 ± 0.16	0.231 ± 0.128

Bibliography

[1] T. Otsuka, R. Fujimoto, Y. Utsuno, B. A. Brown, M. Honma, and T. Mizusaki, Phys. Rev. Lett. **87**, 082502 (2001)

[2] T. Otsuka, T. Suzuki, R. Fujimoto, H. Grawe, and Y. Akaishi, Phys. Rev. Lett. **95**, 232502 (2005)

[3] R. Jastrow, Phys. Rev. **98**, 1479 (1955)

[4] J. G. Zabolitzky and W. Ey, Physics Letters B **76**, 527 (1978)

[5] O. Bohigas and S. Stringari, Physics Letters B **95**, 9 (1980)

[6] M. Dal Ri, S. Stringari, and O. Bohigas, Nuclear Physics A **376**, 81 (1982)

[7] F. Dellagiacoma, G. Orlandini, and M. Traini, Nuclear Physics A **393**, 95 (1983)

[8] M. Jaminon, C. Mahaux, and H. Ngt, Nuclear Physics A **473**, 509 (1987)

[9] P. Doll, G. J. Wagner, K. T. Knvpfle, and G. Mairle, Nuclear Physics A **263**, 210 (1976)

[10] A. E. L. Dieperink and P. K. A. Huberts, Annual Review of Nuclear and Particle Science **40**, 239 (1990)

[11] L. Lapikás, Nuclear Physics A **553**, 297c (1993)

[12] O. Benhar, A. Fabrocini, and S. Fantoni, Phys. Rev. C **41**, R24 (1990)

[13] A. Fabrocini and G. Co', Phys. Rev. C **63**, 044319 (2001)

[14] C. Bisconti, F. A. d. Saavedra, and G. Co', Phys. Rev. C **75**, 054302 (2007)

[15] G. JACOB and T. A. J. MARIS, Rev. Mod. Phys. **45**, 6 (1973)

[16] J. Mougey, M. Bernheim, A. A. Bussière, A. Gillebert, P. X. Hô, M. Priou, D. Royer, I. Sick, and G. J. Wagner, Nuclear Physics A **262**, 461 (1976)

[17] K. Nakamura, S. Hiramatsu, T. Kamae, H. Muramatsu, N. Izutsu, and Y. Watase, Phys. Rev. Lett. **33**, 853 (1974)

[18] K. Nakamura, S. Hiramatsu, T. Kamae, H. Muramatsu, N. Izutsu, and Y. Watase, Nuclear Physics A **271**, 221 (1976)

[19] U. Amaldi Jr., G. C. Venuti, G. Cortellessa, E. D. Sanctis, S. Frullani, R. Lombard, and P. Salvadori, Physics Letters **22**, 593 (1966)

[20] A. N. James, P. T. Andrews, P. Kirkby, and B. G. Lowe, Nuclear Physics A **138**, 145 (1969)

[21] S. Kullander, F. Lemeilleur, P. Renberg, G. Landaud, J. Yonnet, B. Fagerstrvm, A. Johansson, and G. Tibell, Nuclear Physics A **173**, 357 (1971)

[22] S. S. Volkov, A. A. Vorob'ev, O. A. Domchenkov, Y. V. Dotsenko, N. P. Kuropatkin, A. A. Lobodenko, O. V. Miklukho, V. N. Nikulin, V. E. Stradubsky, A. Y. Tsaregorodtsev, Z. A. Chakhalyan, and Y. A. Shcheglov, Soviet Journal of Nuclear Physics **52**, 848 (1990)

[23] A. A. Vorob'ev, Y. V. Dotsenko, A. A. Lobodenko, O. V. Miklukho, I. I. Tkach, A. Y. Tsaregorodtsev, and Y. A. Shcheglov, Physics of Atomic Nuclei **58**, 1817 (1995)

[24] R. A. Niyazov, L. B. Weinstein, G. Adams, P. Ambrozewicz, E. Anciant, M. Anghinolfi, B. Asavapibhop, G. Asryan, G. Audit, T. Auger, H. Avakian, H. Bagdasaryan, J. P. Ball, S. Barrow, M. Battaglieri, K. Beard, M. Bektasoglu, M. Bellis, N. Benmouna, B. L. Berman, W. Bertozzi, N. Bianchi, A. S. Biselli, S. Boiarinov, B. E. Bonner, S. Bouchigny, and R. Bradford, Phys. Rev. Lett. **92**, 052303 (2004)

[25] R. Shneor, P. Monaghan, R. Subedi, B. D. Anderson, K. Aniol, J. Annand, J. Arrington, H. Benaoum, F. Benmokhtar, P. Bertin, W. Bertozzi, W. Boeglin, J. P. Chen, S. Choi, E. Chudakov, E. Cisbani, B. Craver, C. W. de Jager, R. J. Feuerbach, S. Frullani, F. Garibaldi, O. Gayou, S. Gilad, R. Gilman, O. Glamazdin, J. Gomez, and J.-O. Hansen, Phys. Rev. Lett. **99**, 072501 (2007)

[26] D. L. Groep, M. F. van Batenburg, T. S. Bauer, H. P. Blok, D. J. Boersma, E. Cisbani, R. De Leo, S. Frullani, F. Garibaldi, W. Glöckle, J. Golak, P. Heimberg, W. H. A. Hesselink, M. Iodice, D. G. Ireland, E. Jans, H. Kamada, L. Lapikás, G. J. Lolos, C. J. G. Onderwater, R. Perrino, A. Scott, R. Starink, M. F. M. Steenbakkers, G. M. Urciuoli, H. de Vries, L. B. Weinstein, and H. Witała, Phys. Rev. C **63**, 014005 (2000)

[27] D. Middleton, J. Annand, C. Barbieri, P. Barneo, H. Blok, R. Bohm, M. Distler, J. Friedrich, C. Giusti, D. Glazier, P. Grabmayr, T. Hehl, J. Heim, W. Hesselink, E. Jans, M. Kohl, L. Lapikas, I. MacGregor, I. Martin, J. McGeorge, H. Merkel, F. Moschini, G. Rosner, M. Seimetz, H. de Vries, T. Walcher, D. Watts, and B. Zihlmann, The European Physical Journal A - Hadrons and Nuclei **29**, 261 (2006)

[28] D. G. Middleton, J. R. M. Annand, M. A. Antelo, C. Ayerbe, P. Barneo, D. Baumann, J. Bermuth, J. Bernauer, H. P. Blok, R. Böhm, D. Bosnar, M. Ding, M. O. Distler, J. Friedrich, J. G. Llongo, D. I. Glazier, J. Golak, W. Glöckle, P. Grabmayr, T. Hehl, J. Heim, W. H. A. Hesselink, E. Jans, H. Kamada, G. J. Mañas, M. Kohl, L. Lapikás, I. J. D. MacGregor, I. Martin, J. C. McGeorge,

H. Merkel, P. Merle, K. Monstad, F. Moschini, U. Müller, A. Nogga, R. Pérez-Benito, T. Pospis-chil, M. Potokar, G. Rosner, M. Seimetz, R. Skibiński, H. de Vries, T. Walcher, D. P. Watts, M. Weinriefer, M. Weiss, H. Wiała, and B. Zihlmann, Phys. Rev. Lett. **103**, 152501 (2009)

[29] J. Aclander, J. Alster, D. Barton, G. Bunce, A. Carroll, N. Christensen, H. Courant, S. Durrant, S. Gushue, S. Heppelmann, E. Kosonovsky, I. Mardor, Y. Mardor, M. Marshak, Y. Makdisi, E. Minor, I. Navon, H. Nicholson, E. Piasetzky, T. Roser, J. Russell, M. Sargsian, C. Sutton, M. Tanaka, C. White, and J.-Y. Wu, Physics Letters B **453**, 211 (1999)

[30] A. Tang, J. W. Watson, J. Aclander, J. Alster, G. Asryan, Y. Averichev, D. Barton, V. Baturin, N. Bukhtoyarova, A. Carroll, S. Gushue, S. Heppelmann, A. Leksanov, Y. Makdisi, A. Malki, E. Minina, I. Navon, H. Nicholson, A. Ogawa, Y. Panebratsev, E. Piasetzky, A. Schetkovsky, S. Shimanskiy, and D. Zhalov, Phys. Rev. Lett. **90**, 042301 (2003)

[31] O. Chamberlain and E. Segrè, Phys. Rev. **87**, 81 (1952)

[32] J. B. Cladis, W. N. Hess, and B. J. Moyer, Phys. Rev. **87**, 425 (1952)

[33] G. JACOB and T. A. J. MARIS, Rev. Mod. Phys. **38**, 121 (1966)

[34] G. JACOB and T. A. J. MARIS, Rev. Mod. Phys. **45**, 6 (1973)

[35] P. Kitching, W. McDonald, T. Maris, and C. Vasconcellos, in *ADVANCES IN NUCLEAR PHYSICS*, Vol. 15, edited by J. W. Negele and E. Vogt (PLENUM PRESS, 1985) Chap. 2, pp. 43–83

[36] P. G. Roos, N. S. Chant, D. W. Devins, D. L. Friesel, W. P. Jones, A. C. Attard, R. S. Henderson, I. D. Svalbe, B. M. Spicer, V. C. Officer, and G. G. Shute, Phys. Rev. Lett. **40**, 1439 (1978)

[37] P. Kitching, C. A. Miller, W. C. Olsen, D. A. Hutcheon, W. J. McDonald, and A. W. Stetz, Nuclear Physics A **340**, 423 (1980)

[38] L. Antonuk, P. Kitching, C. A. Miller, D. A. Hutcheon, W. J. McDonald, G. C. Neilson, W. C. Olsen, and A. W. Stetz, Nuclear Physics A **370**, 389 (1981)

[39] W. J. McDonald, R. N. MacDonald, W. C. Olsen, R. Dymarz, F. Khanna, L. Antonuk, J. M. Cameron, P. Kitching, G. C. Neilson, D. M. Sheppard, D. A. Hutcheon, C. A. Miller, and J. Kallne, Nuclear Physics A **456**, 577 (1986)

[40] C. Samanta, N. S. Chant, P. G. Roos, A. Nadasen, J. Wesick, and A. A. Cowley, Phys. Rev. C **34**, 1610 (1986)

[41] A. A. Cowley, J. V. Pilcher, J. J. Lawrie, and D. M. Whittal, Phys. Rev. C **40**, 1950 (1989)

[42] A. A. Cowley, J. J. Lawrie, G. C. Hillhouse, D. M. Whittal, S. V. Förtsch, J. V. Pilcher, F. D. Smit, and P. G. Roos, Phys. Rev. C **44**, 329 (1991)

[43] A. A. Cowley, G. J. Arendse, J. A. Stander, and W. A. Richter, Physics Letters B **359**, 300 (1995)

[44] R. Neveling, A. A. Cowley, G. F. Steyn, S. V. Förtsch, G. C. Hillhouse, J. Mano, and S. M. Wyngaardt, Phys. Rev. C **66**, 034602 (2002)

[45] S. Frullani and J. Mougey, in *ADVANCES IN NUCLEAR PHYSICS*, Vol. 14, edited by J. W. Negele and E. Vogt (PLENUM PRESS, 1984) pp. 1–283

[46] J. Kelly, in *ADVANCES IN NUCLEAR PHYSICS*, Vol. 23, edited by J. W. Negele and E. Vogt (PLENUM PRESS, 1996) Chap. 2, pp. 75–294

[47] G. J. Kramer, H. P. Blok, and L. Lapikás, Nuclear Physics A **679**, 267 (2001)

[48] G. Jacob, T. A. J. Maris, C. Schneider, and M. R. Teodoro, Physics Letters B **45**, 181 (1973)

[49] P. Kitching, C. A. Miller, D. A. Hutcheon, A. N. James, W. J. McDonald, J. M. Cameron, W. C. Olsen, and G. Roy, Phys. Rev. Lett. **37**, 1600 (1976)

[50] Y. Yasuda, Master's thesis, Kyoto University (2001)

[51] K. Hatanaka, K. Takahisa, H. Tamura, M. Sato, and I. Miura, Nuclear Instruments and Methods in Physics Research Section A: Accelerators, Spectrometers, Detectors and Associated Equipment **384**, 575 (1997)

[52] I. Miura, T. Yamazaki, A. Shimizu, K. Hosono, T. Itahashi, T. Saito, A. Ando, K. Tamura, K. Hatanaka, M. Kibayashi, M. Uraki, H. Ogata, M. Kondo, and H. Ikegami, in *Proceedings of the 13th International Conference on Cyclotrons and their Applications, Vancouver*, edited by G. Dutte and M. K. Craddock (World Scientific, Singapore, 1993) p. 3

[53] T. Wakasa, K. Hatanaka, Y. Fujita, G. P. A. Berg, H. Fujimura, H. Fujita, M. Itoh, J. Kamiya, T. Kawabata, K. Nagayama, T. Noro, H. Sakaguchi, Y. Shimbara, H. Takeda, K. Tamura, H. Ueno, M. Uchida, M. Uraki, and M. Yosoi, Nuclear Instruments and Methods in Physics Research Section A: Accelerators, Spectrometers, Detectors and Associated Equipment **482**, 79 (2002)

[54] M. Fujiwara, H. Akimune, I. Daito, H. Fujimura, Y. Fujita, K. Hatanaka, H. Ikegami, I. Katayama, K. Nagayama, N. Matsuoka, S. Morinobu, T. Noro, M. Yoshimura, H. Sakaguchi, Y. Sakemi, A. Tamii, and M. Yosoi, Nuclear Instruments and Methods in Physics Research Section A: Accelerators, Spectrometers, Detectors and Associated Equipment **422**, 484 (1999)

[55] M. Fujiwara, A. Nakanishi, Y. Fujita, N. Matsuoka, T. Noro, S. Morinobu, and H. Ikegami, RCNP annual report(1989)

[56] N. Matsuoka, T. Noro, K. Sagara, S. Morinobu, A. Okihara, and K. Hatanaka, RCNP annual report(1990)

[57] N. Matsuoka, T. Noro, K. Sagara, S. Morinobu, A. Okihara, and K. Hatanaka, RCNP annual report(1991)

[58] T. Noro, M. Fujiwara, O. Kamigaito, S. Hirata, Y. Fujita, A. Yamagoshi, T. Takahashi, H. Akimune, Y. Sakemi, M. Yosoi, H. Sakaguchi, and J. Tanaka, RCNP annual report(1991)

[59] A. Tamii, H. Sakaguchi, H. Takeda, M. Yosoi, H. Akimune, M. Fujiwara, H. Ogata, M. Tanaka, and H. Togawa, IEEE Transactions on Nuclear Science **43**, 2488 (1996)

[60] A. Tamii, M. Itoh, T. Kawabata, H. Sakaguchi, H. Takeda, T. Taki, H. Torii, M. Yosoi, H. Akimune, T. Baba, M. Fujiwara, M. Kawabata, T. Noro, , and H. Yoshida, in *Proceedings of the 2nd International Data Acquisition Workshop on Networked Data Acquisition System, Osaka, Japan, 1996*, edited by M. Nomachi and S. Ajimura (World Scientific, Singapore, 1997) p. 238

[61] T. Kawabata, H. Sakaguchi, A. Tamii, H. Takeda, T. Taki, and H. Yoshida, RCNP annual report(1996)

[62] H. Takeda, H. Sakaguchi, A. Tamii, H. Akimune, M. Kawabata, and M. Tanaka, in *Proceedings of the 1995 IEEE Conference on Real-Time Computer Applications in Nuclear Particle and Plasma Physics* (1995) p. 210

[63] HBOOK, CERN Program Library entry Y250

[64] PAW, CERN Program Library entry Q121

[65] M. Ieiri, H. Sakaguchi, M. Nakamura, H. Sakamoto, H. Ogawa, M. Yosol, T. Ichihara, N. Isshiki, Y. Takeuchi, H. Togawa, T. Tsutsumi, S. Hirata, T. Nakano, S. Kobayashi, T. Noro, and H. Ikegami, Nuclear Instruments and Methods in Physics Research Section A: Accelerators, Spectrometers, Detectors and Associated Equipment **257**, 253 (1987)

[66] N. Fujita, *Calibrations of the absolute value of the cross sections for the elastic scattering via 300MeV proton*, Master's thesis, University of Miyazaki (2009)

[67] L. Ray, Phys. Rev. C **20**, 1857 (1979)

[68] R. A. Arndt, W. J. Briscoe, I. I. Strakovsky, and R. L. Workman, Phys. Rev. C **76**, 025209 (2007)

[69] Center for Nuclear Studies, Data Analysis Center, SAID Program, `http://gwdac.phys.gwu.edu/`

[70] N. S. Chant and P. G. Roos, Phys. Rev. C **27**, 1060 (1983)

[71] R. A. Arndt, J. S. Hyslop, and L. D. Roper, Phys. Rev. D **35**, 128 (1987)

[72] E. D. Cooper, S. Hama, B. C. Clark, and R. L. Mercer, Phys. Rev. C **47**, 297 (1993)

[73] L. R. B. Elton and A. Swift, Nuclear Physics A **94**, 52 (1967)

[74] G. Kramer, H. Blok, J. V. D. Brand, H. Bulten, R. Ent, E. Jans, J. Lanen, L. Lapikás, H. Nann, E. Quint, G. V. D. Steenhoven, P. D. W. Huberts, and G. Wagner, Physics Letters B **227**, 199 (1989)

[75] I. Angeli, Atomic Data and Nuclear Data Tables **87**, 185 (2004)

[76] H. Sakaguchi, M. Nakamura, K. Hatanaka, A. Goto, T. Noro, F. Ohtani, H. Sakamoto, H. Ogawa, and S. Kobayashi, Phys. Rev. C **26**, 944 (1982)

[77] J. W. A. den Herder, H. P. Blok, E. Jans, P. H. M. Keizer, L. Lapikás, E. N. M. Quint, G. van der Steenhoven, and P. K. A. de Witt Huberts, Nuclear Physics A **490**, 507 (1988)

[78] R. B. Firestone and C. M. Baglin, *Table of Isotopes*, 8th ed. (John Wiley & Sons.Inc., 1999)

[79] Y. Kudo and K. Miyazaki, Phys. Rev. C **34**, 1192 (1986)

[80] J. Mano and Y. Kudo, Progress of Theoretical Physics **100**, 91 (1998)

[81] J. C. Hiebert, E. Newman, and R. H. Bassel, Phys. Rev. **154**, 898 (1967)

[82] T. Noro, T. Yonemura, S. Asaji, N. S. Chant, K. Fujita, Y. Hagihara, K. Hatanaka, G. C. Hillhouse, T. Ishida, M. Itoh, S. Kishi, M. Nakamura, Y. Nagasue, H. Sakaguchi, Y. Sakemi, Y. Shimizu, H. Takeda, Y. Tamesige, S. Terashima, M. Uchida, T. Wakasa, Y. Yasuda, H. P. Yoshida, and M. Yosoi, Phys. Rev. C **72**, 041602 (2005)

[83] C. A. Miller, K. H. Hicks, R. Abegg, M. Ahmad, N. S. Chant, D. Frekers, P. W. Green, L. G. Greeniaus, D. A. Hutcheon, P. Kitching, D. J. Mack, W. J. McDonald, W. C. Olsen, R. Schubank, P. G. Roos, and Y. Ye, Phys. Rev. C **57**, 1756 (1998)

[84] K. Hatanaka, M. Kawabata, N. Matsuoka, Y. Mizuno, S. Morinobu, M. Nakamura, T. Noro, A. Okihana, K. Sagara, K. Takahisa, H. Takeda, K. Tamura, M. Tanaka, S. Toyama, H. Yamazaki, and Y. Yuasa, Phys. Rev. Lett. **78**, 1014 (1997)

[85] O. V. Miklukho, N. P. Aleshin, S. L. Belostotski, Y. V. Elkin, O. G. Grebenyuk, O. Y. Fedorov, A. A. Izotov, A. A. Jgoun, A. Y. Kisselev, M. P. Levchenko, Y. G. Naryskin, V. V. Nelyubin, A. N. Prokofiev, D. A. Prokofiev, Y. A. Scheglov, A. V. Shvedchikov, V. V. Vikhrov, and A. A. Zhdanov, Nuclear Physics A **683**, 145 (2001)

[86] V. A. Andreev, M. N. Andronenko, G. M. Amalsky, S. L. Belostotski, O. A. Domchenkov, O. Y. Fedorov, K. Hatanaka, A. A. Izotov, A. A. Jgoun, J. Kamiya, A. Y. Kisselev, M. A. Kopytin, O. V. Miklukho, Y. G. Naryshkin, T. Noro, E. Obayashi, A. N. Prokofiev, D. A. Prokofiev, H. Sakaguchi, V. V. Sulimov, A. V. Shvedchikov, H. Takeda, S. I. Trush, V. V. Vikhrov, T. Wakasa, Y. Yasuda, and H. P. Yoshida, Phys. Rev. C **69**, 024604 (2004)

[87] A. A. Cowley, G. J. Arendse, R. F. Visser, G. F. Steyn, S. V. Förtsch, J. J. Lawrie, J. V. Pilcher, T. Noro, T. Baba, K. Hatanaka, M. Kawabata, N. Matsuoka, Y. Mizuno, M. Nomachi, K. Takahisa, K. Tamura, Y. Yuasa, H. Sakaguchi, T. Itoh, H. Takeda, and Y. Watanabe, Phys. Rev. C **57**, 3185 (1998)

[88] R. Sartor and C. Mahaux, Phys. Rev. C **21**, 2613 (1980)

[89] S. Terashima, H. Sakaguchi, H. Takeda, T. Ishikawa, M. Itoh, T. Kawabata, T. Murakami, M. Uchida, Y. Yasuda, M. Yosoi, J. Zenihiro, H. P. Yoshida, T. Noro, T. Ishida, S. Asaji, and T. Yonemura, Phys. Rev. C **77**, 024317 (2008)

[90] S. Hama, B. C. Clark, E. D. Cooper, H. S. Sherif, and R. L. Mercer, Phys. Rev. C **41**, 2737 (1990)

[91] F. Perey and B. Buck, Nuclear Physics **32**, 353 (1962)

[92] K. G. Fissum, M. Liang, B. D. Anderson, K. A. Aniol, L. Auerbach, F. T. Baker, J. Berthot, W. Bertozzi, P.-Y. Bertin, L. Bimbot, W. U. Boeglin, E. J. Brash, V. Breton, H. Breuer, E. Burtin, J. R. Calarco, L. S. Cardman, G. D. Cates, C. Cavata, C. C. Chang, J.-P. Chen, E. Cisbani, D. S. Dale, C. W. de Jager, R. De Leo, A. Deur, and B. Diederich, Phys. Rev. C **70**, 034606 (2004)

[93] A. Gade, D. Bazin, B. A. Brown, C. M. Campbell, J. A. Church, D. C. Dinca, J. Enders, T. Glasmacher, P. G. Hansen, Z. Hu, K. W. Kemper, W. F. Mueller, H. Olliver, B. C. Perry, L. A. Riley, B. T. Roeder, B. M. Sherrill, J. R. Terry, J. A. Tostevin, and K. L. Yurkewicz, Phys. Rev. Lett. **93**, 042501 (2004)

[94] A. Gade, P. Adrich, D. Bazin, M. D. Bowen, B. A. Brown, C. M. Campbell, J. M. Cook, T. Glasmacher, P. G. Hansen, K. Hosier, S. McDaniel, D. McGlinchery, A. Obertelli, K. Siwek, L. A. Riley, J. A. Tostevin, and D. Weisshaar, Phys. Rev. C **77**, 044306 (2008)

[95] R. J. Charity, L. G. Sobotka, and W. H. Dickhoff, Phys. Rev. Lett. **97**, 162503 (2006)

[96] Y. Nagasue, Master's thesis, Kyushu University (2006)

[97] Y. Yasuda, H. Sakaguchi, S. Asaji, K. Fujita, Y. Hagihara, K. Hatanaka, T. Ishida, M. Itoh, T. Kawabata, S. Kishi, T. Noro, Y. Sakemi, Y. Shimizu, H. Takeda, Y. Tameshige, S. Terashima, M. Uchida, T. Wakasa, T. Yonemura, H. P. Yoshida, M. Yosoi, and J. Zenihiro, Phys. Rev. C **81**, 044315 (Apr 2010)

[98] A. Werbrouck, in *Kinematics and Multiparticle Systems*, edited by M. Nikolić (GORDON AND BREACH, 1968)

List of Tables

List of Figures